

TOPICAL REVIEW

## Optics of exciton-plasmon nanomaterials

To cite this article: Maxim Sukharev and Abraham Nitzan 2017 *J. Phys.: Condens. Matter* **29** 443003

View the [article online](#) for updates and enhancements.

### Related content

- [Strong coupling between surface plasmon polaritons and emitters: a review](#)  
P Törmä and W L Barnes
- [Surface plasmon resonance in gold nanoparticles: a review](#)  
Vincenzo Amendola, Roberto Pilot, Marco Frasconi et al.
- [Topical Review](#)  
Emmanuel Fort and Samuel Grésillon

## Topical Review

# Optics of exciton-plasmon nanomaterials

Maxim Sukharev<sup>1,2</sup> and Abraham Nitzan<sup>3</sup><sup>1</sup> College of Integrative Sciences and Arts, Arizona State University, Mesa, AZ 85212, United States of America<sup>2</sup> Department of Physics, Arizona State University, Tempe, AZ 85287, United States of America<sup>3</sup> Department of Chemistry, University of Pennsylvania, Philadelphia, PA 19104, United States of AmericaE-mail: [maxim.sukharev@asu.edu](mailto:maxim.sukharev@asu.edu)

Received 23 April 2016, revised 10 August 2017


Accepted for publication 14 August 2017

Published 5 October 2017

**Abstract**

This review provides a brief introduction to the physics of coupled exciton-plasmon systems, the theoretical description and experimental manifestation of such phenomena, followed by an account of the state-of-the-art methodology for the numerical simulations of such phenomena and supplemented by a number of FORTRAN codes, by which the interested reader can introduce himself/herself to the practice of such simulations. Applications to CW light scattering as well as transient response and relaxation are described. Particular attention is given to so-called strong coupling limit, where the hybrid exciton-plasmon nature of the system response is strongly expressed. While traditional descriptions of such phenomena usually rely on analysis of the electromagnetic response of inhomogeneous dielectric environments that individually support plasmon and exciton excitations, here we explore also the consequences of a more detailed description of the molecular environment in terms of its quantum density matrix (applied in a mean field approximation level). Such a description makes it possible to account for characteristics that cannot be described by the dielectric response model: the effects of dephasing on the molecular response on one hand, and nonlinear response on the other. It also highlights the still missing important ingredients in the numerical approach, in particular its limitation to a classical description of the radiation field and its reliance on a mean field description of the many-body molecular system. We end our review with an outlook to the near future, where these limitations will be addressed and new novel applications of the numerical approach will be pursued.

Keywords: strong coupling, plasmonics, exciton-plasmon

 Supplementary material for this article is available [online](#)

(Some figures may appear in colour only in the online journal)

**1. Introduction**

The collective response of systems involving interacting material systems and optical fields has been studied for a long time, yielding many fascinating modes of behavior. Traditionally light is regarded only as a probing and triggering tool and the observed response is associated with properties of the material system. It has however long been known that

often an observed signal reflects not properties of the material system but of the light–matter hybrid<sup>4</sup>. The most explicit manifestations of this hybrid nature are polaritons—hybrid

<sup>4</sup> It should be emphasized that this distinction is sometimes in our mind only. Spontaneous emission of an excited molecule, which is often regarded as a molecular property, is a property of the molecule–field system in the same way that radiationless relaxation of this molecule is a property of the molecule and its environment.

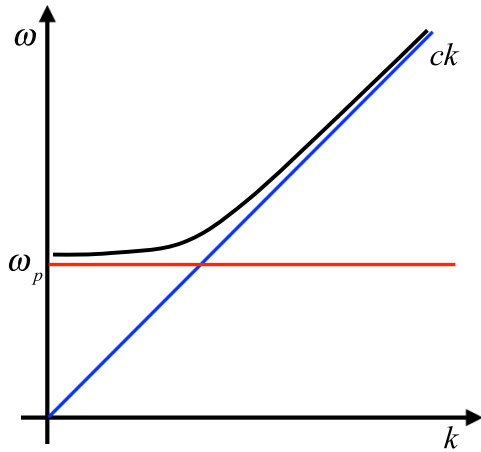


**Figure 1.** The dispersion  $\omega(k)$  (black line) for electromagnetic propagation in a Drude metal appears to result from avoided crossing between the plasmon frequency  $\omega_p$  (red line) and the light line  $\omega = ck$  (blue line).

states of light and matter that display properties of both. Their classical description is obtained when solving the Maxwell equations in an environment whose dielectric properties, represented by the dielectric response function,  $\epsilon(\mathbf{k}, \omega)$  reflect resonance oscillations of charges or dipole fields. This review follows the common practice of using the position-local dielectric response (that is, replacing  $\epsilon(\mathbf{k}, \omega)$  by  $\epsilon(\omega) = \epsilon(k = 0, \omega)$ ), which is experimentally accessible for many systems, however it should be stated at the outset that non-local effects may be important and understanding the extent of their importance continues to be a challenge. With regard to the local dielectric function, one can use the numerical data obtained experimentally, or commonly used model dielectric functions with parameters chosen to approximate such numerical data.

### 1.1. Dielectric response models

For metals, the simplest description of dielectric response is provided by the Drude model [1, 2] that considers conducting electrons as an ideal gas of non-interacting charged particles moving under Newton’s second law augmented by including a phenomenological friction term (see [3, 4]). This leads to the dielectric response function in the form

$$\epsilon_r(\omega) = \epsilon_{r,\infty} - \frac{\omega_p^2}{\omega(\omega - i\gamma)}. \quad (1)$$

Here  $\omega_p$  is the plasma frequency,  $\omega_p = n_e e^2 / (\epsilon_0 m_e) \sim 10^{16} \text{ s}^{-1}$ , where  $m_e$  and  $n_e$  are the electron mass and the electrons density, respectively, and  $\epsilon_{r,\infty}$  represents high frequency contributions from atomic core electrons (we use the notation  $\epsilon_r = \epsilon/\epsilon_0$  throughout this review). Applying this model to light propagation in homogeneous bulk metals, the dispersion relation  $k^2 = \omega^2 \epsilon_r(\omega) / c^2$  becomes for  $\omega \gg \gamma$  (which holds near and above  $\omega_p$ )  $k = (\omega/c) \sqrt{\epsilon_{r,\infty} - \omega_p^2/\omega^2}$ , implying that electromagnetic wave propagation is possible only for  $\omega \sqrt{\epsilon_{r,\infty}} > \omega_p$ , while at  $\omega \sqrt{\epsilon_{r,\infty}} = \omega_p$  all conducting electrons throughout the metal oscillate in phase. Note that

this dispersion appears (see figure 1) to result from avoided crossing between the metal plasmon mode of frequency  $\omega_p$  and the light line  $k = \omega/c$  that represent this dispersion well for  $\omega \gg \omega_p$ . The distortion of this dispersion as  $\omega \rightarrow \omega_p$  from above indicates strong coupling between light and plasma charge oscillations in the metal, creating the hybrid plasmon (or plasmon-polariton) mode.

In general the Drude model qualitatively describes the optical response of metals for a short range of frequencies. When modeling scattering of electromagnetic radiation by metal systems it is a common practice to treat  $\omega_p$ ,  $\epsilon_{r,\infty}$ , and  $\gamma$  as fitting parameters to better describe real and imaginary parts of the dielectric function for a given range of frequencies. Following this approach, another commonly used model combines the Drude function with the more general Lorentz function [5]

$$\epsilon_r(\omega) = \epsilon_{r,\infty} - \frac{\omega_p^2}{\omega^2 - i\gamma\omega} - \sum_{n=1}^N \frac{\Delta\epsilon_{r,n}\omega_n^2}{\omega^2 - i\gamma_n\omega - \omega_n^2}, \quad (2)$$

where the third term is the sum over contributions referred to as arising from the  $n$ th Lorentz oscillator. It can represent the effect of interband transitions as well as motions of the ionic cores. Parameters in the Lorentz part are treated as phenomenological fitting parameters. For example, it was shown that the optical response of silver could be described by (2) for the range of frequencies between 0.1 eV and 5 eV with 5 Lorentz poles [5].

A particular form of the Lorentz function is often used to describe the near infrared response of ionic crystals, where a simple model for the dielectric response yields [3]

$$\begin{aligned} \epsilon_r(\omega) &= \epsilon_{r,\infty} + \frac{\epsilon_{r,0} - \epsilon_{r,\infty}}{(\omega/\omega_T)^2 - 1} = \frac{\epsilon_{r,\infty}(\omega/\omega_T)^2 - \epsilon_{r,0}}{(\omega/\omega_T)^2 - 1} \\ &= \epsilon_{r,0} \frac{(\omega/\omega_L)^2 - 1}{(\omega/\omega_T)^2 - 1}, \end{aligned} \quad (3)$$

where  $\epsilon_{r,0}$  and  $\epsilon_{r,\infty}$  are, respectively, the static ( $\omega \rightarrow 0$ ) and the electronic ( $\omega_T \ll \omega < \omega_{el}$ ) dielectric response constants, while  $\omega_T$  and  $\omega_L = \omega_T \sqrt{\epsilon_0/\epsilon_\infty}$  are the long wavelength limits of the transversal and longitudinal optical phonon frequencies. Using again  $k = (\omega/c) \sqrt{\epsilon_r(\omega)}$  we see that no light can propagate in the crystal for  $\omega_T < \omega < \omega_L$  because  $\epsilon$  is negative in this region. (note that  $\omega_L > \omega_T$  follows from the fact that the full dielectric response  $\epsilon_{r,0}$  is larger than  $\epsilon_\infty$  which reflects electronic response only). For  $\omega \rightarrow 0$   $k \rightarrow (\omega/c) \sqrt{\epsilon_{r,0}}$  while in the limit  $\omega \rightarrow \infty$   $k \rightarrow (\omega/c) \sqrt{\epsilon_{r,\infty}}$ . The overall dispersion as shown schematically in figure 2 can be interpreted as showing an avoided crossing between the low frequency light line and the transversal optical phonon as  $\omega \rightarrow \omega_T$  from below, and a crossing between the high frequency light line and the longitudinal optical phonon as  $\omega \rightarrow \omega_L$  from above. The distortion of the light line near the optical phonon frequencies and the formation of a frequency gap are again manifestation of strong coupling between the radiation field and the lattice optical phonons that results in hybrid phonon-polariton modes.

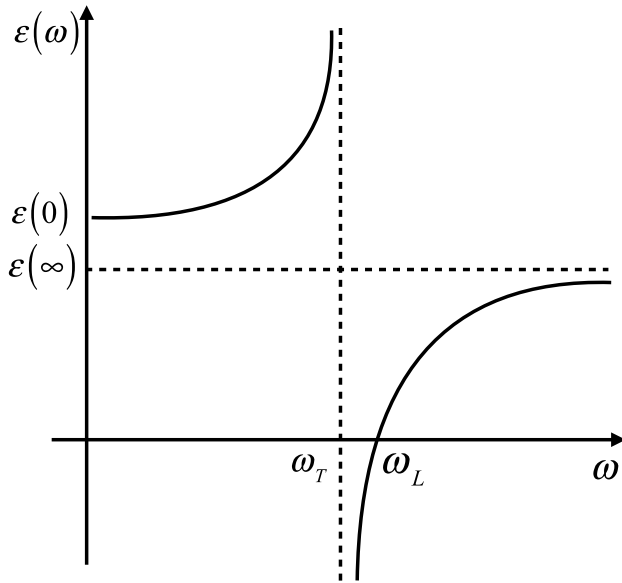


**Figure 2.** Dielectric constant as a function of frequency for a diatomic ionic crystal.

A qualitatively similar behavior is encountered at higher frequencies when the frequency dependence of the dielectric response is dominated by electronic resonances. A simple model for the dielectric function of a system of randomly oriented molecules is<sup>5</sup>

$$\epsilon_r(\omega) = \frac{\omega - \omega_L}{\omega - \omega_T}. \quad (4)$$

Here  $\omega_T = \omega_0 - \eta$  where  $\eta = |\mu|^2/3\epsilon_0\hbar v$  (here  $\omega_0$  and  $\mu$  are the molecular transition frequency and transition dipole, respectively) is of order  $10^{13} \text{ s}^{-1}$  in condensed systems and  $\omega_L = \sqrt{\epsilon_r}\omega_T$  (here  $\epsilon_{r,\infty} = 1$  and  $\epsilon_{r,0} > 1$ ) are again frequencies of transversal and longitudinal exciton modes, respectively. As in equation (3),  $\epsilon$  diverges at  $\omega = \omega_T$ , vanishes at  $\omega = \omega_L$  and shows a forbidden gap for  $\omega_T < \omega < \omega_L$  where EM waves cannot propagate because  $\epsilon < 0$ . The dispersion relation for the resulting exciton-polariton is similar to that shown in figure 2, except that  $\omega_T$  and  $\omega_L$  now take values of the order of electronic transition frequencies  $\sim 10^{15} \text{ s}^{-1}$ .

### 1.2. Collective optical response of metallic nanostructures

Geometry strongly affects the way by which such collective response phenomena are manifested. At a planar surface between two dielectrics characterized by dielectric response functions  $\epsilon_1(\omega)$ ,  $\epsilon_2(\omega)$  (see figure 3) Maxwell's equation can yield a solution that propagate along the surface,  $\exp(ik_x x - k_{zj}|z| - i\omega t)$ ;  $j = 1, 2$  with

$$k_x = \frac{\omega}{c} \sqrt{\left(\frac{\epsilon_1 \epsilon_2}{\epsilon_1 + \epsilon_2}\right)} \quad \text{and} \quad k_{zj} = \frac{\omega}{c} \sqrt{\frac{\epsilon_j^2}{\epsilon_1 + \epsilon_2}} \quad (5)$$

<sup>5</sup> Equation (4) is obtained from the polarizability expression  $\alpha_{el}(\omega) \sim |\mu|^2/\hbar(\omega_0 - \omega)$  where  $\mu$  is the transition dipole matrix element between the two electronic states and  $\omega_0$  is the corresponding transition frequency (energy spacing between these states), and the Clausius–Mossotti equation,  $\frac{\epsilon-1}{\epsilon+2} = \frac{\alpha}{3v}$  where  $v$  is the volume per molecule (inverse molecular number density).

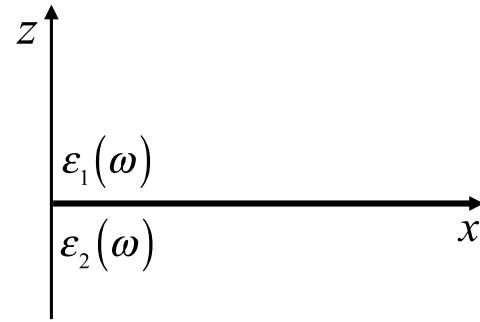


**Figure 3.** Planar interface between two dispersive dielectrics.

offering a variety of behaviors for different interfaces, namely different choices of  $\epsilon_j(\omega)$ ,  $j = 1, 2$  [6, 7]. For a recent review see [8]. Importantly, when the two sides of the interface have their own collective response character, e.g. metal plasmons and molecular excitons, the resulting surface modes can display interaction between such collective excitations, offering new modes of behaviors and potentially novel applications [8].

Such surface modes, including excitations obtained on more structured surfaces such as periodic arrays of holes or slits [9] are referred to as surface polaritons, and in the common case involving metal surfaces—surface plasmon polaritons (SPPs). Small particles constitute another class of systems with interesting plasmon behavior. For a small metal particle, plasmonic charge oscillations are obviously not a traveling wave but a collective electronic response localized on the particle's surface. Such excitations are referred to as localized surface plasmon-polaritons (LSPPs) [10]. For a comprehensive review of terminology used in plasmonics see chapter 3 in [11]. While the standard description is found in many textbooks, we use here an approximate representation [12, 13] that can serve to illustrate the connection to other electromagnetic response situations. Limiting ourselves to a small metal sphere in the electrostatic limit (radius  $a$  and all distances considered much smaller than the radiation wavelength), the potential associated with the plasmon excitations is given by<sup>6</sup>

$$\Phi(r, \theta, \phi) = \sum_{l=1}^{\infty} \sum_{m=-l}^l (A_{lm}(r, \theta, \phi) b_{lm} + A_{lm}^*(r, \theta, \phi) b_{lm}^*) \quad (6)$$

where the functions  $A_{lm}$  are defined in terms of the spherical harmonics  $Y_{lm}$

$$A_{lm}(r, \theta, \phi) = \left[ \frac{\hbar}{al \text{Re } \epsilon'(\omega_l)} \right]^{1/2} Y_{lm}(\theta, \phi) \begin{cases} \left(\frac{r}{a}\right)^{-l-1} & r \geq a \\ \left(\frac{r}{a}\right)^l & r \leq a \end{cases} \quad (7)$$

with  $\epsilon'(\omega) = d\epsilon/d\omega$ . In this representation, the free plasmon modes  $b_{lm}$  satisfy the equations of motion of damped harmonic oscillators,  $\dot{b}_{lm} = -i\omega_l b_{lm} - (1/2)\gamma_l b_{lm}$ , where  $\omega_l$  is the solution of

<sup>6</sup> In the electrostatic limit the interaction of a molecular dipole  $\mu$  is well represented by  $-\mu \cdot E = \mu \cdot \nabla \Phi$ .

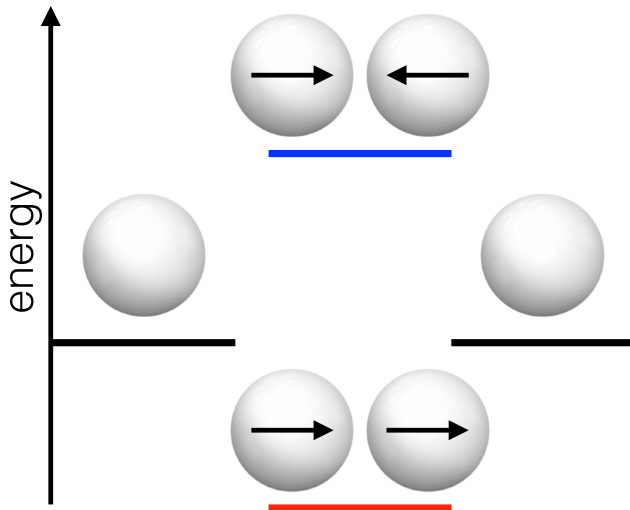


**Figure 4.** The plasmon hybridization model applied to two interacting nanoparticles. The model explains the physical nature of two observed resonances corresponding to anti-bonding (upper state) and bonding (lower state) formed when two nanoparticles are placed close together.

$$\text{Re } \varepsilon_r(\omega_l) = -\frac{l+1}{l}, \quad (8)$$

while  $\gamma_l$  is given by

$$\gamma_l = \frac{2 \text{Im } \varepsilon(\omega_l)}{\text{Re } \varepsilon'(\omega_l)}. \quad (9)$$

The derivation of this form, and in particular assigning harmonic nature to the particle plasmons, assume that these plasmons are underdamped and well separated, which holds only for the low  $l$  plasmons of some metals. When these conditions hold, we can if needed consider the quantization of this field by replacing  $b$  and  $b^*$  by raising and lowering operators  $\hat{b}$  and  $\hat{b}^\dagger$ . It should be emphasized however that while the representation of plasmons in small metal particles as (damped) harmonic oscillations is a common practice, this is more a matter of convenience than a rigorous result. In fact, experimental evidence that plasmon excitations in metal particles can be saturated [14], implies that their assigned harmonic nature is only an approximation.

Another important geometry is that of a cavity, where the radiation field is confined within reflecting walls. When such a cavity supports one mode of frequency  $\omega$  the field at position  $x$  along the cavity axis is given by

$$\varepsilon(t) = i \sum_{\mathbf{k}} \sum_{\sigma_{\mathbf{k}}} \sqrt{\frac{\hbar \omega_{\mathbf{k}}}{2 \varepsilon \Omega}} \sigma_{\mathbf{k}} \left( a_{\mathbf{k}, \sigma_{\mathbf{k}}} e^{i(\mathbf{k} \cdot \mathbf{r} - \omega_{\mathbf{k}} t)} - a_{\mathbf{k}, \sigma_{\mathbf{k}}}^* e^{-i(\mathbf{k} \cdot \mathbf{r} - \omega_{\mathbf{k}} t)} \right) \quad (10)$$

with the classical amplitude  $a$  ( $a^*$ ) becoming the raising and lowering operators  $\hat{a}$  and  $\hat{a}^\dagger$  in the quantum theory. Importantly, interactions of such a mode with other degrees of freedom depend on the cavity volume  $\Omega$ , namely the cavity length  $L_x$  ( $L_y$  and  $L_z$  are assumed to be much smaller than the wavelength). In the ideal case of perfect mirrors, the metal is not involved except by imposing the reflecting boundary conditions. Optical interactions in high- $Q$  cavities can be

analyzed in terms of such cavity modes, adding when needed small damping into the time dependence of equation (10). In optical regimes where the loss is higher, the objects making the mirror become part of the system, cavity physics becomes inter-metal gap physics, and the modes responsible for optical excitations in the space between metals become plasmon-polariton modes whose properties are derived from the dielectric properties of the metals and the geometries of both the gaps and the metal objects. To understand the electromagnetic field behavior in such gaps one needs to consider the full collective response of the system comprising the metal objects and the space between them. For simple geometries this leads to considerations of plasmon hybridization [15–18], (see figure 4 below) while in more complex systems numerical solutions of the Maxwell equations are needed [19].

### 1.3. The molecular system

Next, consider the molecular system. Many observed phenomena could be analyzed, at least qualitatively, by modeling the molecule as a polarizable point object. In this physical limit the effect of the molecule on the plasmonic system is largely disregarded—it is taken into account only so much as it affects the molecule itself (for example by creating image effects or, in more sophisticated treatments, by adding self energy terms into the molecule equations of motion). In this limit the main effect of proximity to a metal surface is assumed to be the molecular interaction with the local electromagnetic field<sup>7</sup> that reflects the response of the metal system to the electromagnetic field of the molecule as well to any incident radiation.

Many interesting observations can be understood qualitatively and at time quantitatively on this level. This includes the electromagnetic theory of surface enhanced Raman scattering [26] (for recent reviews see [27, 28]) that has been later generalized to other photophysical and photochemical properties of molecules adsorbed on metal surfaces and nanostructures [12, 29–31], and analysis of observed modification of radiative and non-radiative relaxation rates of molecules seated near such structures. For example, for a molecule represented by an oscillating charge distribution near a small dielectric structure, the modification of the radiative relaxation rate can be obtained [12, 13, 32] by evaluating the total oscillating dipole in the metal-molecule composite (for a general analysis of such observations near a flat metal surface see [33]). For a molecule represented by an oscillating point dipole at a distance  $R$  from the center of a small dielectric sphere of radius  $a$ , where all distances correspond to the electrostatic limit, this leads to the radiative relaxation rate

$$\Gamma_R = |B|^2 \Gamma_{R0}, \quad (11)$$

where  $\Gamma_{R0}$  is the corresponding rate for the free molecule and where

<sup>7</sup> At close proximity, other effects such as electron transfer between metal and molecules that affect not only the electromagnetic response but also the electronic structure of the metal-molecule composite come into play [20–25]. We do not deal with such effects in this review.

$$B = \begin{cases} 1 + \frac{2(\varepsilon - \varepsilon_s)a^3}{(\varepsilon + 2\varepsilon_s)R^3} & \perp \\ 1 - \frac{(\varepsilon - \varepsilon_s)a^3}{(\varepsilon + 2\varepsilon_s)R^3} & \parallel \end{cases}. \quad (12)$$

In equation (12)  $\varepsilon = \varepsilon(\omega_m)$  and  $\varepsilon_s = \varepsilon_s(\omega_m)$  are the dielectric response functions of the sphere and its environment, respectively, evaluated at the molecular transition frequency  $\omega_m$ , and (here and below)  $\perp$  and  $\parallel$  denote configurations with the dipole being perpendicular and parallel to the sphere surface, respectively. A possibly large effect is seen when  $\omega_m$  is close to  $\omega_p$ , the dipolar plasmon frequency that satisfies  $\text{Re}[\varepsilon(\omega_p) + 2\varepsilon_s(\omega_p)] = 0$ , provided that the imaginary part of this sum is not too large<sup>8</sup>. The latter is known to exist for the noble metals (Ag, Au, Cu) as well as Al. The non-radiative relaxation rate can be calculated by evaluating the rate at which the oscillating molecular charge distribution drives heat generation in the metal,  $\int d^3r (1/2)\sigma|E|^2$  where  $\sigma = \omega \text{Im}(\varepsilon(\omega_m))$  is the conduction at the driving frequency. This leads to

$$\Gamma_{\text{NR}}^{\perp} = -\frac{|\mu|^2}{8\pi\varepsilon_0\hbar a^3} \sum_{l=1}^{\infty} (l+1)^2 (2l+1) \left(\frac{a}{R}\right)^{2(l+2)} \text{Im} \frac{1}{l\varepsilon_r + (l+1)\varepsilon_{rs}}, \quad (13a)$$

$$\Gamma_{\text{NR}}^{\parallel} = -\frac{|\mu|^2}{16\pi\varepsilon_0\hbar a^3} \sum_{l=1}^{\infty} l(l+1)(2l+1) \left(\frac{a}{R}\right)^{2(l+2)} \text{Im} \frac{1}{l\varepsilon_r + (l+1)\varepsilon_{rs}}. \quad (13b)$$

The sums in these expressions represent the contributions of different multipole plasmons to the non-radiative relaxation rate, and are seen to be enhanced at the corresponding plasmon resonance frequencies for which  $\text{Re}[\varepsilon(\omega) + (l+1)\varepsilon_s(\omega)] = 0$ . Note that these rates represent the non-radiative relaxation induced by the metal, and will add to the rates of other non-radiative processes that may be present in the molecular system. In fact, at close proximity, another non-radiative decay channel induced by the metal, electron tunneling between metal and molecule, should also be taken into account.

Validity limits of the model approximations made above should be kept in mind when considering applications to real molecular/metal systems [34–44]. (See [45, 46] for recent reviews.) A point dipole can hardly represent a large dye molecule adsorbed on a small metal particle. The use of a local dielectric function to represent the dielectric response of small particles becomes questionable for small particle sizes (see [47–50]). At large particle size and/or molecule distances the electrostatic approximation breaks down and a full retarded electromagnetic theory is needed. This fact, overlooked in some interpretations of distance dependence of molecule-metal particle energy transfer [41, 42, 45, 46, 51–54], was highlighted in a recent numerical calculation [55]. Many other generalizations of the theory have been published in the past three decades [36, 48, 56–73].

It is notable that the Gersten–Nitzan theory as many of its generalizations represent the molecule as a classical dipole<sup>9</sup>. This may appear strange considering the fact that the rate of

spontaneous emission, an inherently quantum phenomenon, is obtained from this calculation. The well-known [12, 13, 74–79] reason is that this calculation addresses only the effect of proximity to a metal surface, namely the *ratio* between the molecular radiative lifetimes at and away from the metal surface, and this ratio does not depend in our simple model on the quantum nature of this process. Another way to understand this is to observe that the radiative relaxation rate can be obtained from the golden rule formula in terms of the local density of final states of the radiation field, a property that can be calculated for different positions in an inhomogeneous dielectric environment using information obtained from the classical Maxwell equations [80, 81].

Finally, and closer to the focus of this review, in most observations of interacting molecules-plasmon system, the molecular system is not a single molecule but an assembly of atoms or molecules—a molecular aggregate or a molecular layer adsorbed on the metal surface. This has two important consequences. First, the molecular subsystem can have a substantial effect on the plasmonic response of the metal, so the optical behavior has to be considered by treating its molecular and metal parts self-consistently. Second, coherent response of the molecular assembly can play an important role in the ensuing dynamics, and question about what determines coherence and dephasing and their impact on the molecular optical response naturally comes up. For a large molecular assembly, for example when one of the dielectrics separated by a planar interface is the molecular environment, the coherent response of the molecular system can be accounted for by using a suitable dielectric function to describe this environment as in equation (5). Alternatively, a microscopic description of the molecular side has the advantage that it can describe processes that go beyond simple (linear) dielectric response such as dephasing and nonlinear spectroscopy. For this level of description the molecule can be modeled as an  $n$ -level system (most simply  $n = 2$ , see, e.g. [82–85]) and can be described by the optical Bloch equations (chapter 10 in [86]) driven by the local electromagnetic field. The latter, in turn, is evaluated from the classical Maxwell equations in which the time derivative of expectation value of the molecular dipole,  $\text{Tr}(\hat{\mu}\dot{\rho})$  constitutes a current source. This level of calculations is important in particular when many molecules are involved and we return to its detailed description below.

#### 1.4. Collective response of molecule-metal nanostructures

An important attribute of the optical response of molecular aggregates is their collective optical response. Consider first an atomic or molecular assembly without the metal component. Systems relevant to the present discussion are encountered in optical studies of molecular dye aggregates [87] on one hand, and in studies of optical properties of low dimensional (layers and dots) semiconductor structures [88, 89] on the other, although other interesting systems such as dye containing microdroplets can be investigated along similar lines [90–93]. The simplest model pertaining to our applications are studies of the optical response of assemblies of two-level atoms [94–99]. In his seminal paper, Dicke [100] has shown that, because

<sup>8</sup> In standard applications  $\varepsilon_s$  is considered real.

<sup>9</sup> This is true also for many treatments of SERS, with the additional attribute that the dipole moment is assumed to depend on the nuclear coordinate(s).

of their mutual interaction with the radiation field, a cluster of emitters has some modes that can emit cooperatively with rates that scale with the number of atoms, so called superradiant modes, while other modes are only weakly coupled to the radiation field. Closely related is superfluorescence [101], where a system of initially uncorrelated excited emitters develops coherence through their mutual interaction with the radiation field. Prasad and Glauber [94–97] have analyzed in detail the emission properties of such slabs and spheres of two-level emitters under conditions of (a) weak excitation (namely, the system remains close to its ground state so only its linear response is considered); (b) continuum approximation—assuming the system is dense enough to allow smoothing of its atomistic structure and considering it as a continuous polarizable medium; (c) timescale separation between the atomic resonance frequency (the spacing between the atomic levels) and the emission dynamics, as well as between this dynamics and the time it takes light to cross the system; and (d) phase destroying processes such as Doppler or collisional broadening are ignored. Under these assumptions they were able to describe the emission properties of such systems in terms of eigenstates of an integral equation for the system polarization, showing that a few of these eigenstates behave as superradiant modes, emitting at a rate that scales linearly with the number of atoms. All other modes have zero (in the limit of small clusters) decay rates or infinite lifetimes. Similarly, Svidzinsky and coworkers [98] have studied an  $N$ -atom cluster of linear size  $R$  with only one atom excited in the initial state, and have shown that in the small cluster limit ( $k_0 R \rightarrow 0$ ;  $k_0 = \omega_0/c$  where  $\omega_0$  and  $c$  are the resonance frequency and the speed of light, respectively) only one state of this system can emit with rate  $\sim \gamma_R N$  ( $\gamma_R$  being the radiative decay rate of a single excited atom) while the others have infinite lifetimes. In the opposite case of large clusters there are many superradiant states with relaxation rates  $\sim \gamma_R N / (k_0 R)^2$ . We note in passing that other types of coherent dynamics such as soliton-like exciton propagation [102], lasing [103] and Bose–Einstein condensation [104] have been discussed. On the other hand, dephasing phenomena and disorder can change the qualitative behavior of such systems, and energy transfer in excitonic systems can become diffusive on timescales shorter than their radiative emission, with typical coherence lengths of the order of  $\sim 100$  nm. (See e.g [105, 106].)

Next, consider the interaction of such an aggregate of emitters with a plasmon-sustaining interface (Pockrand *et al* [107] was perhaps the first publication to focus attention on such systems. See [108] for a recent review). In accord with the single emitter case discussed above, standard spectroscopic properties—absorption, emission and lifetimes are modified [109–121]. Of particular interest are observations of plasmon effects on interaction between emitters. The simplest manifestation of such effects is the plasmon-induced enhancement of energy transfer between emitters [62, 79, 122–148]. This can be used in conjunction with metal configuration that supports sub-wavelength waveguiding to direct exciton propagation in predetermined ways [149–163]. This plasmon enhanced energy transfer implies that intersite excitonic coupling is effectively enhanced by coupling to the underlying plasmons,

which implies that exciton-plasmon coupling should also affect superradiance and superfluorescence from excited emitter aggregates. References [70, 71, 134, 164–171] have shown that interatomic (or intermolecular) interaction via coupling to plasmons can dominate the formation of cooperative response over the standard coupling to the free radiation field, and leads to qualitatively similar behavior as described above—a few modes of the molecular/atomic aggregate are superradiant while the others can be strongly sub-radiant. Plasmonic metal structures were indeed shown to enhance the collective nature of emission from emitter aggregates [172].

While the above discussion has distinguished between inter-emitter coupling induced by mutual coupling to the radiation field or to surface plasmons, it is important to emphasize that the physics of these phenomena is essentially the same, and the dominance of coupling to plasmon mode results from the focused local nature of the latter. All phenomena associated with exciton-plasmon coupling, including enhanced cooperative emission and enhanced exciton transport, have their analogs in excited molecules and molecular assemblies interacting with optical modes localized in cavities and other nanostructures such as photonic crystals, where molecule-radiation field coupling can be tuned by geometrical characteristics of the systems [173–175].

### 1.5. Strong coupling

The consequences of interaction between molecules and plasmon-supporting metal surfaces have so far been discussed in terms of modified molecular properties—absorption, scattering, and relaxation rates. A growing attention is given in recent years to another manifestation of this interaction (and the equivalent phenomenon in systems comprised of molecules or semiconductor quantum dots and cavity-confined radiation field modes) loosely referred to a ‘strong coupling’, where the focus is on the hybridization between the material and optical modes to form hybrid states that comprise both [176]. An example is shown in figure 4. Two LSPP modes of two nanoparticles are formed by combining the LSPP modes of a spherical nanoparticle corresponding to bonding and anti-bonding states. Treating plasmons as incompressible deformations of electron gas and calculating the total electrostatic energy of the system one obtains a set of coupled equations on amplitudes of deformation fields describing LSPP modes of the combined system [15, 18].

An often encountered model used to explain this aspect of intersystem coupling comprises two coupled classical harmonic oscillators  $A$  and  $B$  [177]. The corresponding Hamiltonian

$$H = \frac{P_A^2}{2m_A} + \frac{P_B^2}{2m_B} + \frac{1}{2}k_A X_A^2 + \frac{1}{2}k_B X_B^2 + \frac{1}{2}\kappa(x_A - x_B)^2 \quad (14)$$

can be expressed in terms of two independent normal modes of frequencies

$$\omega_{\pm}^2 = \frac{1}{2} \left( \omega_A^2 + \omega_B^2 \pm \sqrt{(\omega_A^2 - \omega_B^2)^2 + \frac{4\kappa^2}{m_A m_B}} \right) \quad (15)$$

with

$$\omega_N = \sqrt{\frac{k_N + \kappa}{m_N}}; \quad N = A, B. \quad (16)$$

Plotting the frequencies  $\omega_+$  and  $\omega_-$  against  $\omega_B$  while keeping  $\omega_A$  constant shows a typical coupling induced avoided crossing (see figure 5): When  $\kappa = 0$  the two lines are: a horizontal one,  $\omega_+ = \omega_A$  ( $\kappa = 0$ ) indicating that this root does not depend on  $\omega_B$  and the line  $\omega_- = \omega_B$  ( $\kappa = 0$ ) with slope 1 that correspond to the linear dependence of this root on  $\omega_B$  obviously cross at  $\omega_B = \omega_A$ . When  $\kappa \neq 0$  the lines avoid each other and achieve minimum difference  $(\omega_+^2 - \omega_-^2)_{\min} = 2\kappa/\sqrt{m_A m_B}$  and strong mixing when  $\omega_B = \omega_A$ . A familiar analogous situation is the two-level emitter in quantum mechanics, where diagonalizing the Hamiltonian

$$\begin{aligned} \hat{H} &= \hat{H}_0 + \hat{V}, \\ \hat{H}_0 &= E_A |A\rangle \langle A| + E_B |B\rangle \langle B|, \\ \hat{V} &= V_{AB} |A\rangle \langle B| + V_{BA} |B\rangle \langle A| \end{aligned} \quad (17)$$

yields the eigenvalues

$$E_{\pm} = \frac{E_A + E_B \pm \sqrt{(E_A - E_B)^2 + 4|V_{AB}|^2}}{2} \quad (18)$$

with a minimum spacing (the so called Rabi splitting)  $2|V_{AB}|$ . Yet another familiar system is the Jaynes–Cumming model [178] that describes coupled two-level system and a quantum harmonic oscillator

$$\hat{H} = \hbar\omega\hat{a}^\dagger\hat{a} + E_1 |1\rangle \langle 1| + E_2 |2\rangle \langle 2| + \frac{1}{2}U(\hat{a}^\dagger |1\rangle \langle 2| + \hat{a} |2\rangle \langle 1|). \quad (19)$$

This model appears more relevant to our notion of a molecule (represented by a two-level system) coupled to a plasmon (described as a harmonic oscillator). However, the conservation of excitation

$$\langle \hat{a}^\dagger \hat{a} \rangle + \langle |2\rangle \langle 2| \rangle = \text{constant} \quad (20)$$

that follows from (19), implies that the states of this Hamiltonian correspond to an infinite set of coupled two-level systems that are distinguished by the number of harmonic oscillator quanta that are present when the actual two-level system is in state 1. Each such a pair is thus described by the Hamiltonian (17) where  $|A\rangle = |1, n\rangle$ ,  $|B\rangle = |2, n-1\rangle$  while  $V = U\sqrt{n}$ . A new element is that the Rabi splitting is here proportional to  $\sqrt{n}$ , namely the amplitude of the harmonic subsystem. In addition, from the discussion above, following, e.g. [94–100],  $\hat{V}$  is also expected to scale like  $\sqrt{N}$  where  $N$  is the number of molecules within a volume much smaller than the radiation wavelength that are coherently involved in the process.

These models serve to understand observations of mode coupling in optical response of composite nanosystems, ranging from plasmon hybridization<sup>10</sup> in nanoparticle systems

<sup>10</sup> The term ‘hybridization’ arises from the theoretical approach that qualitatively (and quantitatively in the linear regime) describes SPP modes supported by a complex system using a simple analogy with the hybridization of molecular orbitals in quantum chemistry.

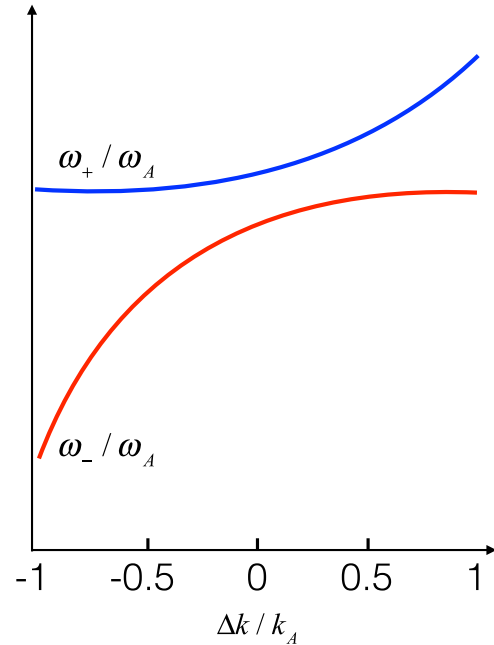


**Figure 5.** The normal mode frequencies of a system of two linearly coupled harmonic oscillators plotted against the difference  $\Delta k = k_B - k_A$  between the force constants of the free oscillators.

[15–18, 179–187], to molecules, molecular assemblies, and semiconductor nanodots interacting with plasmons excited in metal nanostructures [55, 158, 188–202] as well as cavity modes [178, 203–210]. For recent reviews see [108, 175] and [211].

An example for this behavior is shown in figure 6. In later parts of this review we focus on the computational and theoretical analysis of these phenomena in coupled exciton-plasmon systems. Figure 6 demonstrates the qualitatively similar behavior in coupled plasmon systems comprising metallic nanostructures. Specifically we focus on a simple system made of two closely spaced gold nanowires with characteristic lengths less than the incident wavelength schematically depicted in figure 6(a), and consider the linear optical response of this system to two different excitations, namely a conventional incident plane wave and a local dipole source. When the system is excited by the plane wave polarized along the axis connecting two wires the scattering intensity exhibits a single resonance that shifts to higher energies as the gap size increases (figure 6(b)). This is to be expected since the incident field excites longitudinal LSPP modes in each wire and their interaction strength drops as the gap widens. The energy of the resonant mode approaches a limit of a single wire as clearly seen in figure 6(b). It is not surprising to see only a single mode since another hybrid state is the dark (anti-bonding) mode which is not accessible due to symmetry when the system is uniformly excited by the plane wave (see figure 4). Dark states however can be excited when a local dipole source is utilized (figure 6(c)). Here both bonding and anti-bonding hybrid states are seen in the transmission spectra. Using the language of strong coupling physics, the transmission spectra exhibit Rabi splitting that is determined by the strength of the electromagnetic (EM) interaction between LSPP modes



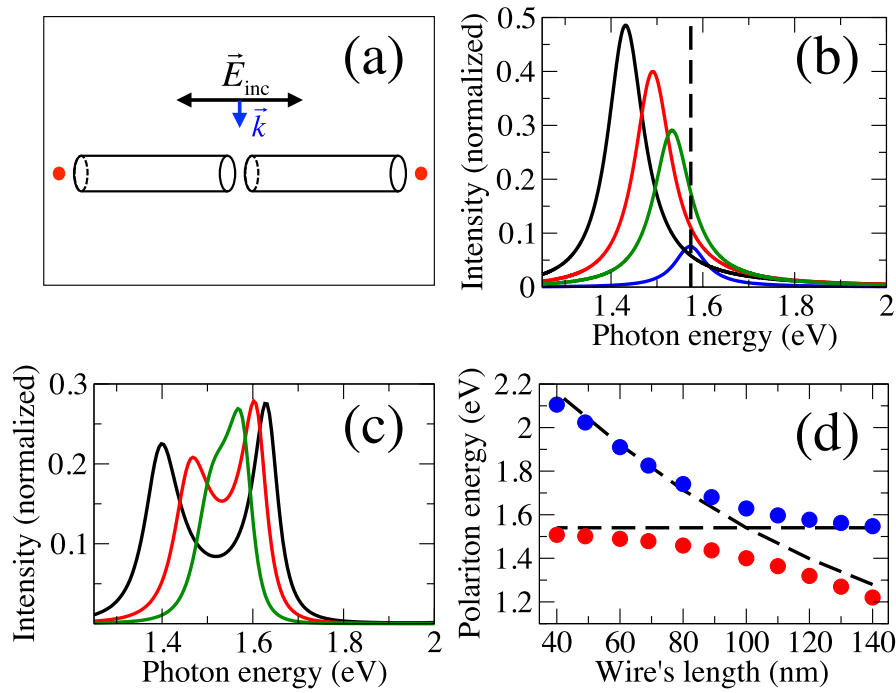


**Figure 6.** Two gold nanowires separated by a sub-diffraction gap. Panel (a) schematically depicts two wires. Two red dots indicate local dipole source and local detection point. This excitation scheme is compared to the conventional plane wave. Panel (b) shows scattered EM intensity detected in the far field when the wires are excited by a plane wave. Blue line shows data for a single 100 nm long wire; black line shows data for the gap of 10 nm, red line—20 nm, green line—40 nm. Both wires are 100 nm long with a diameter of 20 nm. Panel (c) shows results for the case where the wires are excited by a local dipole placed 5 nm away from one of the wires. Different colors correspond to the same values of the gap as in panel (b). Panel (d) shows energies of hybrid plasmon states (red and blue dots) as functions of the length of one of the wires (another wire’s length is fixed at 100 nm). Dashed curve corresponds to the energy of the longitudinal plasmon of a single wire.

of each wire. Reflecting their relative energies (figure 4), the bonding and anti-bonding hybrid states are referred to as the lower and upper polaritons, respectively. The energy separation of these states increases as the gap between wires narrows, indicating the fact that the EM coupling strength increases. Figure 6(d) explores the anti-crossing behavior of the hybrid states when the length of one of the wires is varied. Without EM coupling between the wires the longitudinal LSSP mode of one wire would cross the energy of the LSSP mode of another as dashed lines in figure 6(d) illustrate. The coupling results in the avoided crossing behavior typical for strongly coupled systems.

We note that the observed Rabi splitting for the wires of 100 nm in length is 240 meV corresponding to the characteristic time of EM energy exchange between plasmonic particles of 17 fs. Such a fast dynamics calls for the utilization of plasmon modes (both bright and dark as we shall see below) as nano-optical probes [212] to investigate fundamentals of light–matter interaction.

Coming back to theoretical descriptions, to provide a complete qualitative understanding of these phenomena the models represented by equations (14) and (17) have to be supplemented by proper descriptions of damping on one hand, and the probe used for the actual observation on the other. To show the consequence of taking these into account consider the model of figure 7 in which the two-level model of equation (17) is augmented by (a) having each of the two levels damped by coupling it to its own continuum and (b) having the absorption lineshape of this system probed by a photon

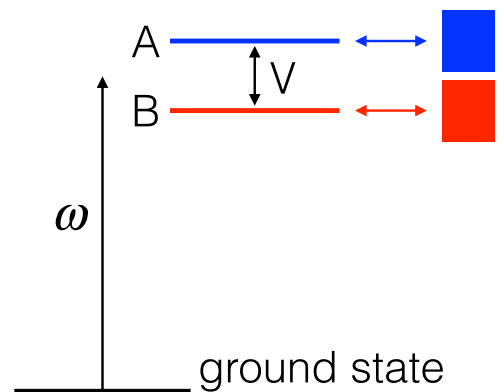


**Figure 7.** A model illustrating the consequence of coupling between two absorption resonances whose widths are determined by coupling to dissipating continua. At issue is the question whether their mutual coupling  $V$  is strong enough to keep them sufficiently apart so that two peaks are observed for all possible values of  $E_A - E_B$ .

coming from the far field and coupled to the system by some dipole operator  $\mu$ . As a primitive model of observation of such phenomena in coupled exciton-photon systems, level A can be a single exciton state and level B a single plasmon state (or a cavity mode), both accessible from the ground state (unexcited molecule-metal/cavity composite) and characterized by their mutual coupling  $V$  and lifetimes associated with their damping to their environments. (Typical plasmon lifetimes are 50 fs and those of cavity modes, determined by the cavity  $Q$  number, are much longer.) Exciton lifetimes are bounded

from below by the radiative decay process, of order of 1 ns in free space and possibly considerably longer in cavity environments, however such lifetimes are made considerably shorter by radiationless relaxation into environmental modes including the close-by metal interface). Denoted these damping rates by  $\gamma_A$  and  $\gamma_B$ , the absorption lineshape is obtained in the form

$$L(\omega) = \text{Im} \frac{F}{(\hbar\omega - E_A + (i/2)\gamma_A)(\hbar\omega - E_B + (i/2)\gamma_B) - |V_{AB}|^2} \quad (21)$$

$$= \text{Im} \frac{F(\omega)}{(\hbar\omega - E_+)(\hbar\omega - E_-)} = \frac{F(\omega)(\hbar\omega - E_+^*)(\hbar\omega - E_-^*)}{|(\hbar\omega - E_+)|^2 |(\hbar\omega - E_-)|^2},$$

where

$$F(\omega) = |\mu_{GA}|^2 (\hbar\omega - E_B + (i/2)\gamma_B) + |\mu_{GB}|^2 (\hbar\omega - E_A + (i/2)\gamma_A) - \mu_{GA}V_{AB}\mu_{BG} - \mu_{GB}V_{BA}\mu_{AG} \quad (22)$$

and  $E_{\pm}$  are given by equation (18) with  $E_A$  and  $E_B$  are replaced by  $E_A - (i/2)\gamma_A$  and  $E_B - (i/2)\gamma_B$ , respectively.

When  $E_A$  is far from  $E_B$  ( $|E_A - E_B| \gg |V_{AB}|$ ) the lineshape (21) clearly shows two maxima, near  $\hbar\omega = E_A, E_B$ . As  $E_B$  changes and approaches  $E_A$  these maxima come closer and may either coalesce into a single maximum or remain separated if the coupling  $|V_{AB}|$  is large enough. At issue is the question whether this lineshape shows one or two maxima when they are at their closest approach. For a quick estimate we can proceed with the following simplifications: take  $\gamma_A = \gamma_B \equiv \gamma$  and assume that the structure of the lineshape is dominated by the denominator  $D(\omega)$  of equation (21):

$$D(\omega) = \left[ (\hbar\omega - E_0 - \eta)^2 + (1/2)\gamma^2 \right] \times \left[ (\hbar\omega - E_0 + \eta)^2 + (1/2)\gamma^2 \right], \quad (23)$$

where  $E_0 = (1/2)(E_A + E_B)$  and  $\eta = (1/2)\sqrt{(E_A - E_B)^2 + 4|V_{AB}|^2}$ . The condition for this function to have two distinct minima is that it has a maximum at  $\hbar\omega = E_0$ , namely  $[d^2D/d\omega^2]_{\omega=\hbar^{-1}E_0} < 0$ . This translates into

$$\gamma < \sqrt{(E_A - E_B)^2 + 4|V_{AB}|^2} \quad (24)$$

so that the condition for a split peak at the closest approach  $E_A = E_B$  is

$$\gamma < 2|V_{AB}|. \quad (25)$$

Situations where this condition is met are referred to as ‘strong coupling’, however it should be kept in mind that ‘strong’ implies that  $|V_{AB}|$  is large relative to not only lifetime broadening as described above, but in fact to any other type of homogeneous and inhomogeneous broadening that can mask the Rabi splitting. To see the implications of this condition, consider first the coupling of a molecule to an unpopulated cavity mode. The coupling strength (Rabi frequency) implied by equation (10) is of order (taking  $\varepsilon_r = 1$ )

$$V = \mu\sqrt{\hbar\omega/2\varepsilon_0\Omega}, \quad (26)$$

where  $\mu$  and  $\omega = 2\pi c/\lambda$  are the dipole matrix element and the frequency for the molecular transition, and  $\Omega$  is the cavity volume. Taking  $\Omega = \lambda^3$  and using  $\mu = 1$  Debye leads to

Rabi frequency of the order of  $\sim 1$  wavenumber ( $10^{-4}$  eV). Compared to this, the damping rate of cavity modes can be relatively negligible, and radiative decay rates of molecular excitations are also 2–3 orders of magnitude smaller (and may be further reduced due to the cavity Purcell effect [213]). This implies that molecule-cavity mode systems can often be found in the strong coupling limit. When an aggregate of many molecules is involved the effective Rabi frequency may increase by 1–2 orders of magnitude, to the level observed in some experiments due to cooperative molecular response.

For a molecule interacting with the dipolar ( $l = 1$ ) plasmon of a small metal nanoparticle we can make an equivalent consideration using equation (6) and  $\mathbf{E} = -\nabla\Phi$  to obtain the molecule (again represented by its transition dipole  $\mu$ )—plasmon interaction. For a small molecule<sup>11</sup> outside a metal sphere of radius  $a$  at a distance  $R > a$  from the sphere center perpendicular to the sphere surface this leads to [12, 13]

$$V = \mu\left(\frac{a}{R}\right)^3 \sqrt{\frac{3\hbar}{2\pi\varepsilon_0 \text{Re}\varepsilon_r'(\omega_p) a^3}} \quad (27)$$

with  $\varepsilon_r'(\omega) = d\varepsilon_r/d\omega$ ,  $\omega_p$  is obtained from (see equation (8))  $\text{Re}(\varepsilon_r(\omega_p)) = -2$  and all distances are assumed small relative to  $\lambda_p = 2\pi c/\omega_p$ . Compared to equation (26) we see a similar structure with elements of differences:  $\omega$  is replaced by  $\varepsilon_r'(\omega_p)^{-1}$  and the cavity volume is replaced by the particle volume (a similar conclusion regarding the volume was reached in [201] following the analysis of [214]). In addition, the factor  $(a/R)^3$  introduces an explicit dependence on the molecule-sphere distance.

Because  $a$  can be far smaller than the radiation wavelength, the Rabi frequency near plasmonic particles can be considerably larger than that characterizing coupling to cavity modes. Indeed, for silver  $\hbar(d\varepsilon/d\omega)_{\omega_p}^{-1}$  is of order 5 eV and for a molecule of  $\mu = 10$  D near a silver sphere of radius  $a = 4$  nm we find  $V \sim 0.1$  eV. On the other hand, the damping in this case is also much larger. It is usually dominated by the dipolar plasmon lifetime, of the order 50 fs for silver, corresponding to  $\gamma \sim 0.1$  eV<sup>12</sup>. We conclude that strong coupling can be realized in such situations as well, in agreement with the observation of [201], although achieving it requires more fine-tuning of system parameters than in the molecule-cavity case.

Like the plasmon coupling example of figure 6, most demonstrations of strong coupling between molecules and optical modes have focused on the phenomenon of avoided crossing and similar manifestations (e.g. Fano lineshapes) in light scattering spectra. However other observations should be noted:

- (a) Obviously, the energetic structure predicted by these models, as exemplified in figure 6, also implies the possibility to observe temporal (Rabi) oscillation in the time domain. Actual observations of such oscillations in

<sup>11</sup> The result (27) assumes a point-like molecule located at distance  $R$  from the sphere center.

<sup>12</sup> When the molecule sits directly on the metal surface, energy and electron transfer to the metal provide other efficient relaxation routes with relaxation times possibly of similar order.

ultrafast optical response of such systems have been rare. A recent work by Vasa *et al* describes such an observation [198].

- (b) The two-level and harmonic oscillator models discussed above provide a useful but by no means complete picture of strongly coupled systems. In particular, the consequences of the vibrational motions in the molecular subsystems can be observed [215, 216] and should be included in a complete analysis of such strongly coupled systems [217].
- (c) In analyzing some of these examples of mode hybridization, the focus is on coupling between molecular excitations and optical/plasmon modes. At close proximity the possibility of electron tunneling between metal structures can considerably change the physics of the system and should be taken into account [21, 22, 218]. Similarly, electron transfer can strongly affect metal-molecule interaction at short distances and overshadows the effect of exciton-plasmon coupling. Indeed, plasmon-induced hot electron chemistry—processes in which following plasmon excitation electrons are exchanged between the metal and molecules are currently drawing increasing attention [219–235]. (See also [236–242] for recent theoretical work and [14, 243, 244] and [245] for reviews.)
- (d) Other important effects of such coupling have been observed and discussed. These include behaviors that reflect the modification of molecular electronic structure and dynamics [246–252], spin relaxation [253–255], metal work functions [256], modification of electron and exciton transport properties because of interaction with cavity modes [206, 207, 257] as well as nonlinear phenomena, e.g. induced transparency [258, 259] and second harmonic generation [260, 261] in coupled exciton-plasmon systems.

The simple theoretical considerations outlined above provide a qualitative understanding of many of the observed phenomena, however to understand the detailed behavior of actual experimental systems involving complex metal structures and an assembly of interacting molecules we need to resort to numerical studies. The rest of this review is aimed to provide a detailed account of the current state of the art of such studies.

## 2. Theoretical background for the numerical approach

Numerical simulations of atomic, molecular or semiconductor systems coupled to the radiation field have been done for a long time in different contexts [101, 262–275]. Including plasmon-sustaining metal nanostructures is a fairly recent development [273]. Below we refer to such systems as coupled exciton-plasmon systems. In what follows we describe the theoretical basis for simulating the dynamics and optical response of such systems, namely the ways by which the EM field, the molecular system, the metal, and the coupling

between them are accounted for. The actual implementation of these descriptions in numerical solvers is described in the next section.

### 2.1. The electromagnetic field

In the vast majority of systems considered here the EM radiation can be treated classically using Faraday's and Ampere's laws

$$\begin{aligned}\frac{\partial \mathbf{B}}{\partial t} &= -\nabla \times \mathbf{E}, \\ \frac{\partial \mathbf{D}}{\partial t} &= \frac{1}{\mu_0} \nabla \times \mathbf{B},\end{aligned}\quad (28)$$

where  $\mu_0$  is magnetic permeability of free space and the electric displacement field is defined as

$$\mathbf{D} = \epsilon_0 \mathbf{E} + \mathbf{P}. \quad (29)$$

The macroscopic polarization,  $\mathbf{P}$ , is the essence of semiclassical theory of optical properties of exciton-plasmon materials. It is induced in a material subsystem by the EM field and in turn drives the EM field through the current density  $\mathbf{J}(\mathbf{r}, t) = \partial \mathbf{P}(\mathbf{r}, t) / \partial t$ .

### 2.2. The metal

In the simulations described below the metal is described as a continuum dielectric with a dielectric function given by the Drude (equation (1)) or Lorentz (equation (2)) models with suitably chosen parameters. Such parameters for several metals are given in [5]. The advantage of using these models is that their effect can be described by adding auxiliary variables governed by Markovian dynamical equations to the description of the system dynamics. The specific equations that govern the dynamics of the current density depend on a choice of a dielectric function and are discussed in section 3.

### 2.3. The molecular system

The simplest description of a molecular system accounts for its response to the radiation field in terms of a local dielectric function that can be described by a Lorentz model with suitably chosen parameters. With this approach, the numerical solution of coupled exciton-plasmon systems is reduced to solving the Maxwell equations in a continuous non-homogeneous dielectric. Such a description of the molecular system suffers from two shortcomings: First, it has to include some procedure to account for the molecular density and local orientation within the Lorentz parameters, and second, while it contains phenomenological damping parameters, it cannot distinguish between the effect of population relaxation (so called  $t_1$  processes) and dephasing ( $t_2$  processes), namely it cannot explicitly account for pure dephasing.

Both orientation effects and molecular density can be described in a classical microscopic description, in which individual molecules (or, in a coarse-grained description, different cells of a numerical grid) are described as Lorentz oscillators with suitably chosen parameters [276].

These oscillators, describing molecular dipoles, do not directly interact with each other. Rather, a mutual interaction is affected through their interaction with the EM field<sup>13</sup>.

The effect of pure dephasing, as a process different from excitation relaxation, can be accounted for by describing the molecular sub-system as a collection of quantum mechanical entities, albeit in a *mean-field approximation*. To describe this procedure we start with the Hamiltonian written as a sum of a molecular part  $\hat{H}_M = \sum_m \hat{h}_m$ , the radiation field  $\hat{H}_R$  and their interaction  $\hat{H}_{MR} = \sum_m \hat{H}_{mR}$ , where the sums are taken over individual molecules.

$$\hat{H} = \hat{H}_M + \hat{H}_R + \hat{H}_{MR}. \quad (30)$$

In  $\hat{H}_{mR} = -\mathbf{E}(\mathbf{r}_m) \cdot \hat{\boldsymbol{\mu}}_m$  the electric field at the position of the molecule  $m$  depends on the states of all other molecular dipoles. The molecular density matrix evolves according to the Liouville equation

$$\frac{d\hat{\rho}}{dt} = -\frac{i}{\hbar} [\hat{H}, \hat{\rho}]. \quad (31)$$

Now assume that  $\hat{\rho} = \prod_m \hat{\rho}_m$  with  $\text{Tr}_m \hat{\rho}_m = 1$ . Using this in (31) and taking trace over all molecules except  $m$  leads to

$$\frac{d\rho_m}{dt} = -\frac{i}{\hbar} \left[ \hat{h}_m - \langle \mathbf{E}(\mathbf{r}_m) \rangle \cdot \hat{\boldsymbol{\mu}}_m, \hat{\rho}_m \right] \quad (32)$$

with  $\langle \mathbf{E}(\mathbf{r}_m) \rangle = \text{Tr}' \left( \mathbf{E} \prod_{m' \neq m} \hat{\rho}_{m'} \right)$  where  $\text{Tr}'$  represents trace over the states of all molecules except  $m$ . The Liouville–von Neumann equation (32) describes the dynamics of a single molecular dipole under the influence of the local average electric field at the position of this dipole. The latter includes the incident field and the average field of all other molecules. For a single molecule within an ensemble of two-level ( $\varepsilon_1, \varepsilon_2$ ) molecules, equation (32) yields (see also [277])

$$\begin{aligned} \frac{d\rho_{11}}{dt} &= -i \frac{\mathbf{E}\boldsymbol{\mu}_{12}}{\hbar} (\rho_{12} - \rho_{12}^*), \\ \frac{d\rho_{12}}{dt} &= i \left[ \frac{\mathbf{E}\boldsymbol{\mu}_{12}}{\hbar} (\rho_{22} - \rho_{11}) + \Omega_{12} \rho_{12} \right], \\ \frac{d\rho_{22}}{dt} &= i \frac{\mathbf{E}\boldsymbol{\mu}_{12}}{\hbar} (\rho_{12} - \rho_{12}^*), \end{aligned} \quad (33)$$

where 1 and 2 denote the ground and the excited state, respectively,  $\boldsymbol{\mu}_{12}$  is the corresponding transition dipole moment (assumed real), and  $\Omega_{12} = (\varepsilon_2 - \varepsilon_1) / \hbar$  is the transition frequency. Another often encountered form of equations (33) is obtained by defining  $X = \rho_{12} + \rho_{12}^*$ ,  $Y = \rho_{12} - \rho_{12}^*$  and noting that  $dX/dt = i\Omega_{12}Y$ . This leads to

$$\begin{aligned} \frac{d\rho_{11}}{dt} &= -\frac{1}{\Omega_{12}} \frac{dX}{dt} \frac{\mathbf{E}\boldsymbol{\mu}_{12}}{\hbar}, \\ \frac{d\rho_{22}}{dt} &= \frac{1}{\Omega_{12}} \frac{dX}{dt} \frac{\mathbf{E}\boldsymbol{\mu}_{12}}{\hbar}, \\ \frac{d^2X}{dt^2} &= -\Omega_{12}^2 X + 2\Omega_{12} \frac{\mathbf{E}\boldsymbol{\mu}_{12}}{\hbar} (\rho_{11} - \rho_{22}). \end{aligned} \quad (34)$$

<sup>13</sup> It is important to emphasize that this statement holds only for interaction within the frequency range accounted for by dynamical coupling with the classical electromagnetic field. Electrostatic interactions and van der Waals forces are also mediated by the ambient electromagnetic field but cannot be accounted for on the level of these simulations. If such interactions are needed they have to be added explicitly.

Next we (a) multiply these equations by the molecular density  $n_M$  and the last equation also by  $\boldsymbol{\mu}_{12}$ , (b) denote the densities of molecules in states 1 and 2 by  $n_M \rho_{11} = n_1$ ;  $n_M \rho_{22} = n_2$  ( $n_1 + n_2 = n_M$ ) and the polarization by  $X n_M \boldsymbol{\mu}_{12} = \mathbf{P}$ , and (c) assume an isotropic system and average over all orientations of the molecular dipole to get  $\langle \mu_x \mu_y \rangle = \langle \mu_x \mu_z \rangle = \langle \mu_y \mu_z \rangle = 0$  and  $\langle \mu_j^2 \rangle = (1/3) \mu^2$ ,  $j = x, y, z$ . Equation (34) then become

$$\frac{dn_1}{dt} = -\frac{1}{\hbar \Omega_{12}} \mathbf{E} \cdot \frac{d\mathbf{P}}{dt}, \quad (35)$$

$$\frac{dn_2}{dt} = \frac{1}{\hbar \Omega_{12}} \mathbf{E} \cdot \frac{d\mathbf{P}}{dt}, \quad (36)$$

$$\frac{d^2\mathbf{P}}{dt^2} = -\Omega_{12}^2 \mathbf{P} + \frac{2}{3\hbar} \Omega_{12} \mu_{12}^2 \mathbf{E} (n_1 - n_2). \quad (37a)$$

This form of the Liouville–von Neumann equations, written in terms of the macroscopic populations and polarization, is identical in the absence of relaxation processes, to the kinetic equations (sometimes referred to as rate equations) used in the laser literature [278–280]). We note in passing that the more general form of equation (37) that does not assume isotropy

$$\frac{d^2\mathbf{P}}{dt^2} = -\Omega_{12}^2 \mathbf{P} + \frac{2\Omega_{12}}{\hbar} \boldsymbol{\mu}_{12} (\mathbf{E} \cdot \boldsymbol{\mu}_{12}) (n_1 - n_2) \quad (37b)$$

can be particularly useful for describing interfacial optical response. Equations (37) is the gateway for coupling the Maxwell's equations to dynamics of the molecular system (more on this, including practical numerical algorithms is in the next section). Focusing for now on the 1D case, we find that in the linear regime, where  $n_2 \ll n_1$  so that  $n_1 \sim n_M$ , equation (37b) implies the following expression for the electric susceptibility  $\chi_e(\omega) = P/(\varepsilon_0 E)$

$$\chi_e = \frac{2\mu_{12}^2 n_M}{\hbar \varepsilon_0 \Omega_{12}} \frac{\Omega_{12}^2}{\Omega_{12}^2 - \omega^2}. \quad (38)$$

To account for population relaxation and dephasing one usually introduces phenomenological decay constants in (31) [281]. Here, however, different practices have been used. For the two-level molecular model under discussion, the standard scheme uses Bloch-type equations such as (33)

$$\begin{aligned} \frac{d\rho_{11}}{dt} &= -i \frac{\mathbf{E}\boldsymbol{\mu}_{12}}{\hbar} (\rho_{12} - \rho_{12}^*) + \gamma_{21} \rho_{22}, \\ \frac{d\rho_{12}}{dt} &= i \left[ \frac{\mathbf{E}\boldsymbol{\mu}_{12}}{\hbar} (\rho_{22} - \rho_{11}) + \Omega_{12} \rho_{12} \right] - \frac{\Gamma}{2} \rho_{12}, \\ \frac{d\rho_{22}}{dt} &= i \frac{\mathbf{E}\boldsymbol{\mu}_{12}}{\hbar} (\rho_{12} - \rho_{12}^*) - \gamma_{21} \rho_{22}, \end{aligned} \quad (39)$$

where  $\gamma_{21}$  is the population relaxation rate, while the coherence  $\rho_{12}$  decays with the rate  $\frac{\Gamma}{2} = \frac{\gamma_{21}}{2} + \gamma_d$ , which takes into account pure dephasing rate  $\gamma_d$ . These rates are related to the population relaxation time,  $T_1$ , decoherence time,  $T_2$ , and the pure dephasing time,  $T_2^*$ , in analogy with phenomenological formula from NMR spectroscopy [282]

$$\frac{1}{T_2} = \frac{1}{2T_1} + \frac{1}{T_2^*}. \quad (40)$$

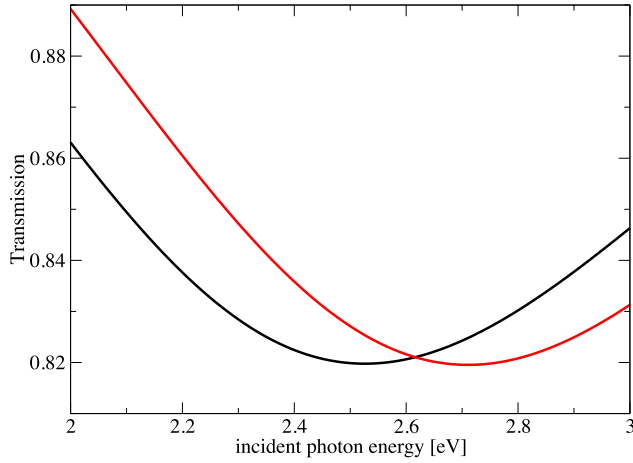


**Figure 8.** Transmission through a 200 nm thin layer of interacting molecules as a function of the incident photon energy. The black line shows results obtained for molecules described by rate equations (42). The red line shows results obtained by applying Bloch equations (39). The molecular transition frequency is 2.5 eV, the decay rate is 1 eV, the transition dipole moment is 10 Debye, and molecular number density is  $10^{26} \text{ m}^{-3}$ .

Starting from (39) and following the procedure that leads to equation (37b) now leads to the linear electric susceptibility in the form

$$\chi_e = \Delta\varepsilon \frac{\Omega_{12}^2}{\Omega_{12}^2 - (\omega - i\frac{\Gamma}{2})^2}, \quad (41)$$

where we use the notation  $\Delta\varepsilon = \frac{2\mu_{12}^2 n_M}{\hbar\varepsilon_0 \Omega_{12}}$ .

Another common phenomenological approach to account for relaxation, apart from the population relaxation rate  $\gamma_{12}$  is to add a damping term to the polarization equation (37), hence replacing equations (35)–(37) by [278–280]

$$\begin{aligned} \frac{dn_1}{dt} - \gamma_{21}n_2 &= -\frac{1}{\hbar\Omega_{12}}\mathbf{E} \frac{d\mathbf{P}}{dt} \\ \frac{dn_2}{dt} + \gamma_{21}n_2 &= \frac{1}{\hbar\Omega_{12}}\mathbf{E} \frac{d\mathbf{P}}{dt}, \\ \frac{d^2\mathbf{P}}{dt^2} + \Gamma \frac{d\mathbf{P}}{dt} + \Omega_{12}^2\mathbf{P} &= \frac{2}{\hbar}\Omega_{12}\mu_{12}^2 (n_1 - n_2)\mathbf{E}. \end{aligned} \quad (42)$$

The linear electric susceptibility as follows from (42) reads

$$\chi_e = \Delta\varepsilon \frac{\Omega_{12}^2}{\Omega_{12}^2 + i\Gamma\omega - \omega^2}, \quad (43)$$

which is different from (41). The susceptibility obtained from the Liouville–von Neumann equation differs from the conventional Lorentzian profile (43) at high dephasing rates resulting in noticeable red shift of the resonance from the molecular transition energy.

Figure 8 demonstrates that models (39) and (42) lead to noticeably different results even in linear regime at high damping. The linear transmission through a thin layer of interacting molecules is evaluated using both Bloch and rate equations. It is clear that data obtained using the Bloch model are red shifted compared to the model based on rate equations.

When molecules are located near a metal interface (a metal nanoparticle, arrays of such particles, arrays of holes, etc) one

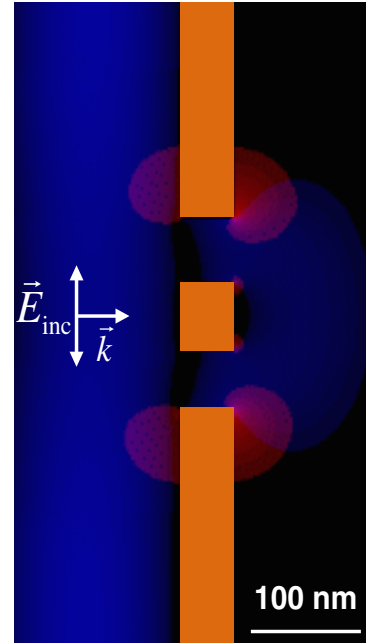


**Figure 9.** Two sub-diffraction slits in thin silver film. The system is excited by a resonant plane wave. Blue color shows instantaneous electromagnetic intensity associated with the vertical electric field component, while red indicates the induced horizontal component.

should pay attention to the local field polarization, which is in general nonlinear and time dependent when an SPP mode is excited. This is illustrated with an example of a double-slit system as shown in figure 9. When excited by a resonant incident field the corresponding SPP mode is launched on both input and output sides of the film. Most importantly, the spatial regions near the slits that are displayed with red and blue colors correspond to the local EM with horizontal and vertical polarization components. With molecules deposited on either side of the film this should be carefully taken into account.

The extension of the model based on rate equations to the case of exciton-plasmon materials with a local field being of arbitrary polarization is straightforward [283]. However, the density matrix approach explicitly takes into account a particular configuration of the excited state wavefunction, which in turn determines the coupling with the local EM field. As frequently implemented, the Hamiltonian of a molecule is written in the basis of angular momentum states such that the dipole coupling with a local electric field usually given as a solution of Maxwell's equations in Cartesian coordinates must be written in spherical coordinates [273, 284]. Alternatively one may work in Cartesian coordinates for both the EM field and the molecular dynamics, facilitated by operating in the basis of  $s$ ,  $p$  orbitals. One can also invoke symmetry group algebra [265].

### 3. Numerical modeling

Due to the complex structure of modern plasmonic materials, it is only for a small number of geometries that one can, in principle, solve the Maxwell equations analytically in terms of the EM field modes. More often than not it is required to numerically integrate Maxwell's equations (28) for the specific structure and the given environment. Moreover, when dealing with

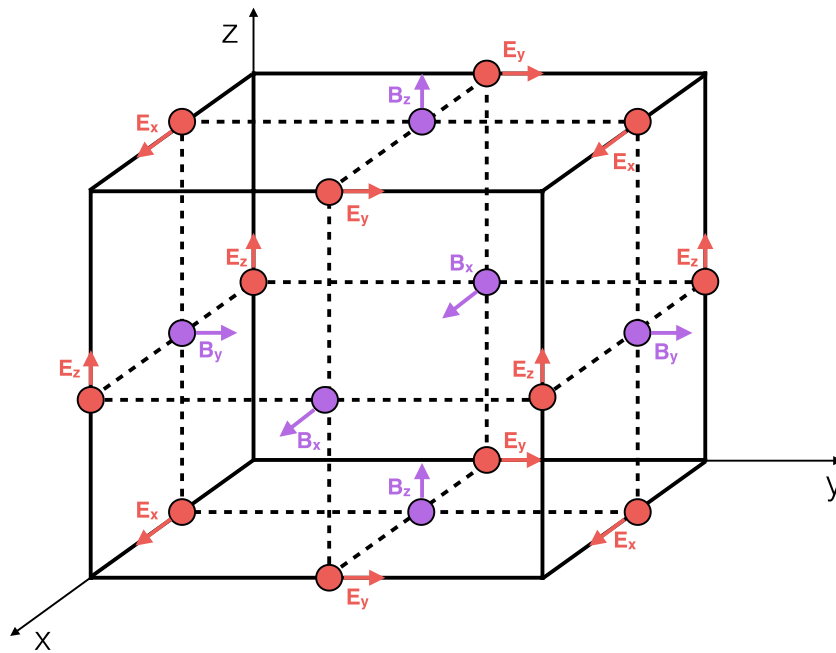


**Figure 10.** Yee's cell with the origin corresponding to the spatial point described by three integers  $(i, j, k) = (x_i, y_j, z_k)$  located on the lattice. The side of the cube along each direction corresponds to the spatial step along this direction.

hybrid systems comprising molecules near plasmonic interfaces such as nanoparticles, in particular under strong coupling conditions, a more involved theory requires numerical integration of the coupled Maxwell–Bloch equations. It is thus important to have access to spatiotemporal dynamics of EM field. There are various numerical methods available for numerical integration of Maxwell's equations on a grid [285, 286]. This part of the review discusses in depth one of many methods, namely finite-difference time-domain approach (FDTD). In addition to applications of FDTD in plasmonics we also provide several working FORTRAN codes, which can be found in supplemental material section ([stacks.iop.org/JPhysCM/29/443003/mmedia](http://stacks.iop.org/JPhysCM/29/443003/mmedia)). The supplied codes correspond to various applications discussed in details in sections 2 and 4.

### 3.1. FDTD and programming aspects

Consider a system of Maxwell's equations (28) here in an inhomogeneous space occupied by different dielectric components whose optical responses are determined by the local polarization currents. An attractive feature of solving Maxwell's equations directly instead of propagating a wave equation is a better numerical convergence, since equation (28) are first order equations unlike the wave equation. In a standard numerical approach one sets a numerical grid over the system and represents the curl operators in the Maxwell equations by finite differences at any grid point. When the dielectric function is location dependent such an approach requires an additional effort in order to account for proper boundary conditions at dielectric interfaces [6]. Such a task becomes very involved when dealing with complex geometries. It was shown, however, that specifically displacing the electric and magnetic field components with respect to each other, one can always satisfy the boundary conditions at every grid point. This scheme was put forward by Kane Yee in

his seminal paper in 1966 [287] and later on was further developed by Allen Taflové [288].

Figure 10 illustrates the unit cell (so-called Yee's cell), which is at the heart of the FDTD scheme and the basis for all the codes that accompany this review. The lattice is defined by a set of points, each given in terms of three integers  $(i, j, k)$  corresponding to the discretized spatial coordinates  $(x_i, y_j, z_k)$  and the origin is a point on this lattice. The cell's side in each direction is one spatial step. One can see that each component of the magnetic field is surrounded by the components of electric field that correspond to the curl operator. Similarly placing more Yee's cells next to each other results in electric field components surrounded by appropriate magnetic field. Each component of EM field is shifted by half a step in particular directions to accommodate the curl equations. As noted above, it is straightforward to show that the discretization of equations (28) using the grid based on Yee's cell leads to the fact that interface conditions are explicitly included in simulations. One would only need to properly discretize the dielectric function. We note that equivalently to the arrangement of EM field components in figure 10 we can interchange the electric and magnetic fields sublattices, a procedure frequently used in [288]. In our calculations (and the accompanying codes) we employ the arrangement shown in figure 10 as introduced by Sadiku [289] and Sullivan [290]. Once the curl equations are discretized in space one needs to propagate these equations along a discretized time axis. This is frequently done using the leapfrog-time stepping technique, which first evaluates the magnetic field using Faraday's law and then based on the updated magnetic field the electric field is advanced in time. It should be noted that the opposite scheme, in which electric field is updated first, is equivalent to the conventional time propagation procedure. Since this approach is essentially an initial boundary value problem, knowledge of the EM fields

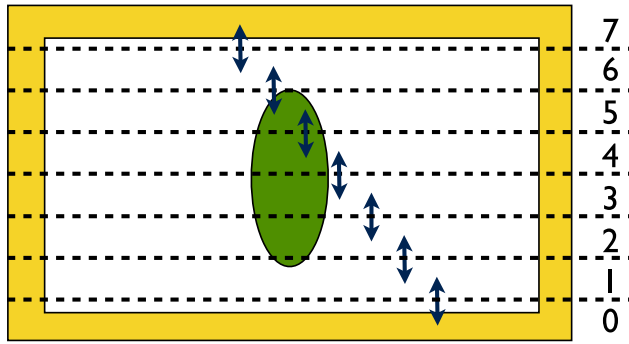


**Figure 11.** Schematics of parallelization of FDTD. Absorbing boundaries are shown as a yellow layer surrounding the grid. Dashed lines indicate the boundaries between processors. Vertical arrows indicate send/receive operations needed to calculate spatial derivatives at the boundaries.

at time  $t = 0$  is required. Once the grid is initiated, i.e. an incident source begins to radiate, the field updates in time are done for all spatial positions on a grid. The most common practice in computational nano-optics is to use pulsed sources implementing either its so-called soft analogue or more commonly utilized the total field/scattered field approach [288]. The latter uses the linear property of Maxwell's equations and splits the computation domain into two regions: (a) total field region surrounding a nano-system, where both scattered and incident fields are evaluated, (b) scattered region surrounding total field region, where only scattered fields are calculated. For systems with periodic boundaries, if one is interested only in a normal incidence geometry, a soft pulsed source can be easily implemented as shown in all periodic codes accompanying this review.

In one or two dimensions FDTD is relatively fast and does not necessarily require much of the computer memory. In contrast, 3D simulations are quite costly in terms of time and memory usage. However, owing to the finite differences discretization in FDTD one can utilize multiple processors. The supplied codes are written using the message-passing interface, which is widely implemented in, for example, the freely available Rocks Cluster package. The idea of parallel evaluation of 2D FDTD equations is schematically depicted in figure 11. Here a total number of processors used is eight, each of which has its own unique number called *rank* that starts with 0 for the root processor. One can decompose FDTD grid onto eight slices along  $x$ -axis as shown in the figure 11, or vertically along  $y$ -axis—either decomposition leads to nearly identical speedup factors as long as  $x$  and  $y$  dimensions are the same. Clearly if a given problem requires elongated geometry the best way to choose a parallel grid is to slice the FDTD domain along shorter direction. The next step is to implement send and receive operations allowing neighbor processors to exchange data as schematically shown in figure 11.

When simulating EM wave propagation in open systems, the spatial grid must be terminated with particular boundary conditions ensuring that outgoing waves leaving the system do not artificially come back. A simple termination of the grid is equivalent to replacing boundaries of the simulation domain with perfect electric conductor. In this case the EM

radiation never leaves the system and results in unphysical field-matter interaction. Unlike in numerical integration of the Schrödinger equation where one propagates a wavepacket and can easily absorb outgoing probability density flux via the exponential window function or the optical potential method [291], absorbing boundary conditions for the Maxwell equations are more involved since the latter corresponds to the vector field and absorption must be taken care of at all possible scattering angles. A widely used approach is to surround the simulation domain by a set of unphysical material referred to as perfectly matched layers (PMLs), the transmission and reflection of which are adjusted such that the incoming wave enters PMLs with the minimum reflection and maximum transmission and then attenuated inside PMLs. The cornerstone of this approach is related to different types of PML coefficients for different EM field components such that to minimize the reflection and maximize the transmission at all angles. The original idea, proposed by Bérenger [292], was to split each component of EM field into two sub-components corresponding to two contributions from the curl operator and then apply PMLs separately for each sub-component. Since the original paper [293], several extensions to PML method were proposed. Of these, the easiest to implement but yet very powerful is the so-called convolution PML (CPML) technique [294]. It has a very important advantage over the split-component method: it efficiently absorbs evanescent fields without causing numerical instabilities—obviously a highly desirable feature in numerical plasmonics. Our codes are supplied with CPML absorbing boundaries. The particular CPML coefficients seen in the codes were carefully determined in numerous numerical experiments [288] and extensively tested on the plasmonic and exciton-plasmon systems considered here.

An important technical point should be noted: The numerical stability of the FDTD propagation requires that the Courant condition [288]

$$\delta t < \frac{\delta x}{\sqrt{N}c}, \quad (44)$$

is satisfied, where  $\delta t$  and  $\delta x$  are the integration time step and the spatial resolution employed in the calculation,  $N$  is the number of dimensions in the given problem and  $c$  is the speed of light in vacuum. In all our codes the expression  $\delta t = \delta x / (2c)$  is used to ensure numerical convergence irrespective of a number of dimensions involved.

Finally, the model dielectric functions for dispersive materials are given by equations (1)–(4) as functions of frequency. The FDTD solver requires the presentation of these functions in the time domain. The commonly used approach relies on properly defining new (auxiliary) equations capturing the dynamical behavior of the polarization current density (so-called the auxiliary differential equation method (ADE) [295]) in spatial regions with the dispersion. To illustrate this method we consider the most general example of a material whose optical properties are described by the Drude-Lorentz function (2). The corresponding equations on the current density can be obtained from the relation between polarization, displacement, and electric field in the frequency domain

$$\mathbf{D} = \varepsilon_0 \varepsilon_\infty \mathbf{E} + \mathbf{P} = \varepsilon_0 (\varepsilon_\infty + \chi(\omega)) \mathbf{E}, \quad (45)$$

where the electric susceptibility is defined as  $\chi = \frac{\varepsilon}{\varepsilon_0} - 1$ . The contribution to the displacement current from the dispersive second term in (45) reads

$$\begin{aligned} \mathbf{J}_D &= i\omega \varepsilon_0 \left( -\frac{\Omega_p^2}{\omega^2 - i\Gamma\omega} \right) \mathbf{E}, \\ \mathbf{J}_L^{(n)} &= i\omega \varepsilon_0 \left( \frac{\Delta \varepsilon_n \omega_n^2}{\omega_n^2 + i\gamma_n \omega - \omega^2} \right) \mathbf{E}, \end{aligned} \quad (46)$$

here the current density is split in two parts, i.e.  $\mathbf{J}_D$  is the Drude current density and  $\mathbf{J}_L^{(n)}$  is the Lorentz current density associated with  $n$ th pole in (2). Finally, the corresponding auxiliary differential equations on the current densities in the time domain are [296]

$$\begin{aligned} \frac{\partial \mathbf{J}_D}{\partial t} + \Gamma \mathbf{J}_D &= \varepsilon_0 \Omega_p^2 \mathbf{E}, \\ \frac{\partial^2 \mathbf{J}_L^{(n)}}{\partial t^2} + \gamma_n \frac{\partial \mathbf{J}_L^{(n)}}{\partial t} + \omega_n^2 \mathbf{J}_L^{(n)} &= \varepsilon_0 \Delta \varepsilon_n \omega_n^2 \frac{\partial \mathbf{E}}{\partial t}. \end{aligned} \quad (47)$$

Equations (47) are then discretized in time and are propagated along with the Maxwell equations in spatial regions occupied by the dispersive material.

This relatively simple and yet powerful FDTD technique and its extensions has attracted considerable attention, resulting in several commercial packages, yet it is important to emphasize that the availability of home-built codes is often crucial. Although commercial packages offer a wide variety of options including automatic parallelization, they lack the versatility needed for advance research, including many important features as discussed below. Despite the wide variety of commercial products, a cutting-edge research depends critically on capabilities that reach far beyond those of black-box commercial codes—for example, integrating Maxwell’s equations on a grid with additional propagations of the Liouville–von Neumann equation, which is not included in any commercial packages. In passing, it should be mentioned that several research teams have recently begun to use simulations on graphical cards—graphical processor unit (GPU) FDTD [288]. Although GPU simulations can be very efficient compared to standard symmetric multi-processor (SMP) clusters, there is a fundamental limitation to speedups one can achieve using GPU. For example, to be able to perform simulations similar to some of those presented below one needs to use a graphical card with a memory larger than 32 Gb, which is not commercially available yet. In order to perform such simulations it is required to access RAM memory on a motherboard, which dramatically slows simulations and results in speedup factors of less than 1, i.e. computations are actually slower on several GPUs compared to a single processor.

### 3.2. Numerical integration of coupled Maxwell–Bloch equations

We now turn to the discussion of exciton-plasmon materials and numerical implementation of a Maxwell–Bloch integrator. The original idea of numerically integrating coupled Maxwell–Bloch equations was published by Ziolkowski, Arnold, and Godny in 1995 [263]. Consider interaction of

EM radiation with a set of two-level quantum emitters in one dimension. The dynamics of each emitter is governed by the Liouville–von Neumann equation (39) with the local electric field that has contributions from all other emitters and the incident radiation. Each emitter contributes to the total EM field via dipole radiation that is taken into account via corresponding polarization currents. The Maxwell’s equations (28) are coupled to the quantum dynamics of the emitters, and the system of corresponding partial differential equations needs to be propagated in time. In their original paper Ziolkowski *et al* [263] proposed an iterative procedure based on a predictor-corrector scheme to numerically integrate this system of equations. Such a procedure was also adopted in two [265] and three dimensions [269]. One starts iterations with initial conditions corresponding to emitters in the ground electronic state and the incident field is injected into the grid via TF/SF or by other means [297]. The solution vector,  $\mathbf{U}$ , that contains all components of the EM field and the density matrix elements for each emitter, is updated according to

$$\mathbf{U}^{(\text{new})} = \mathbf{U}^{(\text{old})} + \delta t \mathbf{F} \left( \mathbf{U}^{(\text{old})}, \mathbf{U}^{(\text{new})} \right), \quad (48)$$

where  $\mathbf{F}$  is the functional based on Maxwell–Liouville–von Neumann equations. It was shown that the proposed scheme converges after about 3–4 iterations for each time step. The convergence, however, is significantly diminished at high emitters’ concentrations. It also becomes noticeably slower when applied to exciton-plasmon systems at resonant conditions [269] when emitter’s transition energy is close to an SPP mode of the plasmonic system.

Bidégaray proposed an alternative numerical scheme similar to the ADE method that is used to numerically describe the optics of dispersive materials [298]. The premise is to split Maxwell’s equations from the quantum dynamics by a half a time step. The resulting numerical procedure as outlined below does not require several iterations for each time step (which may become very costly when attempting to obtain steady-state solutions). The method is called a weakly coupled technique and was proven to be very efficient especially in two and three dimensions. The resulting integration procedure of the coupled Maxwell–Bloch equations can be outlined as follows:

1. In the regions occupied by quantum media Maxwell’s equations are solved utilizing FDTD algorithm. First, the magnetic field is updated according to Faraday’s law. Next, using Ampere’s law we update the electric field with the macroscopic polarization current density, which uses the density matrix at the previous time step. The EM field in the regions occupied by metal is updated according to the ADE method evaluated at the same time step as the density matrix components. With the knowledge of electric field components (stored in memory at two time steps) we update the density matrix at each spatial point on the grid according to (39) using a suitable numerical technique for the integration of a system of ordinary differential equations. Usually the fourth order Runge–Kutta scheme is sufficient.



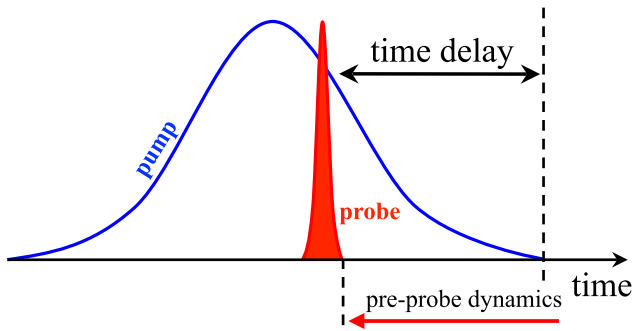


**Figure 12.** Illustration of the pump-probe simulations.

2. With the knowledge of the electric field components and updated density matrix, we calculate the macroscopic polarization current at each grid point.

Clearly the weakly coupled method is not limited to a particular equation used to describe the quantum dynamics. One can use this method and couple Maxwell's equations to a set of rate equations (42), for instance.

### 3.3. Notes on linear and nonlinear simulations

The FDTD algorithm is a time domain method that requires extra-effort when calculating steady-state solutions of the Maxwell equations or a particular spectral response such as a scattering cross-section. In the linear regime, when optical properties of the system under consideration are independent from the incident field, it is possible to obtain a spectral response within a single FDTD run. The method, referred to as the short pulse method (SPM) was first introduced in [299]. The system is excited by a short pulse of the bandwidth that covers the spectral range of interest. The corresponding equations are propagated for extended period of time such that the EM fields decay due to intrinsic losses in the system and radiation to the far field. During the time iterations the discrete Fourier transform of EM field components is evaluated on-the-fly. After reaching the end of the time propagation the calculated Fourier components are weighted with respect to the incident pulse contributions at a given frequency (that includes both an amplitude and a phase). This method thus yields spectra in the frequency domain within a single FDTD run.

Because the SPM relies on matching Fourier-frequency components of the output signal with the corresponding components of the incoming pulse, this method cannot be used for processes involving inelastic scattering or nonlinear response. A common example of the former type is the response of a molecular system exhibiting scattering or fluorescence at frequencies different from the absorption peak. Here the conventional continuous wave method (CWM) must be applied. One drives the system using CW pump at a given frequency  $\omega_{in}$ , steady-state solutions are obtained, a given observable is calculated, and the process is repeated for another  $\omega_{in}$  (more on this subject below).

Let us now consider an example of nonlinear spectroscopy where materials are subject to a high intense fs laser pulse pump. After some controllable time delay the low intense

probe is applied, measuring a particular spectral observable such as reflection or transmission, for instance. The goal of this technique is to be able to track the dynamics of a system driven by the pump recording changes of the observable compared to a linear case (i.e. when the pump is not applied).

The key challenge in modeling nonlinear dynamics using the pump-probe pulse sequence is to disentangle signals caused by the strong pump and the weak probe. When a system comprised of optically coupled emitters is excited by intense pump pulse, it exhibits polarization oscillations lasting long after the pump is gone. Consequently, when the system is probed by a weak probe, one observes an undesired high intensity signal at the pump frequency caused by induced polarization oscillations. Experimentally, such oscillations may be filtered out so as not to interfere with the probe in the far field. In simulations, these unwanted oscillations must be handled carefully because they may interfere with the signal produced by the probe. An efficient computational method to simulate transient spectroscopy experiments was proposed in [300]. The idea behind this method is illustrated in figure 12. A high intensity pump drives the system, then a weak probe is sent after a given time delay. The corresponding equations of motion are propagated in time and space with the driving pump up until the probe pulse 'arrives'. At that time the density matrix elements are recorded at all grid points where quantum emitters are located. These data are used as initial conditions for simulation of the probe interaction with the sample. This method guarantees that undesired high amplitude oscillations are absent when one probes the system and that the probe does not alter the optical response of the system. The method is however approximate as it disregards pump-probe coherences that may affect the actual experimental system.

To illustrate how such a technique works we consider a pump-probe experiment applied to a thin 1D layer comprising interacting two-level molecules with molecular resonance at 1.6 eV. Our interest is to apply a pump-probe pulse sequence and evaluate the absorption as a function of the incident photon frequency and the pump-probe delay for different pump intensities. Figure 13 shows results of simulations based on the numerical technique described above. The time envelope of the pump pulse is taken in the form [282]

$$\int_{-\infty}^{+\infty} F(t) dt = n\pi \frac{\hbar}{2\mu_{12}E_0}, \quad (49)$$

where  $n = 1, 2, 3, \dots$  and  $E_0$  is the pump amplitude. We start with a pump corresponding to the  $\pi$  pulse ( $n = 1$ ) that completely inverts a single molecule, transferring population initially located in the ground state to the excited state. It is seen that the system exhibits positive absorption during the first half of the pump (even slightly longer than 90 fs) and then the sign of the absorption changes as molecules are in their excited state. The probe pulse triggers stimulated emission thus resulting in a negative absorption. Other panels in figure 13 demonstrate the results for the pumps with  $2\pi$ ,  $3\pi$ , and  $4\pi$  envelopes. As anticipated, the molecules undergo Rabi oscillations that depend on the pump pulse area. However, the Rabi cycling is not perfect as it would be if the molecules were

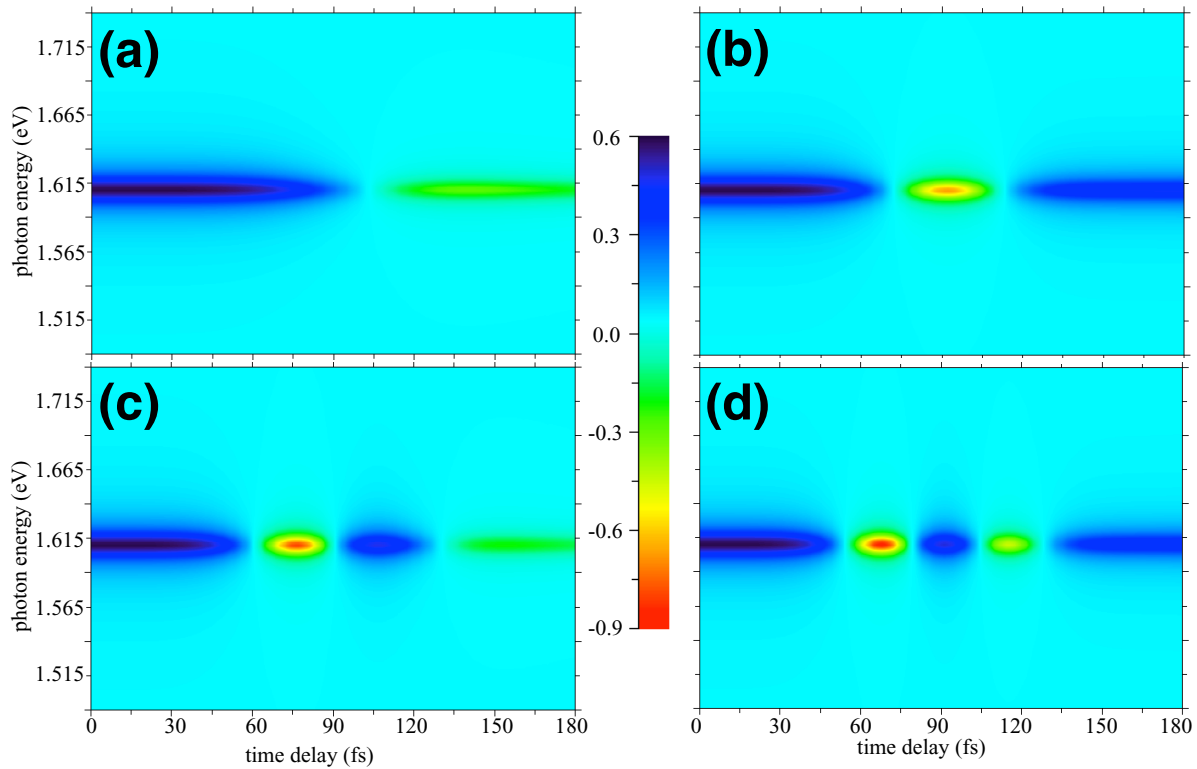


**Figure 13.** Absorption in the pump-probe simulations as a function of the incident photon energy and time delay. Panels (a) through (d) show how absorption changes with time when  $\pi$  (a),  $2\pi$  (b),  $3\pi$  (c), and  $4\pi$  pumps are applied. The pump is 180 fs long.

independent and not interacting. Each subsequent oscillation of the system from the ground state to the excited state is less pronounced due to decoherence.

### 3.4. Semiclassical treatment of fluorescence

The semiclassical model based on coupled Maxwell–Bloch equations cannot account for the phenomenon of spontaneous emission since the latter is a purely quantum effect associated with the quantum nature of the radiation field. It has been demonstrated that the effect of spontaneous emission can be partially accounted for by imposing a classical stochastic field on the system [266]. Obviously, classical electromagnetic noise cannot mimic vacuum fluctuations; in particular, it can induce excitation of ground-state molecules while vacuum fluctuations can lead only to radiative damping of excited molecules. One can use this trick to study time evolution in a system, which is initially inverted; that is, all molecules are in the excited state. In this case, the induction of emission by the EM noise will soon lead to a dominant signal of induced emission that does not depend much on the nature of that noise, provided the latter is weak enough [270]. This method has been successfully used to simulate superradiance and gain within the FDTD approach [274]. However, this method cannot be used to generate fluorescence in a system of mostly ground-state molecules, where the main effect of such noise will be to induce unphysical molecular excitation (as if a given molecule being embedded in the ‘noise’ field undergoes the unphysical process of absorbing its own spontaneously emitted photon).

It is therefore highly desired to have an algorithm that: (1) still relies on Maxwell’s equations to evaluate spatiotemporal dynamics of electromagnetic radiation; (2) does not include nonphysical excitation of relaxed molecules by ‘their own spontaneous photons’; (3) produces EM field due to spontaneous emission that has a proper time correlation function and dependence on damping parameters (radiationless transition rate, pure dephasing rate). It was recently proposed [301] that this could be accomplished in a straight manner by inserting a dipole source into Ampere’s law with specific time characteristics. Let us briefly overview the method. The idea is that in addition to the classical scattering by the molecule, the molecule itself also acts as a source of spontaneous radiation, which has the properties of a random electromagnetic field. The latter then is added as a dipole source to the Ampere law. The time dependence of the stochastic component of the field can be deduced by considering properties of electromagnetic field produced by a single molecule at the steady state. Upon careful derivation of the corresponding field correlation function, the stochastic field due to spontaneous emission is obtained [301] by employing the stochastic dipole

$$d_{\mathbf{R}}(t) = \sum_{m=1}^N \sqrt{d_m} A_m \cos(\omega_m t + \varphi_m), \quad (50)$$

where  $A_m$  and  $\varphi_m$  are the Gaussian random number and the random phase between 0 and  $2\pi$ , respectively, the sum is taken over  $N$  oscillators ( $N$  needs to be chosen such that the numerical convergence is achieved when a particular physical observable is calculated). The normalization factor  $d_m$  is defined as

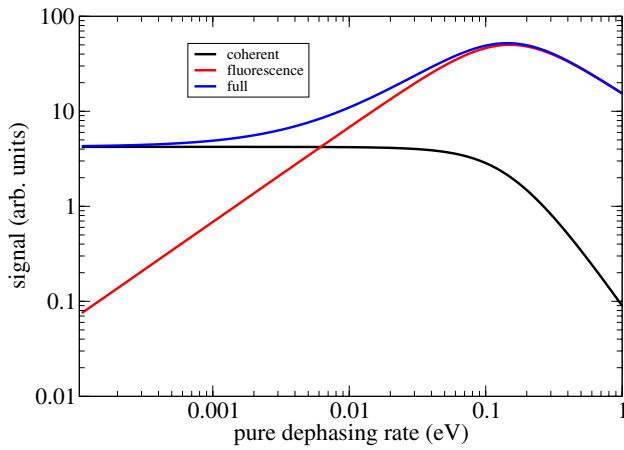


**Figure 14.** Signal as a function of the pure dephasing rate. Black line shows the coherent signal, the fluorescence is shown as a red line, and the complete signal is shown as a blue line.

$$d_m = \frac{(\Delta\omega) c \hbar \Gamma \Gamma_R}{\mu_0 \Omega_{12}^3} \left| \rho_{22} - |\rho_{12}|^2 \right| \frac{N_{\text{total}}}{(\Omega_{12} - \omega_m)^2 + \left(\frac{\Gamma}{2}\right)^2}, \quad (51)$$

where  $\Gamma_R$  is the radiative lifetime of the excited state,  $\Gamma = \Gamma_R + \gamma_{21}$ ,  $\Delta\omega$  is the spectral resolution of the sum in (50) sampled around the molecular transition frequency,  $\Omega_{12}$ , excited state population,  $\rho_{22}$ , and the coherence,  $\rho_{12}$ , are included in (51) to account for the pure dephasing.  $N_{\text{total}}$  is the total number of molecules at given grid point where the stochastic dipole is generated. The dipole (50) is inserted into the Ampere law.

Figure 14 illustrates the aforementioned approach with the example of a single two-level molecule driven by an off-resonant CW radiation. The molecular transition frequency is set at 3 eV and the laser field drives the molecule at 2.85 eV. The intensity of the radiation produced by an oscillating pointwise dipole at steady state is proportional to the square of the dipole moment. The molecule is initially in the ground state and is driven by a low intensity incident field such that the population of the excited state is always small. The corresponding dynamics is evaluated using Bloch equations for the density matrix. With the fluorescence present, the scattering of EM radiation is no longer elastic and for a given CW frequency there is a distribution of scattered frequencies. The total emission/scattering signal is thus evaluated as an integral over all scattered frequencies, however it is informative to separate the signals due to spontaneous emission (50) and coherent radiation produced by off-diagonal elements of the density matrix. Figure 14 shows the linear dependence of the fluorescence on the pure dephasing rate at low dephasing. One can also see that the fluorescence becomes dominant when the dephasing becomes faster, exceeding  $10^{-2}$  eV for the present choice of parameters.

#### 4. Applications

The semiclassical theory described in previous sections inherently takes into account all electromagnetically induced interactions in an exciton-plasmon system, limited only by the

classical description of the electromagnetic field and the mean field approximation for the molecular response. It can thus describe a vast body of various phenomena pertaining to the linear and nonlinear optical response of the many-molecule system interacting with plasmonic nanostructures, including collective effects. This section discusses several intriguing applications of the theory to understand both linear and nonlinear optical properties of exciton-plasmon nanomaterials.

##### 4.1. Dipole induced electromagnetic transparency

Our first example is the problem of reflection/transmission/absorption of low intensity radiation by a 1D layer comprised of interacting two-level molecules. In a series of papers Prasad and Glauber attempted analytically to describe the rich physics of this problem by proposing a new model called polarium [94–97]. The latter consists of interacting randomly oriented two-level emitters. It was shown that the system exhibits a set of multiple resonances near the molecular transition frequency. The reflection was shown to have a flat plateau reaching unity at high molecular concentration. The theoretical analysis, however, relied on a pure mathematical description with a little physical insight.

Later on the semiclassical theory based on Maxwell–Bloch equations was used to re-visit the problem of scattering of EM radiation by thin molecular films [302]. The complete theory in this paper, in addition to the Maxwell–Bloch equations, relied on somewhat artificial term included as a local field correction in Bloch equations, i.e. the so-called Lorentz–Lorenz (LL) correction [262]. Such a term allows one to work out a simple analytical model capable of explaining the observed scattering in a straightforward manner. The LL correction remains however a controversial issue [303]. A simple counterargument is as follows. Focusing on the scattering of EM radiation by a thin molecular film comprised of two-level emitters, it is obvious that at low molecular densities the transmission at normal incidence has a minimum at the molecular transition frequency, which is indeed observed in the Maxwell–Bloch simulation. Let us now assume that we keep increasing the spatial resolution when integrating the corresponding Maxwell–Bloch equations. At relatively low molecular densities the best spatial resolution we can have is such that each grid point is occupied by a single molecule inside the molecular layer. Since we solve Maxwell–Bloch equations exactly all electromagnetically induced interactions are included. Thus we conclude that the LL shift of the resonance exhibited by the transmission should be observed without artificially including the LL local field correction. Indeed, it was shown in [303] by directly including contributions from tens of millions of pointwise dipoles that there is no observed LL shift of the molecular resonance. (It should be noted however that an experimental evidence of the LL shift has been reported [304, 305].)

While the question of a proper microscopic theory that would correctly account for the LL shift remains open, we turn to the discussion of the main results reported in [302, 306]. As noted above, the interpretation advanced in these paper relies on the LL shift. Here we note that numerical simulations

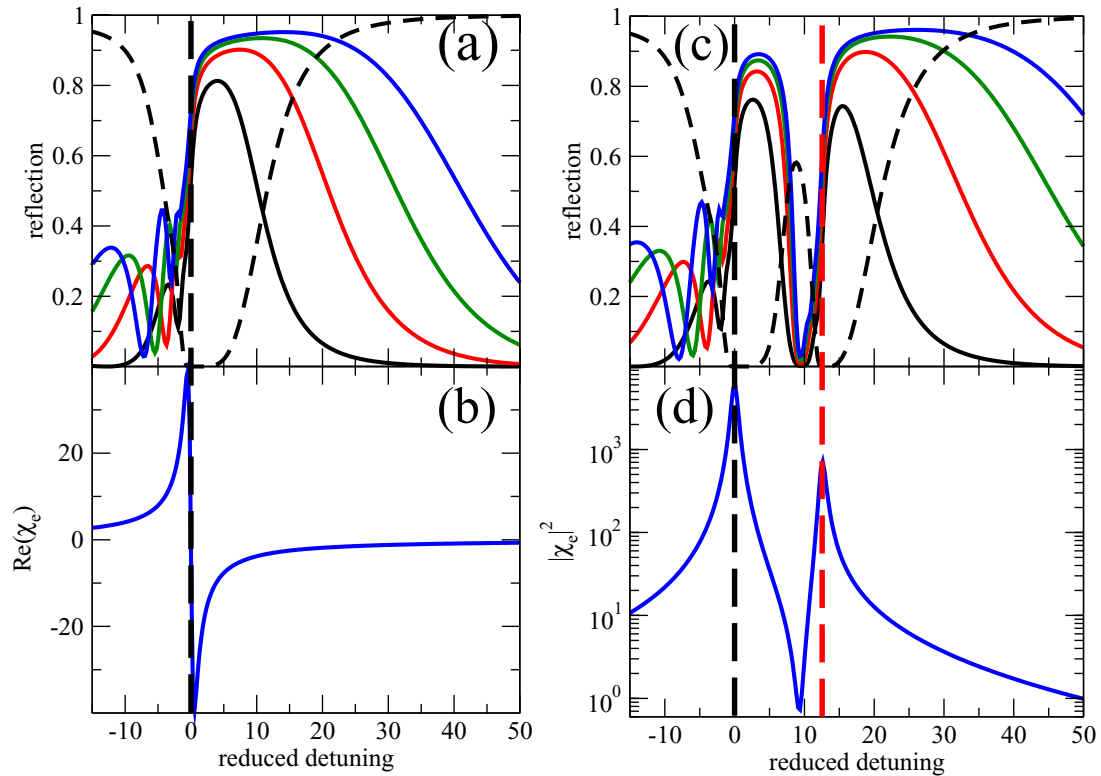


**Figure 15.** Linear optical response of thin molecular films. Panels (a) and (c) show reflection spectra as functions of reduced detuning for films comprised of two-level molecules and three-level molecules, respectively. Corresponding susceptibilities are shown in panels (b) and (d). Vertical dashed lines indicate molecular transition frequencies.

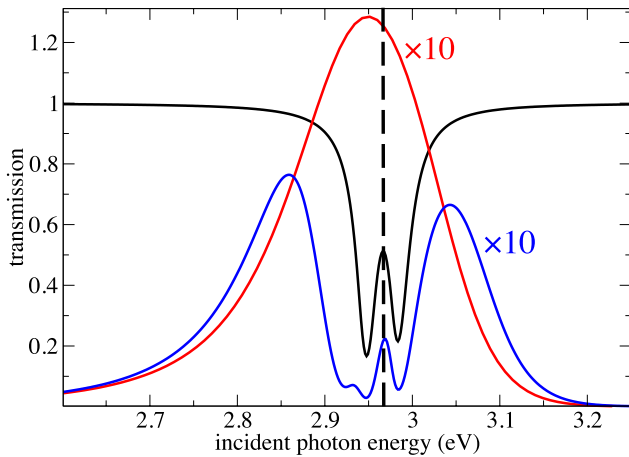
based on direct integration of Maxwell–Bloch equations support the main findings of the [302, 306] without explicitly invoking such shift.

Figure 15 shows results of such simulations of the linear optical properties of thin molecular films. The reduced detuning is defined as  $\delta = \frac{2}{\Gamma}(\omega - \Omega_{12})$ . Panel (a) shows how the reflection spectrum for interacting two-level molecules varies with molecular concentration. The reflection becomes noticeably wider at high concentrations with the maximum shifting towards higher energies (very surprising result as one would expect to see the red shift predicted by the LL model). This is consistent with earlier results reported in [94, 95]. In contrast, the transmission spectra exhibit wide minima, suggesting that the film becomes opaque. An elegant explanation of the obvious plateau exhibited by the reflection at high concentrations was proposed in [302]. We note that the real part of susceptibility is negative in the region of high reflection as seen in figure 15(b), which means that molecules oscillate out-of-phase with respect to the incident field. The medium is then characterized by a collective dipole excitation that cancels out transmission and enhances reflection over a very large window around the transition frequency much like conductive electrons in metal. This behavior dominates at high densities, where the dipoles coherently cooperate to prevent penetration of the incident radiation in the film. Resonant modes observed at a negative detuning are conventional Fabry–Pérot resonances [306].

Completely different physical picture is observed when two-level molecules are replaced by emitters characterized by

a V-type three levels. Figure 15(c) shows reflection spectra for interacting three-level molecules at different concentrations. The widening of the reflection window and blue shift of the resonance is still seen. However, the major difference from the previous example is a clear wide reflection minimum that appears at the energy somewhat between two molecular transitions. The corresponding transmission (not shown) exhibits a maximum exactly at the minimum of the reflection. The system thus displays the transmission window in otherwise nearly completely opaque frequency range. The material parameters such as transition dipoles for two molecular transitions, their frequencies, the thickness of the film, and molecular concentration control the position of the transparency window.

In order to understand the physics behind this phenomenon it is informative to examine the absolute value of the susceptibility as shown in figure 15(d). The susceptibility exhibits two resonances with different profiles. The low energy transition has a simple Lorentzian shape, while the high-energy transition shows up as a clear Fano resonance with a minimum located at the same frequency as the transparency resonance. This suggests that the interference between two dipole transitions plays a key role in this effect. There is a frequency range where two molecular transitions overlap and the corresponding contributions from the two types of dipoles add up in the macroscopic polarization of the medium. In addition, in this frequency range the two dipoles oscillate in opposite directions (out of phase). This comes from the fact that one type of emitters is blue detuned while the other is red detuned, leading to opposite signs of their susceptibilities.



**Figure 16.** 3D DIET in exciton-plasmon systems. Transmission for a stand-alone molecular film is shown as a black like. Transmission for the bare hole array is indicated as a red line. Transmission calculated for the exciton-plasmon system is shown as blue line.

This transparency phenomenon is reminiscent of electromagnetically induced transparency (EIT) [307]. Compared to EIT, however, the strong coupling induced by the pump laser is replaced by strong dipole-dipole interactions. This effect is a linear phenomenon and does not require intense laser radiation. By the analogy to EIT this effect was named Dipole-Induced Electromagnetic Transparency (DIET). DIET results in slow light [306], although the group velocity estimated for interacting  $^{85}\text{Rb}$  atoms reaches as low as 10 m/s, which is relatively high compared to EIT results.

DIET is highly robust to material parameters. We performed 3D simulations specifically for this review in order to illustrate that DIET can be observed in exciton-plasmon systems. The system under consideration is a conventional periodic array of holes in a silver film. The geometrical parameters are: periodicity is 320 nm, film thickness is 200 nm, the hole diameter is 140 nm, and the molecular film thickness is 100 nm. The molecular is placed directly on top of the array at the incident side. The surface plasmon-polariton resonance of the bare hole array is found to be 2.95 eV. The molecular transition energies are set at 2.95 eV (directly at the plasmon mode to achieve strong coupling) and at 2.985 eV. At the molecular number density of  $4 \times 10^{25} \text{ m}^{-3}$  a stand-alone molecular layer exhibits DIET as seen in figure 16 as a maximum in the transmission. The corresponding hybrid system comprised of the periodic array of holes and molecular layer clearly shows very same transmission resonance located inside Rabi splitting. We note that due to strong coupling between the low energy molecular transition and the plasmonic mode there are two expected hybrid states seen in the transmission at 2.86 eV and 3.04 eV.

#### 4.2. Linear optics of excitonic clusters

We now turn to the discussion of linear optical properties of ensembles of interacting molecules in two and three dimensions. Our goal is to establish general physical understanding of how such systems react to external optical excitation. Once equipped with such knowledge we shall discuss how these

properties are altered when molecules are resonantly coupled to plasmonic systems.

As an example that illustrates how excitonic systems scatter electromagnetic radiation we consider an ensemble of two-level molecules uniformly distributed in a subdiffraction volume in the form of a circle (two dimensions) and a sphere (three dimensions) [273]. Such a problem was first considered in a series of works by Prasad and Glauber [94–97], where the framework of polarium model (see section 4.1) was established. It was demonstrated that excitonic clusters might in principle exhibit a set of narrow resonances provided that the pure dephasing rate is negligibly small. Furthermore such resonances are always seen in the background of a wide mode, properties of which are attributed to the collective response of molecules to the incident field. Such a collective mode (Prasad and Glauber referred to this mode as a superradiant one) has unique characteristics that vary significantly with the molecular transition dipole and concentration. We note that such characteristics, which we shall discuss below, were recently experimentally verified [308]. It is also interesting to note that the superradiant mode in excitonic systems is observed only in two- or three-dimensional geometries. Figure 17 shows results obtained for two- (panel (a)) and three-dimensional (panel (b)) clusters with a radius of 20 nm comprised of two-level molecules with a resonant energy of 3 eV. The scattering intensity clearly exhibits two resonances. The first mode is a relatively weak response slightly below the molecular transition frequency. The second is a strong and broad peak at a higher frequency that moves to the blue at larger molecular concentrations. We note that the intensity of the high-frequency mode scales as a square of the molecular density, i.e.  $n_M^2$ , suggesting a possible collective nature of this mode. It should be noted that this collective resonance is noticeably wider than the molecular transition resonance. Moreover, the result for increasing of the transition dipole,  $d_{12}$ , is qualitatively similar to that obtained with increasing molecular density. It is seen that the latter results in a blueshift of the collective mode and in a redshift of the lower-frequency mode [273]. The former shows a quadratic dependence of the resonant frequency on the dipole moment.

It has been shown numerically [97, 273, 309] that the width of the cooperative emission mode and its resonant frequency scale as (SR below stands for superradiant as per [97, 273, 309])

$$\begin{aligned} \Gamma_{\text{SR}} &\sim n_M \Gamma, \\ \omega_{\text{SR}} &\sim n_M d_{12}^2. \end{aligned} \quad (52)$$

The results based on direct numerical integration of Maxwell–Bloch equations follow the same dependence of the superradiant mode seen in figure 17 on the number density and the individual molecular decay rate. It is also informative to explore the spatial dependence of the electromagnetic intensity associated with two observed resonances. Figure 17(d) shows intensity distributions calculated using steady state solutions of Maxwell–Bloch equations at two frequencies. Clearly the electromagnetic intensity at the lower resonant frequency is mainly localized on the surface of the cluster exhibiting a dipole radiation pattern similar to the electromagnetic intensity distributions seen at the plasmon resonance for a single

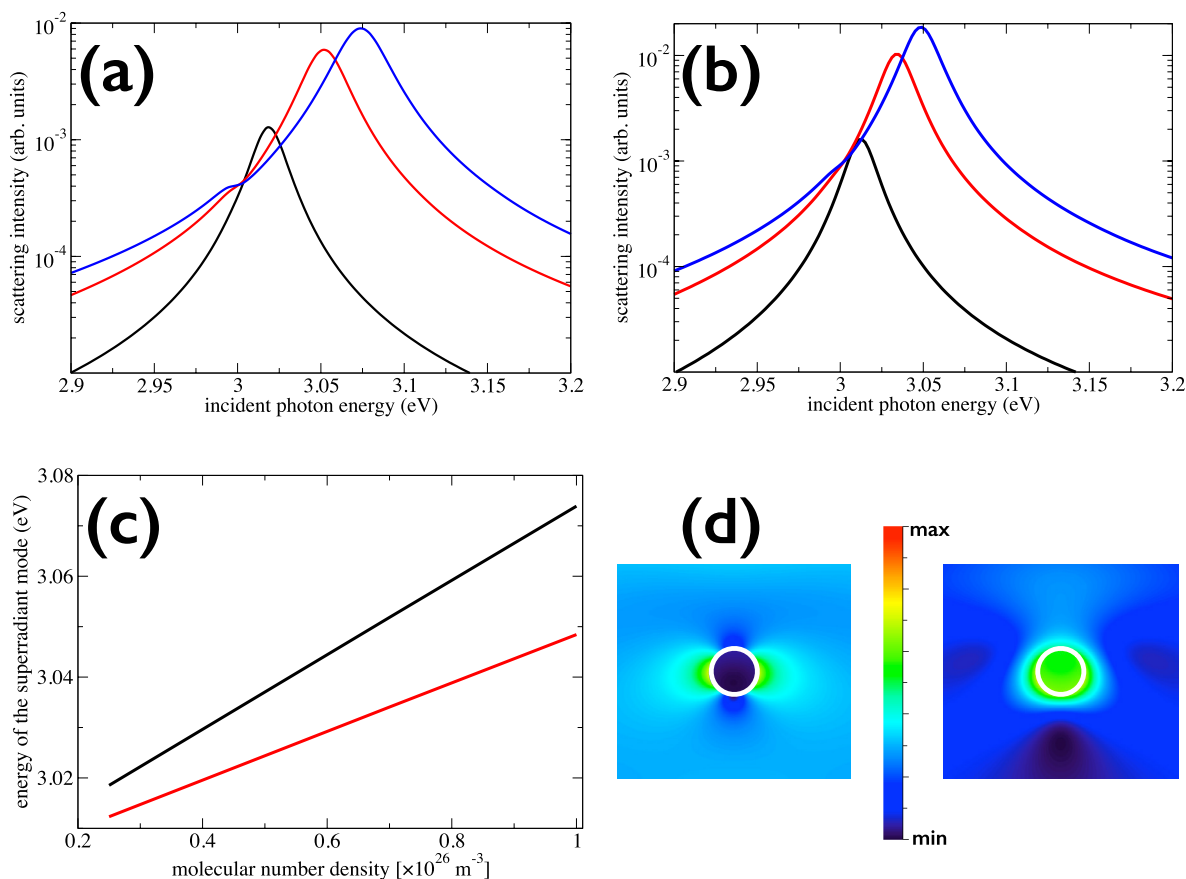


**Figure 17.** Scattering by two- and three-dimensional excitonic clusters. Panels (a) and (b) show scattering intensity as a function of the incident photon energy for 2D (a) and 3D (b) clusters at different densities: black line is for  $2.5 \times 10^{25} \text{ m}^{-3}$ , red line is for  $7 \times 10^{25} \text{ m}^{-3}$ , and blue line is for  $10^{26} \text{ m}^{-3}$ . Panel (c) shows the energy of the superradiant mode for 2D (black line) and 3D (red line) clusters as a function of the molecular density. Panel (d) illustrates intensity distributions for the surface mode (left) calculated at the molecular transition energy 3 eV and the superradiant mode (right) at 3.07 eV.

metal nanoparticle. In contrast, superradiant mode is uniformly distributed over the entire volume of the particle with all molecules coherently participating in the radiation process.

#### 4.3. Collective resonances in hybrid systems

Systems comprised of metallic nanostructured arrays are particularly attractive for interaction with molecular excited states, as the plasmonic resonances may be tuned by geometrical factors (i.e. the periodicity of arrays) to exactly match the molecular frequencies. As was pointed out in previous sections, when the coupling strength between the local field driven by plasmon oscillations and molecules exceeds all damping rates of the system the strong coupling regime is achieved. The strong coupling manifests itself as avoided crossing of the original non-interacting modes. The newly formed polaritons are energetically separated by the Rabi splitting, which reflects the coupling strength. Various experiments and theoretical calculations of a different complexity (ranging from simple two coupled oscillator models [177] coupled to fully quantum calculations [160]) have been performed to describe such a phenomenon. Most of the experiments, however, have been performed at relatively low molecular concentrations, thus not capturing possible collective exciton resonances and their interaction with plasmonic modes.

It was recently demonstrated [273] that core-shell nanoparticles with a metallic core and a molecular shell resonant with the core localized plasmon mode may exhibit not two but three resonances depending on molecular density. The presence of the upper and lower polaritonic modes due to the hybridization of the plasmon mode and individual molecular resonance is, of course, expected. In addition to this observation the third mode seen at relatively high molecular concentrations is also observed in calculations [273, 310]. The physical nature of the third mode is related to the superradiant resonance discussed in the previous section since the mode's width and scattering intensity depend on the density, transition dipole, and shell's thickness similarly to the superradiant mode. Figure 18(a) explores the density dependence of the collective resonance in the system comprised of a silver core and a resonant molecular shell. The Rabi splitting is seen at low concentrations. At higher concentrations the Rabi splitting increases and the third resonance appears near the molecular transition energy. Note that the position of the third mode shifts to higher energies with increasing molecular density as in the case of the superradiant mode seen in figure 17.

A similar collective exciton resonance has been discussed in the context of periodic nanostructured arrays of slits [192], where it was demonstrated that at high molecular concentrations the transmission exhibits a three-peaked structure

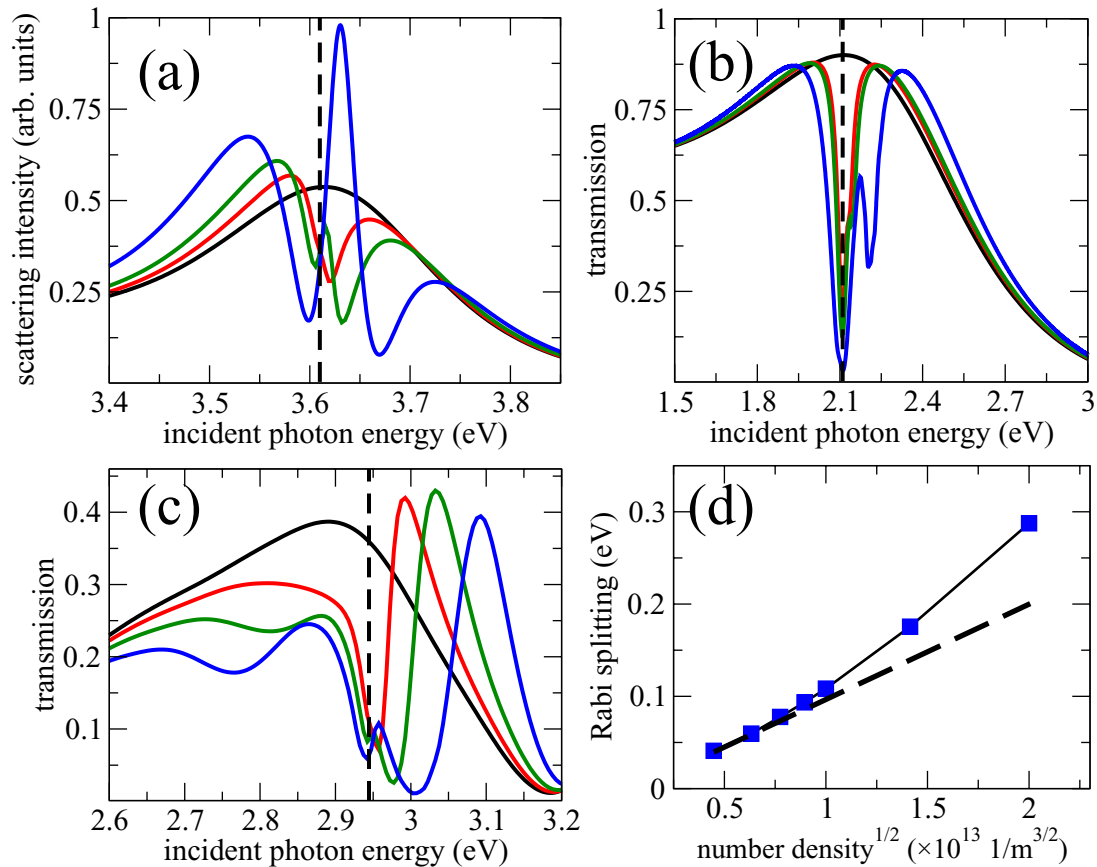


**Figure 18.** Collective exciton resonances in hybrid systems. Panel (a) shows the scattering intensity as a function of the incident photon energy for a core-shell nanoparticle with a silver core of 20 nm in diameter and excitonic 10 nm thick shell. The black line shows the intensity scattered by the bare silver core; the red line represents the scattering by the core-shell particles with the density of molecules of  $8 \times 10^{24} \text{ m}^{-3}$ ; green line is for the density of  $2 \times 10^{25} \text{ m}^{-3}$ ; the blue line is for the density of  $6 \times 10^{25} \text{ m}^{-3}$ . The vertical dashed lines in all panels indicate the molecular transition energy. Panel (b) shows the transmission through the periodic array of slits in a silver film with a period of 300 nm, with a 20 nm thin layer of molecules deposited on top of the film. The black line shows the scattering from the bare slit array; red, green and blue lines are similar results obtained in the presence of molecular films for the molecular densities of  $5 \times 10^{25} \text{ m}^{-3}$ ,  $7 \times 10^{25} \text{ m}^{-3}$  and  $2 \times 10^{26} \text{ m}^{-3}$ , respectively. Panel (c) shows transmission through the hybrid opal array with the period of 320 nm covered by a 20 nm thin layer of resonant molecules. The black line shows the transmission through the bare opal array and the red, green and blue lines are similar signals obtained with molecular layers of densities of  $8 \times 10^{25} \text{ m}^{-3}$ ,  $2 \times 10^{26} \text{ m}^{-3}$  and  $4 \times 10^{26} \text{ m}^{-3}$ , respectively. Panel (d) shows the Rabi splitting for the opal array in (c) as a function of square root of the number density. The deviation from linear dependence (the dashed line) is evident.

similar to the example of the core-shell particle. It was shown that when the in-plane  $k$ -vector varies and the plasmon resonant energy sweeps through the molecular transition, avoided crossing for upper/lower polaritonic branches is observed. When the molecular density is high the third mode appearing in the transmission spectra is nearly dispersionless suggesting that indeed the third resonance is of collective nature mediated by the strong molecule-molecule interactions. The appearance of the collective mode in periodic systems leads to a large repulsion of the upper polariton and in some cases to enhanced transmission at specific frequencies. To provide a clear test of the collective nature of the third mode, calculations with molecule-molecule interaction artificially turned off were performed in [192]. No other changes were introduced meaning that plasmon-molecule coupling was still presented. Technically this was accomplished by replacing the molecular layer with a single two-level system occupying the same volume as molecular layer in which the local electric was assumed to be spatially uniform, thereby eliminating any

internal dipole coupling, while maintaining all other interactions intact. The dipole-dipole interactions, which arise in the model based on Maxwell-Bloch equations from the field-induced interactions between individual molecules, are therefore absent. It was clearly demonstrated that indeed when molecular dipole-dipole interactions were excluded, the value of the Rabi splitting was smaller and the third mode was not observed. Even at significantly higher molecular densities, when the Rabi splitting exceeded 200 meV, the third peak was absent. Figure 18(b) shows transmission spectra for a periodic array of slits with a 20 nm thin molecular layer placed on the input side of the array. The Rabi splitting increases with increasing concentration and the third resonance is observed near the molecular transition energy. The energy of the collective mode increases with increasing concentration similar to the core-shell system. We note that indications for this mode were found in several early experimental reports [110, 259], but its nature and origin have not been understood at the time.

Recently, experiments were performed on plasmonic opal arrays with J-aggregates deposited on metal surface with the molecular density being a controllable parameter [311]. The idea is to manipulate strong coupling between the Bragg-plasmon mode [312] supported by an opal array and J-aggregates dispersed on the input side of the hybrid structure. The collective exciton resonance was experimentally observed for the first time in these experiments. The transition from conventional strong coupling regime exhibiting the usual upper and lower polaritonic branches to a more complex regime was clearly demonstrated. The third nondispersive mode was seen in reflection spectra, as the concentration of J-aggregates was increased. Rigorous numerical simulations based on 3D coupled Maxwell-rate equations qualitatively support these experimental results. Figure 18(c) shows transmission spectra for the opal array at different molecular concentrations. One can see the appearance of the collective resonance reminiscent of the third mode discussed for other geometries. Furthermore it is clear from figure 18(d) that the Rabi splitting deviates from the conventional  $\sqrt{n_M}$  dependence at high densities when the collective mode is seen in spectra.

A simple semiclassical analytical model explaining the physical features of the collective mode was proposed [311]. Let us consider  $N$  identical molecules interacting with one another and with the background surface plasmon-polariton field. The Hamiltonian of such a system reads

$$\hat{H} = \begin{pmatrix} \varepsilon_{12} & C & C & \dots & \Delta \\ C & \varepsilon_{12} & C & \dots & \Delta \\ C & C & \varepsilon_{12} & \dots & \Delta \\ \dots & \dots & \dots & \dots & \dots \\ \Delta & \Delta & \Delta & \dots & \varepsilon_{\text{SPP}} \end{pmatrix}, \quad (53)$$

where  $\varepsilon_{12} = \hbar\Omega_{12}$  is the molecular transition energy,  $\varepsilon_{\text{SPP}}$  is the energy of the corresponding plasmon mode,  $\Delta$  is the molecule-plasmon coupling (deduced from the Rabi splitting), and  $C$  is the phenomenological constant describing the coupling between molecules. This model assumes that molecules are interacting with one another with the same strength. This assumption approximately holds for small enough molecular clusters, and would neglect retardation effects if applied to the systems used in figure 18. Qualitatively, however, the proposed model predicts the correct behavior of the third resonance while if one needs to describe it quantitatively, the numerical integration of Maxwell–Bloch equations is required.

The Hamiltonian (53) is easily diagonalized leading to the following set of eigenenergies

$$E_n = \varepsilon_{12} - C, n = 1, \dots, N - 2, \\ E_{N-1, N} = \frac{(N-1)C + \varepsilon_{12} + \varepsilon_{\text{SPP}}}{2} \pm \sqrt{((N-1)C + \varepsilon_{12} - \varepsilon_{\text{SPP}})^2 + 4N\Delta^2}, \quad (54)$$

here the first root is  $(N - 2)$ -degenerate and the other two represent the upper and lower polaritonic branches although noticeably altered by molecule-molecule interactions. The Rabi splitting,  $\Delta E$ , defined as the energy difference between these upper and lower polaritonic branches at the zero-detuning condition ( $\varepsilon_{12} = \varepsilon_{\text{SPP}}$ ) is

$$\Delta E = \sqrt{(N - 1)^2 C^2 + 4N\Delta^2}. \quad (55)$$

At low molecular concentrations, as the molecule-molecule interaction energy  $C$  is negligible, the Rabi splitting scales as  $\sqrt{N}$  as in the conventional model [108]. Moreover, the scaling of the Rabi splitting with respect to the molecular transition dipole is linear since the molecule-plasmon coupling constant  $\Delta$  also scales linearly with the dipole. This model thus mimics the conventional model based on two coupled oscillators as a limiting case. Let us now examine the behavior of the Rabi splitting at high molecular concentrations. The scaling of the Rabi splitting with molecular density at high  $N$  is

$$\Delta E \approx NC. \quad (56)$$

The clear deviation of the Rabi splitting from the expected  $\sqrt{N}$ -dependence is observed. This has also been observed in numerical simulations performed for all systems discussed in figure 18.

It is of interest to determine how the coupling constant  $C$  scales with molecular parameters. This can be done by fitting the results (54)–(56) to those obtained by numerical simulations, and such fitting was done by simulating systems with varying molecular transition dipole moment,  $d_{12}$ , and molecular density at the resonant conditions corresponding to opal arrays, arrays of slits, and periodic arrays of holes (for both rectangular and honey-comb arrangements of holes). From all these simulations a nearly ideal quadratic dependence of the coupling  $C$  on the dipole moment was observed. Moreover, a clear linear scaling with the molecular density at intermediate densities was also seen. Using a simple argument for the mean inter-particle distance scaling with the number density  $\langle R \rangle \sim 1/N^{1/3}$ , we arrive at the following expression for the coupling constant  $C$

$$C \sim Nd_{12}^2 \sim \frac{d_{12}^2}{\langle R \rangle^3}. \quad (57)$$

The coupling constant evidently has the form of the potential energy of a dipole in the field of another identical dipole thus confirming earlier prediction [192] that the observed third mode corresponds to the collective exciton resonance. We note that the scaling of the collective mode with molecular concentration and the dipole moment is the same as in (52). Moreover this expression combined with (56) results in a clear quadratic dependence of the Rabi splitting on the molecular density. This model is independent from the geometry suggesting that the results discussed here should be observed in other hybrid systems.

We note that the collective mode discussed in this section does not require a presence of the plasmon field. All attributes of the collective nature of this mode pointed out above such as quadratic dependence on the transition dipole were found in excitonic clusters as well [273]. One can argue that for a given molecular concentration higher exciton-plasmon coupling (i.e. higher values of the Rabi splitting) may in principle lead to an observation of the collective mode as long as the damping at the molecular transition energy is lower than the strength of molecule-molecule interaction.



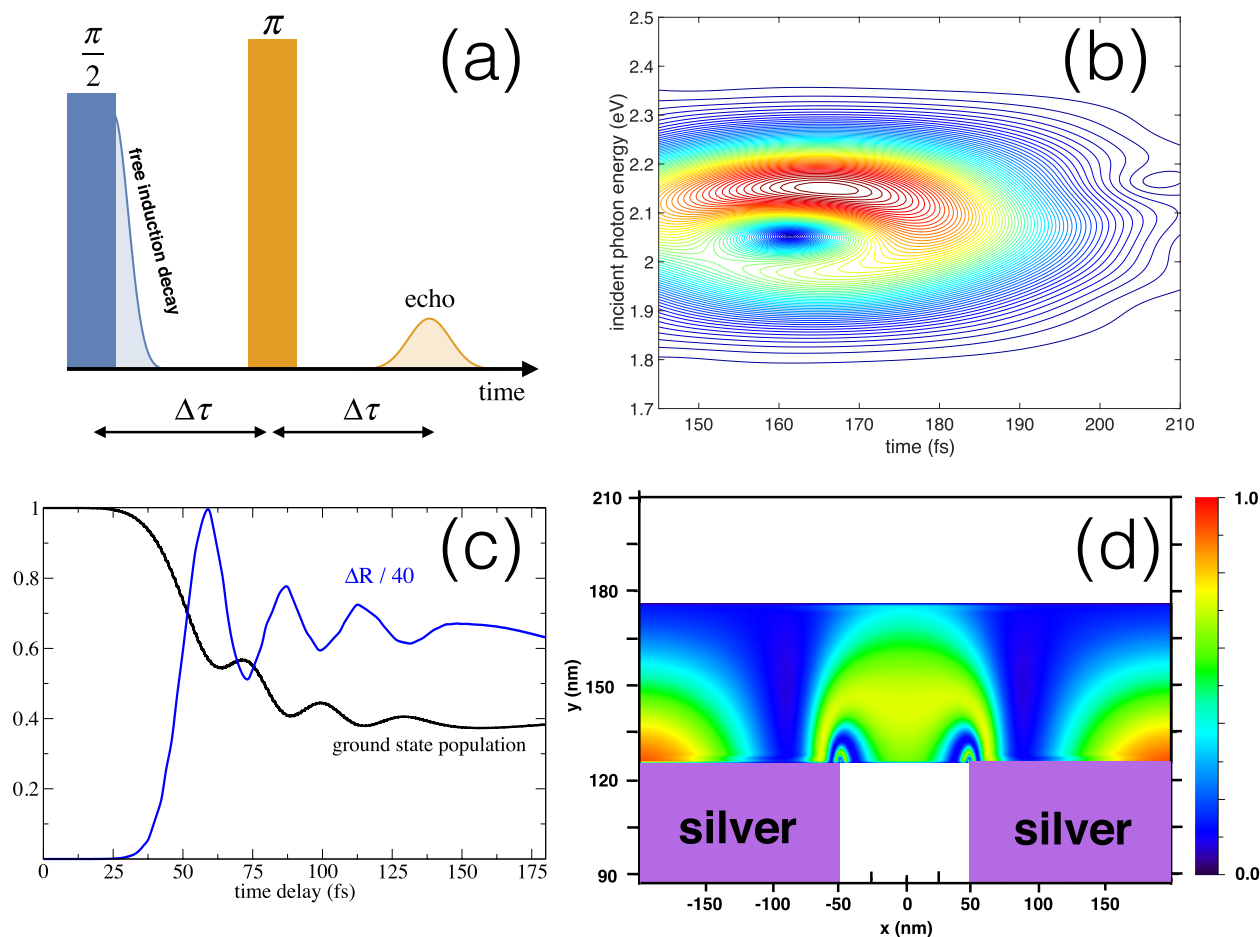


**Figure 19.** Panel (a) schematically shows the dynamics of the two-pulse photon echo spectroscopy. Panel (b) shows the Husimi transform of the time signal of photon echo detected on the output side of the periodic slit array covered by a 20 nm thin resonant molecular layer. Panel (c) shows the ensemble average ground state population of molecules (black line) and the change in reflection (blue line) as functions of the time delay between the pump and the probe pulses. Panel (d) shows the instantaneous spatial distribution of the ground state population of molecules inside molecular layer placed on top of the slit array during strong laser pulse excitation.

#### 4.4. Nonlinear molecular plasmonics

The presented semiclassical theory can also be applied to describe nonlinear optical phenomena since the molecular part of the theory has no restriction on how high the local electric field amplitude may be. We end this review by providing several representative examples of hybrid systems exposed to strong external laser radiation.

The way the pure dephasing is introduced in the theory is through simple damping terms in corresponding equations governing quantum dynamics. This corresponds to homogeneous broadening that implies irrecoverable loss of phase. It is also interesting to include inhomogeneous broadening in hybrid systems explicitly in order to investigate possible phase revivals, which can be harvested by photon echo spectroscopy methods [313]. To this end we consider a molecular aggregate characterized by a distribution of level spacings having a central transition energy. Each molecule is detuned from this central energy by some amount due to inhomogeneous broadening, which can result from conditions such as Doppler shift in individual gas molecules or variations in electric field from point to point in solids. Given such a distribution of molecular transition energies, each individual molecule oscillates at

a frequency that is slightly different from the others after the system is pumped by a strong incident pulse. As a result, all of the molecules begin to oscillate in phase at first, but eventually they dephase within a characteristic inhomogeneous lifetime and, if left alone, never re-phase again resulting in free induction decay [282]. However, for times less than the natural lifetime of the molecule, each molecule is still oscillating. These oscillations are lost when including pure dephasing as a simple damping. One can in principle invert the dephasing process by applying a second pump in the form of a  $\pi$ -pulse. The oscillations then all run in reverse, resulting in a subsequent rephasing. The ensemble of molecules exhibits a non-zero macroscopic polarization once again eventually emitting radiation known as a photon echo signal as schematically illustrated in figure 19(a). This technique is widely used in chemistry and is referred to as photon echo spectroscopy [314]. Inhomogeneous effects due to variations in molecules' surroundings cause each molecule to oscillate at a slightly different frequency than the others, and photon echo spectroscopy removes this effect. Any remaining dephasing cannot be reversed by the echo technique, and is revealed as diminished intensity of the echo [315]. For example, as the delay in applying the  $\pi$ -pulse increases, the natural lifetime of the emitters causes the amplitudes of their

oscillations to decrease, resulting in an echo with lower intensity. Thus a time and frequency structure of a detected photon echo contains important information about the probed system. Additionally, the recovery of a time signal after dephasing offers prospects for memory storage. In [316], the optical properties are copied to a spin system whose lifetime is much longer than that of the optical system thus extending the duration of the system's memory.

Recently [317] the two-pulse photon echo spectroscopy was applied to hybrid systems. The semiclassical theory is expanded to include inhomogeneous broadening of molecules explicitly. When molecules placed in a close proximity to plasmonic structures (such as periodic arrays of slits or nanoparticles) and are resonant to a plasmonic mode a double-peaked time signal of photon echo is observed. The corresponding Husimi transformation (time-frequency map of a time signal [318]) is shown in figure 19(b). One can see that the time-frequency map exhibits two frequencies between 140 and 190 fs. Upon careful examination it was found that such two frequencies presented in the photon echo signals correspond to hybrid states of the system, i.e. upper and lower polaritons. It is interesting to note that in all numerical experiments performed in [317] the frequency of the upper polariton was always dominant in echo spectra as seen in the Husimi transformation of the time signal in figure 19(b). It was also shown that the unique signature of upper and lower polaritons in photon echoes was highly sensitive to exciton-plasmon coupling making it a great tool for ultrafast optical probes of nanomaterials to further scrutinize fundamentals of light-matter interaction at the nanoscale.

The resonant pump-probe nonlinear spectroscopy applied to hybrid nanomaterials can reveal interesting features of the electromagnetic energy exchange between plasmons and excitons [199, 283]. We apply the numerical procedure outlined in section 3 to obtain time resolved spectra modified by a strong optical pump driving the hybrid system comprised of the periodic array of slits in a silver film covered by a 10 nm thin layer of resonant molecules. The pump pulse is 180 fs long and with the amplitude high enough to drive a single molecule through several Rabi cycles. The reflection is calculated at the upper polariton frequency as a function of the pump-probe delay. The change of the reflection with respect to its unperturbed value is shown in figure 19(c) along with the ensemble average population of the molecular ground state. There is a clear correspondence between the oscillations of the ground state population and the changes in reflection induced by the pump. (A similar correlation was found for changes in transmission.) The observed oscillations in the transient spectra are due to quantum transitions between ground and excited states in individual molecules. It is also important to examine the role of dephasing in hybrid materials. This property is greatly affected by the inhomogeneous electric field due to SPPs, as is evident from figure 19(c). One of the causes of the fast decay of Rabi oscillations (in addition to pure decoherence and relaxation caused by interaction with the metallic system, which is explicitly included in the model) is spatially dependent excitation of the molecular layer, resulting from the strong gradient of the electric field induced mainly by surface

plasmons. Different parts of the molecular ensemble therefore experience different local fields. This effect in turn changes the plasmon dynamics, influencing not only the amplitude of Rabi oscillations but also the Rabi period. It should be noted that the molecular layer influences the near-field via the polarization current, which results in even faster dephasing. Simulations with a thicker molecular layer confirm the aforementioned conclusion, i.e. the Rabi oscillations decay significantly faster when a 10 nm thick molecular layer is replaced by a layer with a thickness of 50 nm [199].

It is informative to examine how molecules undergo Rabi cycling under the influence of a strong pump at different spatial locations near metal interface. As pointed out above, strong electromagnetic field gradients result in a highly inhomogeneous excitation of molecules. This is demonstrated in figure 19(d) where we plot a snap-shot of the spatial map of molecules in the ground state taken at the time corresponding to the maximum of the pump. A clear strong spatial variation of the ground-state population is seen. In fact, the variations of the ground state population are oscillations whose wavelength varies somewhat over the region of molecules. One might surmise that the wavelength of these oscillations is on the order of that of the pump, but it is actually significantly smaller. The retardation effects are revealed to be the cause of the spatial modulations of the ground-state population: the temporal oscillations of the ground state probability are similar between adjacent spatial points, but slightly shifted [319]. Hence at a given time, adjacent points have slightly different values of ground state probability. For larger pump amplitude, each molecule will undergo Rabi flopping more rapidly in time. Thus a given phase shift between adjacent locations will lead to a larger shift in the ground state population between those two locations. For a slower group velocity, the pump takes longer to reach an adjacent point, causing the temporal oscillations between two adjacent points to acquire a larger phase difference. The very reason for such spatial variations in the ground state population is the strong coupling between molecules and the corresponding plasmon mode resulting in a small group velocity.

## 5. Summary and outlook

Exciton-plasmon interaction and the laboratory observation of its consequences have attracted much attention in recent years. In this account we have briefly reviewed the main observations in which this coupling is expressed, described models for its description and presented the state of the art methodology for numerical simulations of its manifestations in key experimental observations. At the same time, we have emphasized the common origin of many of the observed phenomena and similar observations in other settings. This common origin is exemplified by the typical characteristics of 'strong coupling' phenomena, whose manifestations as an avoided crossing between free exciton and free plasmon dispersion lines is qualitatively similar to many other phenomena including plasmon hybridization. Another example is provided by the similarity between exciton-plasmon coupling and coupling of

molecular excitations to electromagnetic cavity modes. While these similarities are evident, it is important to keep in mind important practical differences. Even though avoided crossing is pervasive in many quantum and classical systems, its observation in exciton-plasmon systems is facilitated by the fact that many experimental setups make it possible to control the relevant excitation energy by exploring the frequency-wave-vector dispersion properties. Furthermore, the appearance of strong coupling effects between collective modes of a many-body system is not to be taken for granted and limits to their observation must depend on coherence destroying processes. The study of this balance and its manifestations in different systems is still ahead of us. Also ahead of us, both on the experimental and theoretical-computational fronts, is the exploration of the vast modes of behaviors that may be associated with the nonlinear response of such systems.

The systems involved in these studies are quite complex, and while simple models have been useful for qualitative understanding, their detailed investigations require numerical simulations. We have described the state of the art of these simulations and provided sample codes for interested readers to explore and utilize. In their simplest form, simulations consider the optical response of inhomogeneous dielectric systems, with the most common tool being numerical solvers based on FDTD method to integrate the corresponding Maxwell equations. We have described in detail a more advanced approach based on coupled Liouville-Maxwell equations, where the radiation field and its propagation in the metallic domains of the system are described as before by the Maxwell equations applied to the given inhomogeneous medium in which the molecular oscillating dipoles appear as source currents, while the molecular response is described by Liouville-Bloch equations that account for the quantum evolution of the molecular sub-system under the effects of the local electromagnetic field. This level of description can account for dephasing effects in and nonlinear response of the molecular subsystem, while still provide the versatility needed to treat realistic systems of different sizes and shapes.

Looking back, even in just the last decade the field has made an enormous progress in both experimental and numerical methodologies as well as in the discovery of new modes of behaviors of these interesting systems. Much can be achieved by further studying such systems on this level of sophistication, in particular in exploring their nonlinear response behavior and transient response phenomena. With respect to the latter we note that while avoided crossing of exciton and plasmon dispersion peaks is now often observed in such systems, its temporal counterpart, the observation of Rabi oscillations, has been demonstrating only once. Clearly, a better time resolution and/or better control on the preparation of the initially excited state is needed for such observations, and numerical simulations can play an important role in establishing the needed conditions.

Focusing on the numerical methodology, several directions for needed developments are evident. First and foremost is the classical description of the radiation field. While much can be achieved in a classical description it is obvious that purely classical description cannot account for the often observed system response at radiation wavelengths different

from the incident field<sup>14</sup>. Obviously, a full quantum description of the radiation field is not practical (except in cavities that support one or just a few modes), however some of the relevant quantum consequences can perhaps be accounted for (see equation (19) and the associated discussion).

Another issue that requires further study is the use of the mean field approximation (see equations (30)–(32)) for the molecular response in our numerical modeling. Although numerical results based on this approximation do show coherent response, it is not clear at present how much is lost with respect to the description of coherent response by using this approximation. For example, it is known that excitonic energy transport can change its nature from coherent to diffusive due to thermal and disorder effects. It is certainly of interest to study this transition in the presence of coupling to a plasmonic interface, however it is not evident whether such a study can be done on the mean field level.

Finally, the optical response of metal-molecule interfaces often involves, in addition to collective molecular and metal excitations, also electron transfer between these subsystems. Indeed, the consequence of this type of charge transfer phenomena following optical excitation of such interfaces has become a subject of intense recent studies. The numerical description of such phenomena is obviously beyond the capabilities of the presently available numerical methodologies. It will be interesting to explore the possibility to apply methodologies based on the semiconductor Bloch equations (SBE) [320, 321] for such problems. We note that merging SBE with FDTD has been recently reported for 1D case of a semiconductor quantum well [322]. For recent advances in semiconductor-plasmon materials see [323].

The study of coupled exciton-plasmon systems has come a long way in recent years. With a host of open issues, interesting observations and the promise of technological applications we expect it to remain active and fruitful for a substantial time.

## Acknowledgments

The authors are thankful to Prof Adi Salomon for fruitful discussions. MS is grateful to the financial and computing support by the Air Force Office of Scientific Research under Grant No. FA9550-15-1-0189. Both MS and AN would like to thank Binational Science Foundation for generous financial support through collaborative Grant No. 2014113. AN also acknowledges financial support from the University of Pennsylvania.

## References

- [1] Drude P 1900 Zur Elektronentheorie der Metalle *Ann. Phys.* **303** 566
- [2] Drude P 1900 Zur Elektronentheorie der Metalle; II. Teil. Galvanomagnetische und thermomagnetische Effecte *Ann. Phys.* **308** 369

<sup>14</sup>This statement holds in the linear response regime, but this casts doubt also on the integrity of nonlinear response signal obtained in a classical description.

- [3] Ashcroft N W and Mermin N D 1976 *Solid State Physics* (Fort Worth: Saunders College Publishing)
- [4] Kreibig U and Vollmer M 1995 *Optical Properties of Metal Clusters* (Berlin: Springer)
- [5] Rakic A D, Djuricic A B, Elazar J M and Majewski M L 1998 Optical properties of metallic films for vertical-cavity optoelectronic devices *Appl. Opt.* **37** 5271–83
- [6] Raether H 1988 Surface-plasmons on smooth and rough surfaces and on gratings *Springer Tr. Mod. Phys.* **111** 1–133
- [7] Sarid D and Challener W 2010 *Modern Introduction to Surface Plasmons: Theory, Mathematica Modeling, and Applications* (Cambridge: Cambridge University Press)
- [8] Low T, Chaves A, Caldwell J D, Kumar A, Fang N X, Avouris P, Heinz T F, Guinea F, Martin-Moreno L and Koppens F 2017 Polaritons in layered two-dimensional materials *Nat. Mater.* **16** 182–94
- [9] Garcia de Abajo F J 2007 Colloquium: light scattering by particle and hole arrays *Rev. Mod. Phys.* **79** 1267
- [10] Barnes W L and Murray W A 2007 Plasmonic materials *Adv. Mater.* **19** 3771–82
- [11] Ru E L and Etchegoin P 2009 *Principles of Surface-Enhanced Raman Spectroscopy* (Amsterdam: Elsevier)
- [12] Gersten J and Nitzan A 1981 Spectroscopic properties of molecules interacting with small dielectric particles *J. Chem. Phys.* **75** 1139–52
- [13] Gersten J I and Nitzan A 1981 Electromagnetic theory of enhanced Raman scattering by molecules on rough surfaces *J. Chem. Phys.* **73** 3023–37
- [14] Kamat P V 2002 Photophysical, photochemical and photocatalytic aspects of metal nanoparticles *J. Phys. Chem. B* **106** 7729–44
- [15] Prodan E, Radloff C, Halas N J and Nordlander P 2003 A hybridization model for the plasmon response of complex nanostructures *Science* **302** 419
- [16] Nordlander P, Oubre C, Prodan E, Li K and Stockman M I 2004 Plasmon hybridization in nanoparticle dimers *Nano Lett.* **4** 899–903
- [17] Nordlander P and Prodan E 2004 Plasmon hybridization in nanoparticles near metallic surfaces *Nano Lett.* **4** 2209–13
- [18] Prodan E and Nordlander P 2004 Plasmon hybridization in spherical nanoparticles *J. Chem. Phys.* **120** 5444–54
- [19] Sukharev M and Nitzan A 2016 Plasmon transmission through excitonic subwavelength gaps *J. Chem. Phys.* **144** 144703
- [20] Banik M, El-Khoury P Z, Nag A, Rodriguez-Perez A, Guarrottgena N, Bazan G C and Apkarian V A 2012 Surface-enhanced raman trajectories on a nano-dumbbell: transition from field to charge transfer plasmons as the spheres fuse *ACS Nano* **6** 10343–54
- [21] Esteban R, Borisov A G, Nordlander P and Aizpurua J 2012 Bridging quantum and classical plasmonics with a quantum-corrected model *Nat. Commun.* **3** 825
- [22] Savage K J, Hawkeye M M, Esteban R, Borisov A G, Aizpurua J and Baumberg J J 2012 Revealing the quantum regime in tunnelling plasmonics *Nature* **491** 574–7
- [23] Marinica D C, Lourenço-Martins H, Aizpurua J and Borisov A G 2013 Plexciton quenching by resonant electron transfer from quantum emitter to metallic nanoantenna *Nano Lett.* **13** 5972–8
- [24] Teperik T V, Kazansky A K and Borisov A G 2016 Electron tunneling through water layer in nanogaps probed by plasmon resonances *Phys. Rev. B* **93** 155431
- [25] Rodarte A L and Tao A R 2017 Plasmon–exciton coupling between metallic nanoparticles and dye monomers *J. Phys. Chem. C* **121** 3496–502
- [26] Gersten J and Nitzan A 1980 Electromagnetic theory of enhanced Raman scattering by molecules adsorbed on rough surfaces *J. Chem. Phys.* **73** 3023–37
- [27] Stiles P L, Dieringer J A, Shah N C and Duynes R P V 2008 Surface-enhanced raman spectroscopy *Ann. Rev. Anal. Chem.* **1** 601–26
- [28] Schlücker S 2014 Surface-enhanced raman spectroscopy: concepts and chemical applications *Angew. Chem., Int. Ed.* **53** 4756–95
- [29] Gersten J I and Nitzan A 1985 Photophysics and photochemistry near surfaces and small particles *Surf. Sci.* **158** 165–89
- [30] Nitzan A and Brus L E 1981 Theoretical-model for enhanced photochemistry on rough surfaces *J. Chem. Phys.* **75** 2205–14
- [31] Gao S, Ueno K and Misawa H 2011 Plasmonic antenna effects on photochemical reactions *Acc. Chem. Res.* **44** 251–60
- [32] Gersten J I 2005 *Radiative Decay Engineering (Topics in Fluorescence Spectroscopy vol 8)* ed C D Geddes and J R Lakowicz (New York: Springer)
- [33] Chance R R, Prock A and Silbey R 1978 Molecular fluorescence and energy transfer near interfaces *Adv. Chem. Phys.* **37** 1–65
- [34] Drexhage K H, Fleck M, Kuhn H, Schaefer F P and Sperling W 1966 Beeinflussung Der Fluoreszenz Eines Europiumchelates Durch Einen Spiegel *Ber. Bunsenges. Phys. Chem.* **70** 1179–89
- [35] Drexhage K H, Kuhn H and Schaefer F P 1968 Variation of fluorescence decay time of a molecule in front of a mirror *Ber. Bunsenges. Phys. Chem.* **72** 329
- [36] Alivisatos A P, Waldeck D H and Harris C B 1985 Nonclassical behavior of energy transfer from molecules to metal surfaces: biacetyl( $^2\pi\pi^*/Ag(111)$ ) *J. Chem. Phys.* **82** 541–7
- [37] Dulkeith E, Morteaux A C, Niedereichholz T, Klar T A, Feldmann J, Levi S A, van Veggel F C J M, Reinhardt D N and Moller M 2002 Fluorescence quenching of dye molecules near gold nanoparticles *Phys. Rev. Lett.* **89** 203002
- [38] Dulkeith E, Ringler M, Klar T A, Feldmann J, Javier A M and Parak W J 2005 Gold nanoparticles quench fluorescence by phase induced radiative rate suppression *Nano Lett.* **5** 585–9
- [39] Soller T, Ringler M, Wunderlich M, Klar T A, Feldmann J, Josel H P, Markert Y, Nichtl A and Kurzinger K 2007 Radiative and nonradiative rates of phosphors attached to gold nanoparticles *Nano Lett.* **7** 1941–6
- [40] Schuler B, Lipman E A, Steinbach P J, Kumke M and Eaton W A 2005 Polyproline and the ‘spectroscopic ruler’ revisited with single-molecule fluorescence *Proc. Natl Acad. Sci.* **102** 2754–9
- [41] Yun C S, Javier A, Jennings T, Fisher M, Hira S, Peterson S, Hopkins B, Reich N O and Strouse G F 2005 Nanometal surface energy transfer in optical rulers, breaking the FRET barrier *J. Am. Chem. Soc.* **127** 3115–9
- [42] Jennings T L, Singh M P and Strouse G F 2006 Fluorescent lifetime quenching near  $d = 1.5$  nm gold nanoparticles: probing NSET validity *J. Am. Chem. Soc.* **128** 5462–7
- [43] Huang Y-F, Ma K-H, Kang K-B, Zhao M, Zhang Z-L, Liu Y-X, Wen T, Wang Q, Qiu W-Y and Qiu D 2013 Core-shell plasmonic nanostructures to fine-tune long ‘Au nanoparticle-fluorophore’ distance and radiative dynamics *Colloids Surf. A* **421** 101–8
- [44] Gaudreau L, Tielrooij K J, Prawiroatmodjo G E D K, Osmond J, de Abajo F J G and Koppens F H L 2013 Universal distance-scaling of nonradiative energy transfer to graphene *Nano Lett.* **13** 2030–5
- [45] Sen T and Patra A 2012 Recent advances in energy transfer processes in gold-nanoparticle-based assemblies *J. Phys. Chem. C* **116** 17307–17
- [46] Ghosh S K and Pal T 2009 Photophysical aspects of molecular probes near nanostructured gold surfaces *Phys. Chem. Chem. Phys.* **11** 3831–44
- [47] Fuchs R and Barrera R G 1981 Dynamical response of a dipole near the surface of a nonlocal metal *Phys. Rev. B* **24** 2940–50

- [48] Ford G W and Weber W H 1984 Electromagnetic interactions of molecules with metal surfaces *Phys. Rep.* **113** 195–287
- [49] Leung P T 1990 Decay of molecules at spherical surfaces: nonlocal effects *Phys. Rev. B* **42** 7622–5
- [50] D’Agostino S, Della Sala F and Andreani L C 2013 Dipole-excited surface plasmons in metallic nanoparticles: engineering decay dynamics within the discrete-dipole approximation *Phys. Rev. B* **87** 205413
- [51] Singh M P and Strouse G F 2010 Involvement of the LSPR spectral overlap for energy transfer between a dye and Au nanoparticle *J. Am. Chem. Soc.* **132** 9383–91
- [52] Sen T, Halder K K and Patra A 2008 Au nanoparticle-based surface energy transfer probe for conformational changes of BSA protein *J. Phys. Chem. C* **112** 17945–51
- [53] Sen T and Patra A 2008 Resonance energy transfer from rhodamine 6G to gold nanoparticles by steady-state and time-resolved spectroscopy *J. Phys. Chem. C* **112** 3216–22
- [54] Saraswat S, Desiredy A, Zheng D, Guo L, Lu H P, Bigioni T P and Isailovic D 2011 Energy transfer from fluorescent proteins to metal nanoparticles *J. Phys. Chem. C* **115** 17587–93
- [55] Sukharev M, Freifeld N and Nitzan A 2014 Numerical calculations of radiative and non-radiative relaxation of molecules near metal particles *J. Phys. Chem. C* **118** 10545–51
- [56] Ruppin R 1982 Decay of an excited molecule near a small metal sphere *J. Chem. Phys.* **76** 1681–4
- [57] Persson B N J and Lang N D 1982 Electron-hole-pair quenching of excited states near a metal *Phys. Rev. B* **26** 5409–15
- [58] Andreussi O, Corni S, Mennucci B and Tomasi J 2004 Radiative and nonradiative decay rates of a molecule close to a metal particle of complex shape *J. Chem. Phys.* **121** 10190–202
- [59] Bhowmick S, Saini S, Shenoy V B and Bagchi B 2006 Resonance energy transfer from a fluorescent dye to a metal nanoparticle *J. Chem. Phys.* **125** 181102
- [60] Saini S, Bhowmick S, Shenoy V B and Bagchi B 2007 Rate of excitation energy transfer between fluorescent dyes and nanoparticles *J. Photochem. Photobiol. A* **190** 335–41
- [61] Saini S, Shenoy V B and Bagchi B 2008 Excitation energy transfer between non-spherical metal nanoparticles: effects of shape and orientation on distance dependence of transfer rate *J. Phys. Chem. C* **112** 6299–306
- [62] Saini S, Srinivas G and Bagchi B 2009 Distance and orientation dependence of excitation energy transfer: from molecular systems to metal nanoparticles *J. Phys. Chem. B* **113** 1817–32
- [63] Mertens H, Koenderink A F and Polman A 2007 Plasmon-enhanced luminescence near noble-metal nanospheres: comparison of exact theory and an improved Gersten and Nitzan model *Phys. Rev. B* **76** 115123–12
- [64] Rogobete L, Kaminski F, Agio M and Sandoghdar V 2007 Design of plasmonic nanoantennae for enhancing spontaneous emission *Opt. Lett.* **32** 1623–5
- [65] Mertens H and Polman A 2009 Strong luminescence quantum-efficiency enhancement near prolate metal nanoparticles: dipolar versus higher-order modes *J. Appl. Phys.* **105** 044302
- [66] Francs G C D, Girard C, Laroche T, Leveque G and Martin O J F 2007 Theory of molecular excitation and relaxation near a plasmonic device *J. Chem. Phys.* **127** 034701
- [67] Jun Y C, Kekatpure R D, White J S and Brongersma M L 2008 Nonresonant enhancement of spontaneous emission in metal-dielectric-metal plasmon waveguide structures *Phys. Rev. B* **78** 153111
- [68] Chen Y, Nielsen T R, Gregersen N, Lodahl P and Mørk J 2010 Finite-element modeling of spontaneous emission of a quantum emitter at nanoscale proximity to plasmonic waveguides *Phys. Rev. B* **81** 125431
- [69] Chen Y T, Gregersen N, Nielsen T R, Mørk J and Lodahl P 2010 Spontaneous decay of a single quantum dot coupled to a metallic slot waveguide in the presence of leaky plasmonic modes *Opt. Express* **18** 12489–98
- [70] Pustovit V N and Shahbazyan T V 2010 Plasmon-mediated superradiance near metal nanostructures *Phys. Rev. B* **82** 075429
- [71] Pustovit V N 2010 Enhanced fluorescence of a molecular dipole near metal nanoparticle *Physica B* **405** 754–7
- [72] Moroz A 2011 Superconvergent representation of the Gersten–Nitzan and Ford–Weber nonradiative rates *J. Phys. Chem. C* **115** 19546–56
- [73] Polemi A and Shuford K L 2012 Distance dependent quenching effect in nanoparticle dimers *J. Chem. Phys.* **136** 184703
- [74] Agarwal G S 1975 Quantum electrodynamics in the presence of dielectrics and conductors. IV. General theory for spontaneous emission in finite geometries *Phys. Rev. A* **12** 1475–97
- [75] Wijnands F, Pendry J B, Garcia-Vidal F J, Bell P M, Roberts P J and Moreno L M 1997 Green’s functions for Maxwell’s equations: application to spontaneous emission *Opt. Quantum Electron.* **29** 199–216
- [76] Xu Y, Vuckovic J S, Lee R K, Painter O J, Scherer A and Yariv A 1999 Finite-difference time-domain calculation of spontaneous emission lifetime in a microcavity *J. Opt. Soc. Am. B* **16** 465–74
- [77] Vuckovic J, Painter O, Xu Y, Yariv A and Scherer A 1999 Finite-difference time-domain calculation of the spontaneous emission coupling factor in optical microcavities *IEEE J. Quantum Electron.* **35** 1168–75
- [78] Ruppin R and Martin O J F 2004 Lifetime of an emitting dipole near various types of interfaces including magnetic and negative refractive materials *J. Chem. Phys.* **121** 11358–61
- [79] Marocico C A and Knoester J 2011 Effect of surface-plasmon polaritons on spontaneous emission and intermolecular energy-transfer rates in multilayered geometries *Phys. Rev. A* **84** 053824
- [80] Yannopapas V and Vitanov N V 2007 Spontaneous emission of a two-level atom placed within clusters of metallic nanoparticles *J. Phys.: Condens. Matter* **19** 096210
- [81] Shahbazyan T V 2016 Local density of states for nanoplasmonics *Phys. Rev. Lett.* **117** 207401
- [82] Neuhauser D and Lopata K 2007 Molecular nanopolaritons: cross manipulation of near-field plasmons and molecules. I. Theory and application to junction control *J. Chem. Phys.* **127** 154715–10
- [83] Lopata K and Neuhauser D 2009 Nonlinear nanopolaritons: finite-difference time-domain Maxwell–Schrödinger simulation of molecule-assisted plasmon transfer *J. Chem. Phys.* **131** 014701
- [84] Lopata K and Neuhauser D 2009 Multiscale Maxwell–Schrödinger modeling: a split field finite-difference time-domain approach to molecular nanopolaritons *J. Chem. Phys.* **130** 104707
- [85] Arntsen C, Lopata K, Wall M R, Bartell L and Neuhauser D 2011 Modeling molecular effects on plasmon transport: Silver nanoparticles with tartrazine *J. Chem. Phys.* **084101–7**
- [86] Nitzan A 2006 *Chemical Dynamics in Condensed Phases* (Oxford: Oxford University Press)
- [87] Kasha M, Rawls H R and El-Bayoumi M A 1965 The exciton model in molecular spectroscopy *Pure Appl. Chem.* **11** 371–92
- [88] Hawrylak P 1999 Excitonic artificial atoms: engineering optical properties of quantum dots *Phys. Rev. B* **60** 5597–608

- [89] Wheeler D A and Zhang J Z 2013 Exciton dynamics in semiconductor nanocrystals *Adv. Mater.* **25** 2878–96
- [90] Tzeng H-M, Wall K F, Long M B and Chang R K 1984 Laser emission from individual droplets at wavelengths corresponding to morphology-dependent resonances *Opt. Lett.* **9** 499–501
- [91] Qian S X, Snow J B and Chang R K 1985 Coherent raman mixing and coherent anti-stokes raman-scattering from individual micrometer-size droplets *Opt. Lett.* **10** 499–501
- [92] Snow J B, Qian S X and Chang R K 1985 Stimulated raman-scattering from individual water and ethanol droplets at morphology-dependent resonances *Opt. Lett.* **10** 37–9
- [93] Tzeng H M, Long M B, Chang R K and Barber P W 1985 Laser-induced shape distortions of flowing droplets deduced from morphology-dependent resonances in fluorescence-spectra *Opt. Lett.* **10** 209–11
- [94] Glauber R J and Prasad S 2000 Polarium model: reflection and transmission of coherent radiation *Phys. Rev. A* **61** 063815
- [95] Prasad S and Glauber R J 2000 Polarium model: coherent radiation by a resonant medium *Phys. Rev. A* **61** 063814
- [96] Prasad S and Glauber R J 2010 Coherent radiation by a spherical medium of resonant atoms *Phys. Rev. A* **82** 063805
- [97] Prasad S and Glauber R J 2011 Coherent scattering by a spherical medium of resonant atoms *Phys. Rev. A* **83** 063821
- [98] Svidzinsky A A, Chang J-T and Scully M O 2010 Cooperative spontaneous emission of N atoms: many-body eigenstates, the effect of virtual Lamb shift processes, and analogy with radiation of N classical oscillators *Phys. Rev. A* **81** 053821
- [99] Takeda H 2012 Collective population evolution of two-level atoms based on mean-field theory *Phys. Rev. A* **85** 023837
- [100] Dicke R H 1954 Coherence in spontaneous radiation processes *Phys. Rev.* **93** 99–110
- [101] Bonifacio R and Lugiato L A 1975 Cooperative radiation processes in two-level systems: superfluorescence *Phys. Rev. A* **11** 1507–21
- [102] Kiselev A S, Kiselev A S and Rozanov N N 2008 Nanosized discrete dissipative solitons in resonantly excited molecular J-aggregates *JETP Lett.* **87** 663–6
- [103] Manassah J T 2010 Minimum size requirements for open-ended lasing from N two-level atoms in infinite cylindrical samples *Phys. Rev. A* **82** 045803
- [104] Deng H, Haug H and Yamamoto Y 2010 Exciton-polariton Bose–Einstein condensation *Rev. Mod. Phys.* **82** 1489–537
- [105] Zhao H, Moehl S and Kalt H 2002 Coherence length of excitons in a semiconductor quantum well *Phys. Rev. Lett.* **89** 097401
- [106] Valteau S, Saikin S K, Yung M-H and Guzik A A 2012 Exciton transport in thin-film cyanine dye J-aggregates *J. Chem. Phys.* **137** 034109
- [107] Pockrand I, Swalen J D, Santo R, Brillante A and Philpott M R 1978 Optical properties of organic dye monolayers by surface plasmon spectroscopy *J. Chem. Phys.* **69** 4001–11
- [108] Törmä P and Barnes W L 2015 Strong coupling between surface plasmon polaritons and emitters: a review *Rep. Prog. Phys.* **78** 013901
- [109] Govorov A O, Bryant G W, Zhang W, Skeini T, Lee J, Kotov N A, Slocik J M and Naik R R 2006 Exciton–plasmon interaction and hybrid excitons in semiconductor-metal nanoparticle assemblies *Nano Lett.* **6** 984–94
- [110] Salomon A, Genet C and Ebbesen T W 2009 Molecule-light complex: dynamics of hybrid molecule–surface plasmon states *Angew. Chem., Int. Ed.* **48** 8748–51
- [111] Achermann M 2010 Exciton–plasmon interactions in metal-semiconductor nanostructures *J. Phys. Chem. Lett.* **1** 2837–43
- [112] Andersen M L, Stobbe S, Sorensen A S and Lodahl P 2011 Strongly modified plasmon-matter interaction with mesoscopic quantum emitters *Nat. Phys.* **7** 215–8
- [113] Climente J I, Movilla J L, Goldoni G and Planelles J 2011 Excitonic resonance in semiconductor–metal nanohybrids *J. Phys. Chem. C* **115** 15868–74
- [114] Cohen-Hoshen E, Bryant G W, Pinkas I, Sperling J and Bar-Joseph I 2012 Exciton–plasmon interactions in quantum dot–gold nanoparticle structures *Nano Lett.* **12** 4260–4
- [115] Estrin Y, Rich D H, Kretinin A V and Shtrikman H 2013 Influence of metal deposition on exciton–surface plasmon polariton coupling in GaAs/AlAs/GaAs core–shell nanowires studied with time-resolved cathodoluminescence *Nano Lett.* **13** 1602–10
- [116] Manjavacas A, García de Abajo F J and Nordlander P 2011 Quantum plexcitonics: strongly interacting plasmons and excitons *Nano Lett.* **11** 2318–23
- [117] Raino G, Stoferle T, Park C, Kim H C, Topuria T, Rice P M, Chin I J, Miller R D and Mahrt R F 2011 Plasmonic nanohybrid with ultrasmall ag nanoparticles and fluorescent dyes *ACS Nano* **5** 3536–41
- [118] Niesen B, Rand B P, Van Dorpe P, Cheyng D, Shen H H, Maes B and Heremans P 2012 Near-field interactions between metal nanoparticle surface plasmons and molecular excitons in thin-films. Part I: absorption *J. Phys. Chem. C* **116** 24206–14
- [119] Niesen B, Rand B P, Van Dorpe P, Cheyng D, Fron E, Van der Auweraer M and Heremans P 2012 Near-field interactions between metal nanoparticle surface plasmons and molecular excitons in thin-films. Part II: emission *J. Phys. Chem. C* **116** 24215–23
- [120] Uwada T, Toyota R, Masuhara H and Asahi T 2007 Single particle spectroscopic investigation on the interaction between exciton transition of cyanine dye J-aggregates and localized surface plasmon polarization of gold nanoparticles *J. Phys. Chem. C* **111** 1549–52
- [121] El Kabbash M, Rahimi Rashed A, Sreekanth K V, De Luca A, Infusino M and Strangi G 2016 Plasmon-exciton resonant energy transfer: across scales hybrid systems *J. Nanomater.* **2016** 21
- [122] Gersten J I and Nitzan A 1984 Accelerated energy transfer between molecules near a solid particle *Chem. Phys. Lett.* **104** 31–7
- [123] Hua X M, Gersten J I and Nitzan A 1985 Theory of energy transfer between molecules near solid-dielectric particles *J. Chem. Phys.* **83** 3650–9
- [124] Andrew P and Barnes W L 2004 Energy transfer across a metal film mediated by surface plasmon polaritons *Science* **306** 1002–5
- [125] Sun M, Pullerits T, Kjellberg P, Beenken W J D and Han K 2006 Control of emission by intermolecular fluorescence resonance energy transfer and intermolecular charge transfer *J. Phys. Chem.* **110** 6324–8
- [126] Gersten J I 2007 Fluorescence resonance energy transfer near thin films on surfaces *Plasmonics* **2** 65–77
- [127] Govorov A O, Lee J and Kotov N A 2007 Theory of plasmon-enhanced Forster energy transfer in optically excited semiconductor and metal nanoparticles *Phys. Rev. B* **76** 125308
- [128] Zhang J, Fu Y and Lakowicz J R 2007 Enhanced Forster resonance energy transfer (FRET) on a single metal particle *J. Phys. Chem. C* **111** 50–6
- [129] Komarala V K, Bradley A L, Rakovich Y P, Byrne S J, Gun'ko Y K and Rogach A L 2008 Surface plasmon enhanced Forster resonance energy transfer between the CdTe quantum dots *Appl. Phys. Lett.* **93** 123102

- [130] Reil F, Hohenester U, Krenn J R and Leitner A 2008 Förster-type resonant energy transfer influenced by metal nanoparticles *Nano Lett.* **8** 4128–33
- [131] Wei W, Li S, Qin L, Xue C, Millstone J E, Xu X, Schatz G C and Mirkin C A 2008 Surface plasmon-mediated energy transfer in heterogap Au–Ag nanowires *Nano Lett.* **8** 3446–9
- [132] Marocico C A and Knoester J 2009 Intermolecular resonance energy transfer in the presence of a dielectric cylinder *Phys. Rev. A* **79** 053816
- [133] Chung H Y, Leung P T and Tsai D P 2010 Enhanced intermolecular energy transfer in the vicinity of a plasmonic nanorice *Plasmonics* **5** 363–8
- [134] Martín-Cano D, Martín-Moreno L, García-Vidal F J and Moreno E 2010 Resonance energy transfer and superradiance mediated by plasmonic nanowaveguides *Nano Lett.* **10** 3129–34
- [135] Su X R, Zhang W, Zhou L, Peng X N and Wang Q Q 2010 Plasmon-enhanced Förster energy transfer between semiconductor quantum dots: multipole effects *Opt. Express* **18** 6516–21
- [136] Faessler V, Hrelescu C, Lutich A A, Osinkina L, Mayilo S, Jackel F and Feldmann J 2011 Accelerating fluorescence resonance energy transfer with plasmonic nanoresonators *Chem. Phys. Lett.* **508** 67–70
- [137] Pustovit V N and Shahbazyan T V 2011 Resonance energy transfer near metal nanostructures mediated by surface plasmons *Phys. Rev. B* **83** 085427
- [138] Antón M A, Carreño F, Melle S, Calderón O G, Cabrera-Granado E, Cox J and Singh M R 2012 Plasmonic effects in excitonic population transfer in a driven semiconductor–metal nanoparticle hybrid system *Phys. Rev. B* **86** 155305
- [139] Lunz M, Zhang X, Gerard V A, Gun'ko Y K, Lesnyak V, Gaponik N, Susha A S, Rogach A L and Bradley A L 2012 Effect of metal nanoparticle concentration on localized surface plasmon mediated Förster resonant energy transfer *J. Phys. Chem. C* **116** 26529–34
- [140] Zhao L, Ming T, Shao L, Chen H J and Wang J F 2012 Plasmon-controlled Förster resonance energy transfer *J. Phys. Chem. C* **116** 8287–96
- [141] Gonzaga-Galeana J A and Zurita-Sanchez J R 2013 A revisit of the Förster energy transfer near a metallic spherical nanoparticle: (1) efficiency enhancement or reduction? (2) The control of the Förster radius of the unbounded medium. (3) The impact of the local density of states *J. Chem. Phys.* **139** 244302
- [142] Angioni A, Corni S and Mennucci B 2013 Can we control the electronic energy transfer in molecular dyads through metal nanoparticles? A QM/continuum investigation *Phys. Chem. Chem. Phys.* **15** 3294–303
- [143] Karanikolas V, Marocico C A and Bradley A L 2014 Spontaneous emission and energy transfer rates near a coated metallic cylinder *Phys. Rev. A* **89** 063817
- [144] Pustovit V N, Urbas A M and Shahbazyan T V 2014 Energy transfer in plasmonic systems *J. Opt.* **16** 114015
- [145] Roslyak O, Cherqui C, Dunlap D H and Piryatinski A 2014 Effect of localized surface-plasmon mode on exciton transport and radiation emission in carbon nanotubes *J. Phys. Chem. B* **118** 8070–80
- [146] Chou K F and Dennis A M 2015 Förster resonance energy transfer between quantum dot donors and quantum dot acceptors *Sensors* **15** 13288–325
- [147] Kucherenko M G, Stepanov V N and Kruchinin N Y 2015 Intermolecular nonradiative energy transfer in clusters with plasmonic nanoparticles *Opt. Spectrosc.* **118** 103–10
- [148] Marocico C A, Zhang X and Bradley A L 2016 A theoretical investigation of the influence of gold nanosphere size on the decay and energy transfer rates and efficiencies of quantum emitters *J. Chem. Phys.* **144** 024108
- [149] Barnes W L, Dereux A and Ebbesen T W 2003 Surface plasmon subwavelength optics *Nature* **424** 824–30
- [150] Maier S A, Brongersma M L, Kik P G, Meltzer S, Requicha A A G, Koel B E and Atwater H A 2001 Plasmonics—a route to nanoscale optical devices *Adv. Mater.* **13** 1501–5
- [151] Maier S A, Kik P G, Atwater H A, Meltzer S, Harel E, Koel B E and Requicha A A G 2003 Local detection of electromagnetic energy transport below the diffraction limit in metal nanoparticle plasmon waveguides *Nat. Mater.* **2** 229–32
- [152] Zia R, Selker M D, Catrysse P B and Brongersma M L 2004 Geometries and materials for subwavelength surface plasmon modes *J. Opt. Soc. Am. A* **21** 2442–6
- [153] Oulton R F, Sorger V J, Genov D A, Pile D F P and Zhang X 2008 A hybrid plasmonic waveguide for subwavelength confinement and long-range propagation *Nat. Photon.* **2** 496–500
- [154] Grandidier J, des Francs G C, Massenot S, Bouhelier A, Markey L, Weeber J-C, Finot C and Dereux A 2009 Gain-assisted propagation in a plasmonic waveguide at telecom wavelength *Nano Lett.* **9** 2935–9
- [155] Veronis G, Yu Z, Kocabas S E, Miller D A B, Brongersma M L and Fan S 2009 Metal-dielectric-metal plasmonic waveguide devices for manipulating light at the nanoscale *Chin. Opt. Lett.* **7** 302–8
- [156] Sorger V J, Ye Z, Oulton R F, Wang Y, Bartal G, Yin X and Zhang X 2011 Experimental demonstration of low-loss optical waveguiding at deep sub-wavelength scales *Nat. Commun.* **2** 331
- [157] Ellenbogen T and Crozier K B 2011 Exciton-polariton emission from organic semiconductor optical waveguides *Phys. Rev. B* **84** 161304
- [158] Ellenbogen T, Steinvurzel P and Crozier K B 2011 Strong coupling between excitons in J-aggregates and waveguide modes in thin polymer films *Appl. Phys. Lett.* **98** 261103
- [159] Paul A, Solis D, Bao K, Chang W-S, Nauert S, Vidgerman L, Zubarev E R, Nordlander P and Link S 2012 Identification of higher order long-propagation-length surface plasmon polariton modes in chemically prepared gold nanowires *ACS Nano* **6** 8105–13
- [160] González-Tudela A, Huidobro P A, Martín-Moreno L, Tejedor C and García-Vidal F J 2013 Theory of strong coupling between quantum emitters and propagating surface plasmons *Phys. Rev. Lett.* **110** 126801
- [161] Solis D, Paul A, Olson J, Slaughter L S, Swanglap P, Chang W-S and Link S 2013 Turning the corner: efficient energy transfer in bent plasmonic nanoparticle chain waveguides *Nano Lett.* **13** 4779–84
- [162] Gu Z, Liu S, Sun S C, Wang K, Lyu Q, Xiao S and Song Q 2015 Photon hopping and nanowire based hybrid plasmonic waveguide and ring-resonator *Sci. Rep.* **5** 9171
- [163] Carmeli I, Cohen M, Heifler O, Lilach Y, Zalevsky Z, Mujica V and Richter S 2015 Spatial modulation of light transmission through a single microcavity by coupling of photosynthetic complex excitations to surface plasmons *Nat. Commun.* **6** 7334
- [164] Sadeghi S M 2009 Plasmonic metaresonances: molecular resonances in quantum dot–metallic nanoparticle conjugates *Phys. Rev. B* **79** 233309–4
- [165] Pustovit V N and Shahbazyan T V 2009 Cooperative emission of light by an ensemble of dipoles near a metal nanoparticle: the plasmonic Dicke effect *Phys. Rev. Lett.* **102** 077401
- [166] Choquette J J, Marzlin K-P and Sanders B C 2010 Superradiance, subradiance, and suppressed superradiance of dipoles near a metal interface *Phys. Rev. A* **82** 023827

- [167] Shahbazyan T V and Pustovit V N 2011 Plasmonic Dicke effect *Appl. Phys. A* **103** 755–8
- [168] Teperik T V and Degiron A 2012 Superradiant optical emitters coupled to an array of nanosize metallic antennas *Phys. Rev. Lett.* **108** 147401
- [169] Sadeghi S M 2012 Quantum coherence effects in hybrid nanoparticle molecules in the presence of ultra-short dephasing times *Appl. Phys. Lett.* **101** 213102
- [170] Sadeghi S M 2013 Ultrafast plasmonic field oscillations and optics of molecular resonances caused by coherent exciton-plasmon coupling *Phys. Rev. A* **88** 013831
- [171] Sadeghi S M and Patty K D 2014 Ultrafast dynamics induced by coherent exciton-plasmon coupling in quantum dot-metallic nanoshell systems *J. Opt. Soc. Am. B* **31** 120–7
- [172] Sorokin A V, Zabolotskii A A, Pereverzev N V, Yefimova S L, Malyukin Y V and Plekhanov A I 2014 Plasmon controlled exciton fluorescence of molecular aggregates *J. Phys. Chem. C* **118** 7599–605
- [173] Khitrova G, Gibbs H M, Kira M, Koch S W and Scherer A 2006 Vacuum Rabi splitting in semiconductors *Nat. Phys.* **2** 81–90
- [174] Gibbs H M, Khitrova G and Koch S W 2011 Exciton-polariton light-semiconductor coupling effects *Nat. Photon.* **5** 273
- [175] Lodahl P, Mahmoodian S and Stobbe S 2015 Interfacing single photons and single quantum dots with photonic nanostructures *Rev. Mod. Phys.* **87** 347–400
- [176] Miroshnichenko A E, Flach S and Kivshar Y S 2010 Fano resonances in nanoscale structures *Rev. Mod. Phys.* **82** 2257–98
- [177] Novotny L 2010 Strong coupling, energy splitting, and level crossings: a classical perspective *Am. J. Phys.* **78** 1199–202
- [178] Shore B W and Knight P L 1993 The Jaynes-Cummings model *J. Mod. Opt.* **40** 1195–238
- [179] Gantzounis G, Stefanou N and Yannopoulos V 2005 Optical properties of a periodic monolayer of metallic nanospheres on a dielectric waveguide *J. Phys.: Condens. Matter* **17** 1791–802
- [180] Jain P K, Eustis S and El-Sayed M A 2006 Plasmon coupling in nanorod assemblies: optical absorption, discrete dipole approximation simulation, and exciton-coupling model *J. Phys. Chem. B* **110** 18243–9253
- [181] Jain P K and El-Sayed M A 2008 Surface plasmon coupling and its universal size scaling in metal nanostructures of complex geometry: elongated particle pairs and nanosphere trimers *J. Phys. Chem. C* **112** 4954–60
- [182] Harris N, Arnold M D, Blaber M G and Ford M J 2009 Plasmonic resonances of closely coupled gold nanosphere chains *J. Phys. Chem. C* **113** 2784–91
- [183] Chergui M, Melikyan A and Minassian H 2009 Calculation of surface plasmon frequencies of two, three, and four strongly interacting nanospheres *J. Phys. Chem. C* **113** 6463–71
- [184] Halas N J, Lal S, Chang W-S, Link S and Nordlander P 2011 Plasmons in strongly coupled metallic nanostructures *Chem. Rev.* **111** 3913–61
- [185] Letnes P A, Simonsen I and Mills D L 2011 Substrate influence on the plasmonic response of clusters of spherical nanoparticles *Phys. Rev. B* **83** 075426
- [186] Chang W-S, Willingham B, Slaughter L S, Dominguez-Medina S, Swanglap P and Link S 2012 Radiative and nonradiative properties of single plasmonic nanoparticles and their assemblies *Acc. Chem. Res.* **45** 1936–45
- [187] Salomon A, Prior Y, Fedoruk M, Feldmann J, Kolkowski R and Zyss J 2014 Plasmonic coupling between metallic nanocavities *J. Opt.* **16** 114012
- [188] Bellessa J, Bonnand C, Plenet J C and Mugnier J 2004 Strong coupling between surface plasmons and excitons in an organic semiconductor *Phys. Rev. Lett.* **93** 036404
- [189] Dintinger J, Klein S, Bustos F, Barnes W L and Ebbesen T W 2005 Strong coupling between surface plasmon-polaritons and organic molecules in subwavelength hole arrays *Phys. Rev. B* **71** 035424
- [190] Cade N I, Ritman-Meer T and Richards D 2009 Strong coupling of localized plasmons and molecular excitons in nanostructured silver films *Phys. Rev. B* **79** 241404
- [191] Schwartz T, Hutchison J A, Genet C and Ebbesen T W 2011 Reversible switching of ultrastrong light-molecule coupling *Phys. Rev. Lett.* **106** 196405
- [192] Salomon A, Gordon R J, Prior Y, Seideman T and Sukharev M 2012 Strong coupling between molecular excited states and surface plasmon modes of a slit array in a thin metal film *Phys. Rev. Lett.* **109** 073002
- [193] Schlather A E, Large N, Urban A S, Nordlander P and Halas N J 2013 Near-field mediated plexcitonic coupling and giant rabi splitting in individual metallic dimers *Nano Lett.* **13** 3281–6
- [194] Vasa P *et al* 2008 Coherent exciton-surface-plasmon-polariton interaction in hybrid metal-semiconductor nanostructures *Phys. Rev. Lett.* **101** 116801
- [195] Vasa P, Pomraenke R, Cirmi G, De Re E, Wang W, Schwieger S, Leipold D, Runge E, Cerullo G and Lienau C 2010 Ultrafast manipulation of strong coupling in metal-molecular aggregate hybrid nanostructures *ACS Nano* **4** 7559–65
- [196] Vasa P and Lienau C 2010 An unusual marriage: coupling molecular excitons to surface plasmon polaritons in metal nanostructures *Angew. Chem., Int. Ed.* **49** 2476–7
- [197] Wang W, Vasa P, Pomraenke R, Vogelgesang R, De Sio A, Sommer E, Maiuri M, Manzoni C, Cerullo G and Lienau C 2014 Interplay between strong coupling and radiative damping of excitons and surface plasmon polaritons in hybrid nanostructures *ACS Nano* **8** 1056–64
- [198] Vasa P, Wang W, Pomraenke R, Lammers M, Maiuri M, Manzoni C, Cerullo G and Lienau C 2013 Real-time observation of ultrafast Rabi oscillations between excitons and plasmons in metal nanostructures with J-aggregates *Nat. Photon.* **7** 128–32
- [199] Sukharev M, Seideman T, Gordon R J, Salomon A and Prior Y 2014 Ultrafast energy transfer between molecular assemblies and surface plasmons in the strong coupling regime *ACS Nano* **8** 807–17
- [200] Sukharev M 2014 Control of optical properties of hybrid materials with chirped femtosecond laser pulses under strong coupling conditions *J. Chem. Phys.* **141** 084712
- [201] Zengin G, Wersäll M, Nilsson S, Antosiewicz T J, Käll M and Shegai T 2015 Realizing strong light-matter interactions between single-nanoparticle plasmons and molecular excitons at ambient conditions *Phys. Rev. Lett.* **114** 157401
- [202] Tsargorodska A, Cartron M L, Vasilev C, Kodali G, Mass O A, Baumberg J J, Dutton P L, Hunter C N, Törmä P and Leggett G J 2016 Strong coupling of localized surface plasmons to excitons in light-harvesting complexes *Nano Lett.* **16** 6850–6
- [203] Lidzey D G, Virgili T, Bradley D D C, Skolnick M S, Walker S and Whittaker D M 1999 Observation of strong exciton-photon coupling in semiconductor microcavities containing organic dyes and J-aggregates *Opt. Mater.* **12** 243–7
- [204] Walther H, Benjamin T H V, Berthold-Georg E and Thomas B 2006 Cavity quantum electrodynamics *Rep. Prog. Phys.* **69** 1325
- [205] Byrnes T, Kim N Y and Yamamoto Y 2014 Exciton-polariton condensates *Nat. Phys.* **10** 803–13



- [206] Coles D M, Somaschi N, Michetti P, Clark C, Lagoudakis P G, Savvidis P G and Lidzey D G 2014 Polariton-mediated energy transfer between organic dyes in a strongly coupled optical microcavity *Nat. Mater.* **13** 712–9
- [207] Moody G, McDonald C, Feldman A, Harvey T, Mirin R P and Silverman K L 2016 Electronic enhancement of the exciton coherence time in charged quantum dots *Phys. Rev. Lett.* **116** 037402
- [208] Chikkaraddy R, de Nijs B, Benz F, Barrow S J, Scherman O A, Rosta E, Demetriadou A, Fox P, Hess O and Baumberg J J 2016 Single-molecule strong coupling at room temperature in plasmonic nanocavities *Nature* **535** 127–30
- [209] Santhosh K, Bitton O, Chuntunov L and Haran G 2016 Vacuum Rabi splitting in a plasmonic cavity at the single quantum emitter limit *Nat. Commun.* **7** 11823
- [210] Park D J, Ku J C, Sun L, Lethiec C M, Stern N P, Schatz G C and Mirkin C A 2017 Directional emission from dye-functionalized plasmonic DNA superlattice microcavities *Proc. Natl Acad. Sci. USA* **114** 457–61
- [211] Ebbesen T W 2016 Hybrid light–matter states in a molecular and material science perspective *Acc. Chem. Res.* **49** 2403–12
- [212] Novotny L and Hecht B 2006 *Principles of Nano-Optics* (Cambridge: Cambridge University Press)
- [213] Purcell E M 1946 *Phys. Rev.* **69** 681
- [214] Kristensen P T and Hughes S 2014 Modes and mode volumes of leaky optical cavities and plasmonic nanoresonators *ACS Photonics* **1** 2–10
- [215] Vergauwe R M A, George J, Chervy T, Hutchison J A, Shalabney A, Torbeev V Y and Ebbesen T W 2016 Quantum strong coupling with protein vibrational modes *J. Phys. Chem. Lett.* **7** 4159–64
- [216] George J, Chervy T, Shalabney A, Devaux E, Hiura H, Genet C and Ebbesen T W 2016 Multiple Rabi splittings under ultrastrong vibrational coupling *Phys. Rev. Lett.* **117** 153601
- [217] Sukharev M and Charron E 2017 Molecular plasmonics: the role of rovibrational molecular states in exciton-plasmon materials under strong-coupling conditions *Phys. Rev. B* **95** 115406
- [218] White A J, Sukharev M and Galperin M 2012 Molecular nanoplasmonics: self-consistent electrostatics in current-carrying junctions *Phys. Rev. B* **86** 205324
- [219] Lee S J, Piorek B D, Meinhardt C D and Moskovits M 2010 Photoreduction at a distance: facile, nonlocal photoreduction of Ag ions in solution by plasmon-mediated photoemitted electrons *Nano Lett.* **10** 1329–34
- [220] Lee Y K, Jung C H, Park J, Seo H, Somorjai G A and Park J Y 2011 Surface plasmon-driven hot electron flow probed with metal-semiconductor nanodiodes *Nano Lett.* **11** 4251–5
- [221] Wang P, Huang B, Dai Y and Whangbo M-H 2012 Plasmonic photocatalysts: harvesting visible light with noble metal nanoparticles *Phys. Chem. Chem. Phys.* **14** 9813–25
- [222] Mukherjee S, Libisch F, Large N, Neumann O, Brown L V, Cheng J, Lassiter J B, Carter E A, Nordlander P and Halas N J 2012 Hot electrons do the impossible: plasmon-induced dissociation of H<sub>2</sub> on Au *Nano Lett.* **13** 240–7
- [223] Aruda K O, Tagliazucchi M, Sweeney C M, Hannah D C and Weiss E A 2013 The role of interfacial charge transfer-type interactions in the decay of plasmon excitations in metal nanoparticles *Phys. Chem. Chem. Phys.* **15** 7441–9
- [224] Wu K, Rodríguez-Córdoba W E, Yang Y and Lian T 2013 Plasmon-induced hot electron transfer from the Au Tip to CdS Rod in CdS–Au nanoheterostructures *Nano Lett.* **13** 5255–63
- [225] Mubeen S, Lee J, Singh N, Kramer S, Stucky G D and Moskovits M 2013 An autonomous photosynthetic device in which all charge carriers derive from surface plasmons *Nat. Nano* **8** 247–51
- [226] Chalabi H and Brongersma M L 2013 Plasmonics: harvest season for hot electrons *Nat. Nano* **8** 229–30
- [227] Conklin D, Nanayakkara S, Park T H, Lagadec M F, Stecher J T, Chen X, Therien M J and Bonnell D A 2013 Exploiting plasmon-induced hot electrons in molecular electronic devices *ACS Nano* **7** 4479–86
- [228] DuChene J S, Sweeny B C, Johnston-Peck A C, Su D, Stach E A and Wei W D 2014 Prolonged hot electron dynamics in plasmonic-metal/semiconductor heterostructures with implications for solar photocatalysis *Angew. Chem., Int. Ed.* **53** 7887–91
- [229] Qian K *et al* 2014 Surface plasmon-driven water reduction: gold nanoparticle size matters *J. Am. Chem. Soc.* **136** 9842–5
- [230] Sil D, Gilroy K D, Niaux A, Boulesbaa A, Neretina S and Borguet E 2014 Seeing is believing: hot electron based gold nanoplasmonic optical hydrogen sensor *ACS Nano* **8** 7755–62
- [231] Kim K, Choi J Y and Shin K S 2015 Photoreduction of 4-nitrobenzenethiol on Au by hot electrons plasmonically generated from Ag nanoparticles: gap-mode surface-enhanced raman scattering observation *J. Phys. Chem. C* **119** 5187–94
- [232] Mubeen S, Lee J, Liu D, Stucky G D and Moskovits M 2015 Panchromatic photoproduction of H<sub>2</sub> with surface plasmons *Nano Lett.* **15** 2132–6
- [233] Moskovits M 2015 The case for plasmon-derived hot carrier devices *Nat. Nano* **10** 6–8
- [234] Brandt N C, Keller E L and Frontiera R R 2016 Ultrafast surface-enhanced raman probing of the role of hot electrons in plasmon-driven chemistry *J. Phys. Chem. Lett.* **7** 3179–85
- [235] Reineck P, Brick D, Mulvaney P and Bach U 2016 Plasmonic hot electron solar cells: the effect of nanoparticle size on quantum efficiency *J. Phys. Chem. Lett.* **7** 4137–41
- [236] Kornbluth M, Nitzan A and Seideman T 2013 Light-induced electronic non-equilibrium in plasmonic particles *J. Chem. Phys.* **138** 174707
- [237] Govorov A O, Zhang H and Gun'ko Y K 2013 Theory of photoinjection of hot plasmonic carriers from metal nanostructures into semiconductors and surface molecules *J. Phys. Chem. C* **117** 16616–31
- [238] Manjavacas A, Liu J G, Kulkarni V and Nordlander P 2014 Plasmon-induced hot carriers in metallic nanoparticles *ACS Nano* **8** 7630–8
- [239] Govorov A O, Zhang H, Demir H V and Gun'ko Y K 2014 Photogeneration of hot plasmonic electrons with metal nanocrystals: quantum description and potential applications *Nano Today* **9** 85–101
- [240] Zhang H and Govorov A O 2014 Optical generation of hot plasmonic carriers in metal nanocrystals: the effects of shape and field enhancement *J. Phys. Chem. C* **118** 7606–14
- [241] Besteiro L V and Govorov A O 2016 Amplified generation of hot electrons and quantum surface effects in nanoparticle dimers with plasmonic hot spots *J. Phys. Chem. C* **120** 19329–39
- [242] Brown A M, Sundararaman R, Narang P, Goddard W A and Atwater H A 2016 Nonradiative plasmon decay and hot carrier dynamics: effects of phonons, surfaces, and geometry *ACS Nano* **10** 957–66
- [243] Brongersma M L, Halas N J and Nordlander P 2015 Plasmon-induced hot carrier science and technology *Nat. Nano* **10** 25–34

- [244] Park J Y, Baker L R and Somorjai G A 2015 Role of hot electrons and metal–oxide interfaces in surface chemistry and catalytic reactions *Chem. Rev.* **115** 2781–817
- [245] Narang P, Sundararaman R and Atwater H A 2016 Plasmonic hot carrier dynamics in solid-state and chemical systems for energy conversion *Nanophotonics* **5** 96–111
- [246] Hutchison J A, Schwartz T, Genet C, Devaux E and Ebbesen T W 2012 Modifying chemical landscapes by coupling to vacuum fields *Angew. Chem., Int. Ed.* **51** 1592–6
- [247] Pellegrini C, Flick J, Tokatly I V, Appel H and Rubio A 2015 Optimized effective potential for quantum electro-dynamical time-dependent density functional theory *Phys. Rev. Lett.* **115** 093001
- [248] Galego J, Garcia-Vidal F J and Feist J 2015 Cavity-induced modifications of molecular structure in the strong-coupling regime *Phys. Rev. X* **5** 041022
- [249] Herrera F and Spano F C 2016 Cavity-controlled chemistry in molecular ensembles *Phys. Rev. Lett.* **116** 238301
- [250] Kowalewski M, Bennett K, Rouxel J R and Mukamel S 2016 Monitoring nonadiabatic electron-nuclear dynamics in molecules by attosecond streaking of photoelectrons *Phys. Rev. Lett.* **117** 043201
- [251] Kowalewski M, Bennett K and Mukamel S 2016 Cavity femtochemistry: manipulating nonadiabatic dynamics at avoided crossings *J. Phys. Chem. Lett.* **7** 2050–4
- [252] Kowalewski M, Bennett K and Mukamel S 2016 Non-adiabatic dynamics of molecules in optical cavities *J. Chem. Phys.* **144** 054309
- [253] Bienfait A *et al* 2016 Controlling spin relaxation with a cavity *Nature* **531** 74–7
- [254] Sun S, Kim H, Solomon G S and Waks E 2016 A quantum phase switch between a single solid-state spin and a photon *Nat. Nano* **11** 539–44
- [255] Zeng P, Cadusch J, Chakraborty D, Smith T A, Roberts A, Sader J E, Davis T J and Gómez D E 2016 Photoinduced electron transfer in the strong coupling regime: waveguide–plasmon polaritons *Nano Lett.* **16** 2651–6
- [256] Hutchison J A, Liscio A, Schwartz T, Canaguier-Durand A, Genet C, Palermo V, Samori P and Ebbesen T W 2013 Tuning the work-function via strong coupling *Adv. Mater.* **25** 2481–5
- [257] Orgiu E *et al* 2015 Conductivity in organic semiconductors hybridized with the vacuum field *Nat. Mater.* **14** 1123–9
- [258] Artuso R D and Bryant G W 2010 Strongly coupled quantum dot-metal nanoparticle systems: exciton-induced transparency, discontinuous response, and suppression as driven quantum oscillator effects *Phys. Rev. B* **82** 195419
- [259] Hutchison J A, O’Carroll D M, Schwartz T, Genet C and Ebbesen T W 2011 Absorption-induced transparency *Angew. Chem., Int. Ed.* **50** 2085–9
- [260] Schön P, Bonod N, Devaux E, Wenger J, Rigneault H, Ebbesen T W and Brasselet S 2010 Enhanced second-harmonic generation from individual metallic nanoapertures *Opt. Lett.* **35** 4063–5
- [261] Salomon A, Zielinski M, Kolkowski R, Zyss J and Prior Y 2013 Size and shape resonances in second harmonic generation from silver nanocavities *J. Phys. Chem. C* **117** 22377–82
- [262] Bowden C M and Dowling J P 1993 Near dipole-dipole effects in dense media: generalized Maxwell–Bloch equations *Phys. Rev. A* **47** 1247
- [263] Ziolkowski R W, Arnold J M and Gogny D M 1995 Ultrafast pulse interactions with two-level atoms *Phys. Rev. A* **52** 3082–94
- [264] Hofmann H F and Hess O 1999 Quantum Maxwell–Bloch equations for spatially inhomogeneous semiconductor lasers *Phys. Rev. A* **59** 2342–58
- [265] Slavcheva G, Arnold J M, Wallace I and Ziolkowski R W 2002 Coupled Maxwell-pseudospin equations for investigation of self-induced transparency effects in a degenerate three-level quantum system in two dimensions: finite-difference time-domain study *Phys. Rev. A* **66** 063418
- [266] Slavcheva G M, Arnold J M and Ziolkowski R W 2004 FDTD simulation of the nonlinear gain dynamics in active optical waveguides and semiconductor microcavities *IEEE J. Sel. Top. Quantum Electron.* **10** 1052–62
- [267] Gray S K and Kupka T 2003 Propagation of light in metallic nanowire arrays: finite-difference time-domain studies of silver cylinders *Phys. Rev. B* **68** 045415
- [268] Girard C, Martin O J F, Lévêque G, des Francs G C and Dereux A 2005 Generalized Bloch equations for optical interactions in confined geometries *Chem. Phys. Lett.* **404** 44–8
- [269] Fratallocchi A, Conti C and Ruocco G 2008 Three-dimensional *ab initio* investigation of light-matter interaction in Mie lasers *Phys. Rev. A* **78** 013806
- [270] Andreassen J and Cao H 2009 Finite-difference time-domain formulation of stochastic noise in macroscopic atomic systems *J. Lightwave Technol.* **27** 4530–5
- [271] Hellström S and Fu Y 2010 Dynamic optical response of an excitonic quantum dot studied by solving the self-consistent Maxwell–Schrödinger equations nonperturbatively *Phys. Rev. B* **82** 245305
- [272] Yu X-y, Liu W and Li C 2011 Near-resonant propagation of short pulses in a two-level medium *Phys. Rev. A* **84** 033811
- [273] Sukharev M and Nitzan A 2011 Numerical studies of the interaction of an atomic sample with the electromagnetic field in two dimensions *Phys. Rev. A* **84**
- [274] Pusch A, Wuestner S, Hamm J M, Tsakmakidis K L and Hess O 2012 Coherent amplification and noise in gain-enhanced nonplasmonic metamaterials: a Maxwell–Bloch Langevin approach *ACS Nano* **6** 2420–31
- [275] Meng L, Yam C, Koo S, Chen Q, Wong N and Chen G 2012 Dynamic multiscale quantum mechanics/electromagnetics simulation method *J. Chem. Theory Comput.* **8** 1190–9
- [276] Bellessa J *et al* 2009 Giant Rabi splitting between localized mixed plasmon-exciton states in a two-dimensional array of nanosize metallic disks in an organic semiconductor *Phys. Rev. B* **80** 033303
- [277] Mandel L and Wolf E 1995 *Optical Coherence and Quantum Optics* (Cambridge: Cambridge University Press)
- [278] Siegman A E 1986 *Lasers* vol 37 (Mill Valley, CA) pp 462–6
- [279] Chang S-H and Taflova A 2004 Finite-difference time-domain model of lasing action in a four-level two-electron atomic system *Opt. Express* **12** 3827–33
- [280] Fang A, Koschny T, Wegener M and Soukoulis C M 2009 Self-consistent calculation of metamaterials with gain *Phys. Rev. B* **79** 241104
- [281] Tempel D G and Aspuru-Guzik A 2011 Relaxation and dephasing in open quantum systems time-dependent density functional theory: properties of exact functionals from an exactly-solvable model system *Chem. Phys.* **391** 130–42
- [282] Allen L and Eberly J H 1975 *Optical Resonance and Two-Level Atoms* (New York: Wiley)
- [283] Sukharev M, Day P N and Pachter R 2015 Optical response of hybrid plasmon–exciton nanomaterials in the presence of overlapping resonances *ACS Photonics* **2** 935–41
- [284] Sukharev M and Malinovskaya S A 2012 Stimulated Raman adiabatic passage as a route to achieving optical control in plasmonics *Phys. Rev. A* **86** 043406
- [285] Lakshminarayanan V, Calvo M L and Alieva T 2012 *Mathematical Optics: Classical, Quantum, and Computational Methods* (Boca Raton, FL: CRC Press)

- [286] Besbes M *et al* 2007 Numerical analysis of a slit-groove diffraction problem *J. Eur. Opt. Soc.* **2** 0722
- [287] Yee K S 1966 Numerical solution of initial boundary value problems involving Maxwell's equations in isotropic media *IEEE Trans. Antennas Propagat.* **14** 302
- [288] Taflov A and Hagness S C 2005 *Computational Electrodynamics: the Finite-Difference Time-Domain Method* (Boston: Artech House)
- [289] Sadiku M N 2011 *Numerical Techniques in Electromagnetics with MATLAB* (Boca Raton, FL: CRC Press)
- [290] Sullivan D M 2013 *Electromagnetic Simulation using the FDTD Method* (New York: Wiley)
- [291] Kosloff R 1988 Time-dependent quantum-mechanical methods for molecular dynamics *J. Phys. Chem.* **92** 2087–100
- [292] Bérenger J-P 2007 *Synthesis Lectures on Computational Electromagnetics* vol 8 (San Rafael, CA: Morgan & Claypool)
- [293] Berenger J-P 1994 A perfectly matched layer for the absorption of electromagnetic waves *J. Comput. Phys.* **114** 185–200
- [294] Roden J A and Gedney S D 2000 Convolution PML (CPML): an efficient FDTD implementation of the CFS–PML for arbitrary media *Microw. Opt. Technol. Lett.* **27** 334–9
- [295] Kashiwa T and Fukai I 1990 A treatment by the FD-TD method of the dispersive characteristics associated with electronic polarization *Microw. Opt. Technol. Lett.* **3** 203–5
- [296] Pernice W H P, Payne F P and Gallagher D F G 2006 An FDTD method for the simulation of dispersive metallic structures *Opt. Quantum Electron.* **38** 843–56
- [297] Sullivan D M and IEEE Microwave Theory and Techniques Society 2000 *Electromagnetic Simulation Using the FDTD Method (IEEE Press Series on RF and Microwave Technology)* (New York: IEEE Press) p xv, 165p
- [298] Bidégaray B 2003 Time discretizations for Maxwell–Bloch equations *Numer. Methods Partial Differ. Equ.* **19** 284–300
- [299] Luebbers R J, Kunz K S, Schneider M and Hunsberger F 1991 A finite-difference time-domain near zone to far zone transformation [electromagnetic scattering] *IEEE Trans. Antennas Propagat.* **39** 429–33
- [300] Sukharev M, Seideman T, Gordon R J, Salomon A and Prior Y 2014 Ultrafast energy transfer between molecular assemblies and surface plasmons in hybrid nano-materials in the strong coupling regime *ACS Nano* **8** 807–17
- [301] Sukharev M and Nitzan A 2017 submitted
- [302] Puthumpally-Joseph R, Sukharev M, Atabek O and Charron E 2014 Dipole-induced electromagnetic transparency *Phys. Rev. Lett.* **113** 163603
- [303] Javanainen J, Ruostekoski J, Li Y and Yoo S-M 2014 Shifts of a resonance line in a dense atomic sample *Phys. Rev. Lett.* **112** 113603
- [304] Maki J J, Malcuit M S, Sipe J E and Boyd R W 1991 Linear and nonlinear optical measurements of the Lorentz local field *Phys. Rev. Lett.* **67** 972–5
- [305] Keaveney J, Sargsyan A, Krohn U, Hughes I G, Sarkisyan D and Adams C S 2012 Cooperative lamb shift in an atomic vapor layer of nanometer thickness *Phys. Rev. Lett.* **108** 173601
- [306] Puthumpally-Joseph R, Atabek O, Sukharev M and Charron E 2015 Theoretical analysis of dipole-induced electromagnetic transparency *Phys. Rev. A* **91** 043835
- [307] Fleischhauer M, Imamoglu A and Marangos J P 2005 Electromagnetically induced transparency: optics in coherent media *Rev. Mod. Phys.* **77** 633–73
- [308] Araújo M O, Krešić I, Kaiser R and Guerin W 2016 Superradiance in a large and dilute cloud of cold atoms in the linear-optics regime *Phys. Rev. Lett.* **117** 073002
- [309] Svidzinsky A and Chang J-T 2008 Cooperative spontaneous emission as a many-body eigenvalue problem *Phys. Rev. A* **77** 043833
- [310] Antosiewicz T J, Apell S P and Shegai T 2014 Plasmon–exciton interactions in a core–shell geometry: from enhanced absorption to strong coupling *ACS Photonics* **1** 454–63
- [311] Fauche P, Gebhardt C, Sukharev M and Vallee R A 2017 Plasmonic opals: observation of a collective molecular exciton mode beyond the strong coupling *Sci. Rep.* **7** 4107
- [312] Fauche P, Ungureanu S, Kolaric B and Vallee R A L 2014 Emitters as probes of a complex plasmophotonic mode *J. Mater. Chem. C* **2** 10362–8
- [313] Abella I D, Kurnit N A and Hartmann S R 1966 Photon echoes *Phys. Rev.* **141** 391–406
- [314] de Boeij W P, Pshenichnikov M S and Wiersma D A 1998 Ultrafast solvation dynamics explored by femtosecond photon echo spectroscopies *Annu. Rev. Phys. Chem.* **49** 99–123
- [315] Cho M, Scherer N F, Fleming G R and Mukamel S 1992 Photon echoes and related four-wave-mixing spectroscopies using phase-locked pulses *J. Chem. Phys.* **96** 5618–29
- [316] Brixner T, Aeschlimann M, Bauer M, Bayer D, de Abajo F J, Pfeiffer W, Rohmer M, Spindler C and Steeb F 2007 Adaptive subwavelength control of nano-optical fields *Nature* **446** 301–4
- [317] Blake A and Sukharev M 2017 Photon echo in exciton-plasmon nanomaterials: a time-dependent signature of strong coupling *J. Chem. Phys.* **146** 084704
- [318] Brixner T and Gerber G 2001 Femtosecond polarization pulse shaping *Opt. Lett.* **26** 557–9
- [319] Blake A and Sukharev M 2015 Surface plasmon polaritons in periodic arrays of V-shaped grooves strongly coupled to quantum emitters *Phys. Rev. B* **92** 035433
- [320] Lindberg M and Koch S W 1988 Effective Bloch equations for semiconductors *Phys. Rev. B* **38** 3342–50
- [321] Ning C Z, Indik R A and Moloney J V 1997 Effective Bloch equations for semiconductor lasers and amplifiers *IEEE J. Quantum Electron.* **33** 1543–50
- [322] Guazzotti S, Pusch A, Reiter D E and Hess O 2016 Dynamical calculation of third-harmonic generation in a semiconductor quantum well *Phys. Rev. B* **94** 115303
- [323] Li J-J and Zhu K-D 2014 Recent advances of light propagation in surface plasmon enhanced quantum dot devices *Crit. Rev. Solid State Mater. Sci.* **39** 25–45